Design of series fed antenna array with reduced beam squint and distortion

Changxu Zhao

TU Delft

Design of series fed antenna array with reduced beam squint and distortion

Thesis report

by

Changxu Zhao

to obtain the degree of Master of Science
at the Delft University of Technology
to be defended publicly on June 28, 2023 at 15:00

Thesis committee:

Chair:	Prof. Dsc. Alexander Yarovoy
Supervisor:	Dr. Yanki Aslan
External examiner:	Dr. Daniele Cavallo
Place:	Faculty of Electrical Engineering, Mathematics & Computer Science, Delft
Project Duration:	November, 2022 - June, 2023
Student number:	5401798

An electronic version of this thesis is available at `http://repository.tudelft.nl/`.

Abstract

With the development of the fifth generation (5G) technologies and beyond, the requirements for future wireless communication systems become more stringent, which demand novel antenna design at millimetre waves. The most commonly proposed array topology for 5G usage is square 8x8 or 16x16 microstrip patches with the full digital beam-forming method. Such designs result in massive complexity, high power consumption, and heat generation, especially with the full digital beam-forming method. To reduce design complexity and power consumption, the hybrid beam-forming is proposed, in which the linear subarrays are used with a fixed beam pattern in elevation, and combined in an array with digital beam-forming to realize the beam scanning in azimuth. Recent studies in the MS3 group at TU Delft have demonstrated that the series-fed subarray can be used in hybrid beam-forming and can realize any desired pattern by independent control of amplitude and phase on each unit cell. However, the main drawbacks of the series-fed arrays are the radiation beam squint and pattern distortion under different frequencies, which can limit the radiation bandwidth. Therefore, it is necessary to investigate the design of the series-fed antenna arrays to reduce the beam squint and pattern distortion.

In this thesis, the performance of series-fed antenna arrays radiating the csc^2 shaped beam pattern is investigated in terms of beam squint and pattern distortion. The RMS value is used in this thesis to quantify the pattern distortion in series-fed arrays and is used as a performance metric. Firstly, seven types of edge-fed series-fed subarrays are designed and optimized in CST. Their performance in terms of beam squint and pattern distortion is evaluated with and without considering the mutual coupling effect. Then, the subarray with the most stable radiation pattern over the evaluated frequency band (25 GHz - 27 GHz) is selected. Following this, the center-fed series-fed proximity-coupled subarray is designed aiming to reduce the amount of beam squint while having a stable radiation pattern. The performance of the center-fed subarray is compared with the edge-fed configuration in terms of the beam squint and pattern distortion. The simulation results show that the center-fed configuration can significantly reduce the beam squint but can increase the pattern distortion. Finally, the array of center-fed series-fed proximity-coupled subarrays is designed and simulated in CST. The results show that the array is able to reduce the beam squint (within $\pm 1°$) while having a reasonable pattern distortion (around 20% difference compared to the synthesized pattern) within the frequency range from 25.8 GHz to 26.5 GHz.

Acknowledgements

I would like to express my deepest gratitude to my daily supervisor, Dr. Yanki Aslan, for his invaluable guidance, unwavering support, and continuous encouragement throughout the duration of my thesis. His expertise, insightful feedback, and dedication to my academic growth have played a pivotal role in shaping the outcome of this research.

I would also like to extend my sincere appreciation to Prof. DSc. Alexander Yarovoy, the Chair of the Microwave Sensing, Signals, and Systems group at TU Delft. I am honoured to have had the opportunity to work under his esteemed supervision. His profound knowledge, visionary leadership, and unwavering commitment to excellence have been a constant source of inspiration for me. I am grateful for his support, valuable insights, and the platform he has provided to explore cutting-edge research in this field.

Last but not least, I want to express my heartfelt appreciation to my family for their unconditional love, encouragement, and unwavering belief in me. Their constant support and understanding have been the foundation of my academic pursuits.

Above all, I am immensely grateful to Dr. Yanki Aslan, Prof. DSc. Alexander Yarovoy, the Microwave Sensing, Signals, and Systems group, my classmates, and my family for their contributions and support throughout my thesis. Their collective efforts have been instrumental in shaping the successful completion of this research endeavour.

Changxu Zhao
Delft, 19 June 2023

Contents

Nomenclature

List of Abbreviations

5G the Fifth Generation

AC-MPA Aperture-Coupled Microstrip Patch Antenna

AF Array Factor

CMOS Complementary Metal-Oxide-Semiconductor

CPS Co-Planar Strip

CPW Co-Planar Waveguide

EUCAP European Conference on Antennas and Propagation

LWA Leaky-Wave Antenna

MIMO Multi Input Multi Output

NRI-TL Negative Refractive Index Transmission Line

PEC Perfect Electric Conductor

RMS Root-Mean-Square

RMSE Root-Mean-Square Error

SICL Substrate Integrated Coaxial Line

SIW Substrate Integrated Waveguide

TE Transverse Electric

TEM Transverse Electric and Magnetic

VSWR Voltage Standing Wave Ratio

List of Figures

List of Tables

1 Introduction

This chapter includes the background information of the thesis. The advantages of the series fed-antenna arrays in the next-generation of base station antennas are described in Section 1.1. The relevant previous research in the MS3 group is summarized in Section 1.2. The unsolved scientific challenges regarding the beam squint and pattern-shape distortion are explained in Section 1.3. The research objective and scope are listed in Section 1.4. The novelties of the thesis are enumerated in Section 1.5. Finally, the structure of the rest of the thesis is outlined in Section 1.6.

1.1. Motivation

With the development of the fifth generation (5G) technologies and beyond, the requirements for future wireless communication systems become more stringent on channel capacity, link quality, cost and reliability, which demand novel antenna design solutions at millimetre waves. In particular, the next-generation base stations are required to provide multiple simultaneous beams, as shown in Figure 1.1, using the same frequency band and time resources with limited interference, suitable processing complexity, acceptable power consumption and simple thermal management [1].

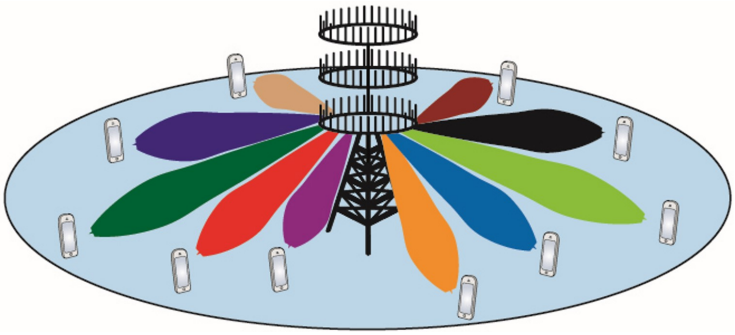

Figure 1.1: 5G base station multi-beam scenario [2]

The most commonly proposed array topology for 5G usages is square 8x8 or 16x16 microstrip patches with square lattices and half-wavelength element separation [3]. Such designs result in massive complexity, power consumption, and heat generation when using full-digital beam-forming [4]. To reduce design complexity and power consumption, hybrid beamforming has gained more attention due to its low cost and complexity [5]. In hybrid beamforming, an appealing approach is to design linear subarrays in analogue beam forming with a fixed beam pattern in elevation, and combine them in an array with digital beamforming to realize the beam scanning in azimuth (Figure 1.2) [6].

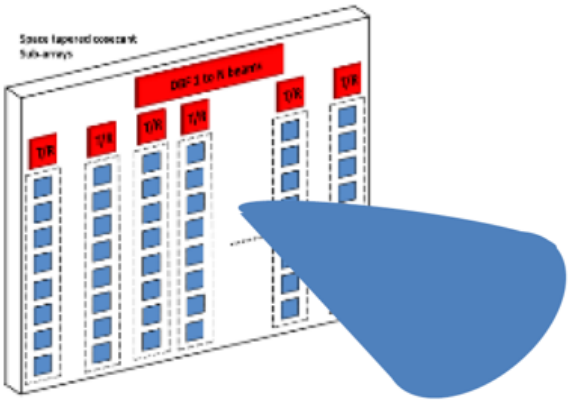

Figure 1.2: Array of vertical shaped beam sub-arrays [7]

1.2. Relevant research in MS3

In the last few years, the MS3 group at TU Delft has extensively studied the optimization and design of subarrays for millimeter-wave hybrid beamforming usage. A design of a transverse slot array at 24GHz fed by SIW technology was proposed in [8]. The 6-element sub-array structure proposed in that paper realizing a -30dB Dolph-Chebyshev amplitude distribution is shown in Figure 1.3. The design combines hybrid beam-forming which reduces hardware/processing complexity and power consumption, with SIW feeding technology which reduces the losses. In addition, the design in [8] allows independent control of amplitude and phase on each unit cell, which makes the designed sub-array possible to realize any desired pattern.

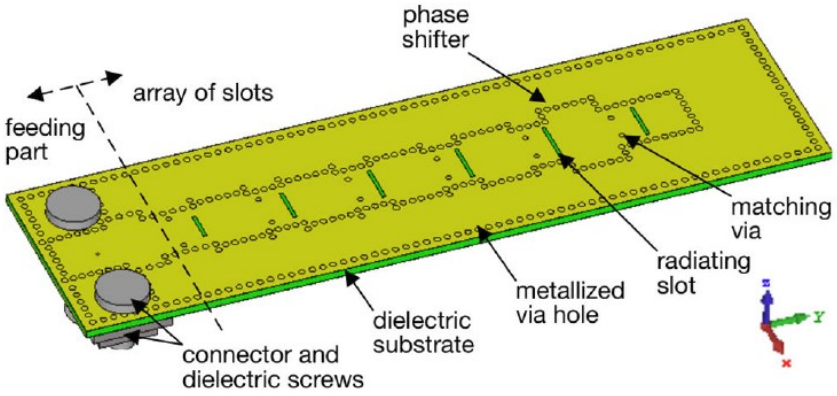

Figure 1.3: Structure of transverse slot sub-array fed by SIW [8]

A recent study case in [7] shows that for a 200m cell from a base station at H=10m, about 90% of ground-only users are within 3° to 10° from the horizon as shown in Figure 1.4a. Based on this result, the cosecant-squared beam pattern in elevation (Figure 1.4b) was proposed in [7] to realize equi-power coverage. An amplitude-phase distribution synthesis algorithm based on iterative rephasing and projection of the mask pattern was developed in-house. This particular beam shape can be used in hybrid beam-forming in which the single analogue beam in the elevation plane with a cosecant-squared shape is used, and the beam in the azimuth plane is digitally controlled. Such hybrid-beamforming method in [7] drastically reduces the number of array chains, the complexity, processing, consumption and cost. Combining the research from [8] and [7], a SIW series-fed aperture coupled microstrip patch antenna (AC-MPA) array that realized the cosecant-squared beam pattern is proposed in [9]. The array was designed based on the concept proposed in [8] with an additional patch layer on top of the slot layer. Comparing with the design in [8], the design in [9] has increased the impedance bandwidth from 150 MHz to 5.7 GHz after

adding the patch layer. The antenna array design in [9] partially satisfies the challenging requirements of 5G application in terms of multi-beam generation capability with a large scanning area and low-cost implementation.

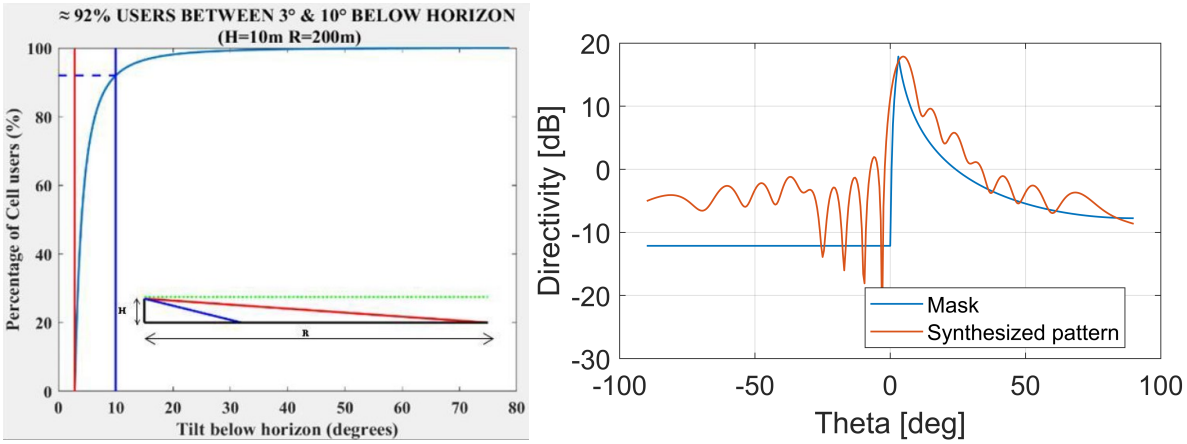

(a) Percentage of user coverage [7]

(b) Cosecant-squared beam pattern (Theta is the elevation angle)

Figure 1.4: Equi-power user coverage

Before the start of this thesis, an extra project has been done on the SIW series-fed transverse slot array design for the shaped-beam pattern. During the extra project, two new transverse slot SIW-fed sub-arrays operating at 26GHz have been designed to operate in base station antennas with hybrid beamforming dedicated to work in dense urban environments. The radiation patterns in the elevation plane have been tailored to two innovative and representative deployment scenarios as shown in Figures 1.5 and 1.6. To limit the distance between the subarrays and avoid grating lobes while scanning in azimuth, a novel phase shifter structure has been proposed and implemented into the sub-array design. The simulated results of the realized pattern and impedance matching performance of two proposed subarrays are shown in Figures 1.7 and 1.8. The CST models of the designed subarrays for both scenarios are shown in Figure 1.9. At the end of the extra project, a paper was published on European Conference of Antennas and Propagation (EUCAP) [10].

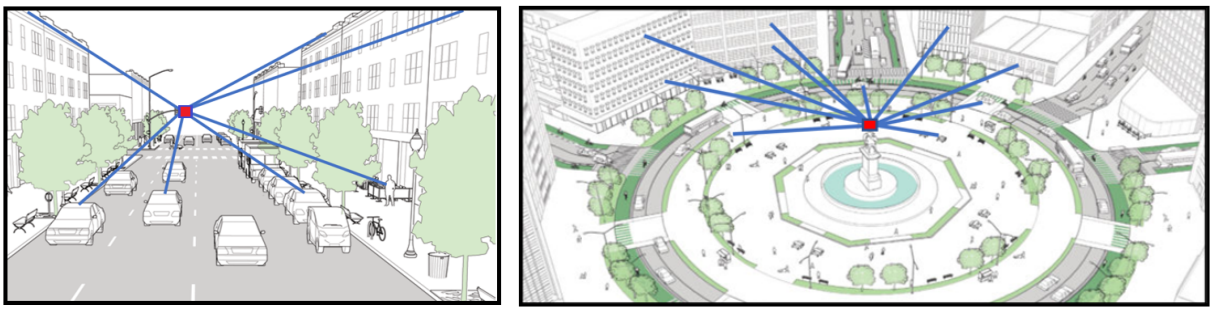

(a) **(b)**

Figure 1.5: Urban area base station environment: (a) Scenario-1: street, (b) Scenario-2: roundabout or city square. [10]

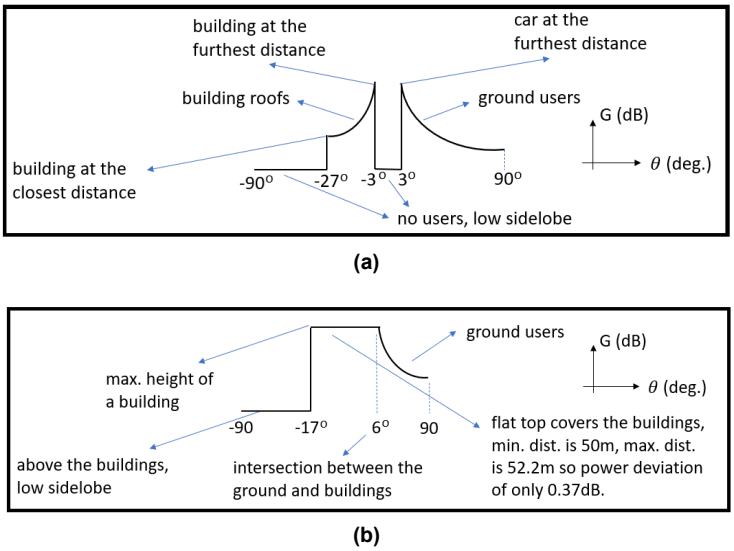

Figure 1.6: Shaped elevation beam patterns for the deployment scenarios: (a) Scenario-1: dual-cosecant-squared shape, (b) Scenario-2: combined flat-top cosecant-squared shape. [10]

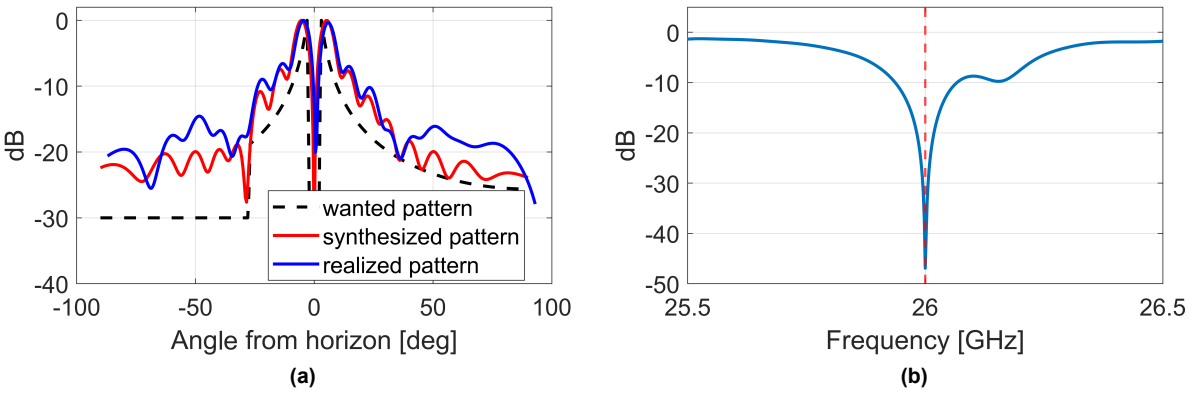

Figure 1.7: Subarray performance for Scenario-1: (a) simulated pattern, (b) reflection coefficient. [10]

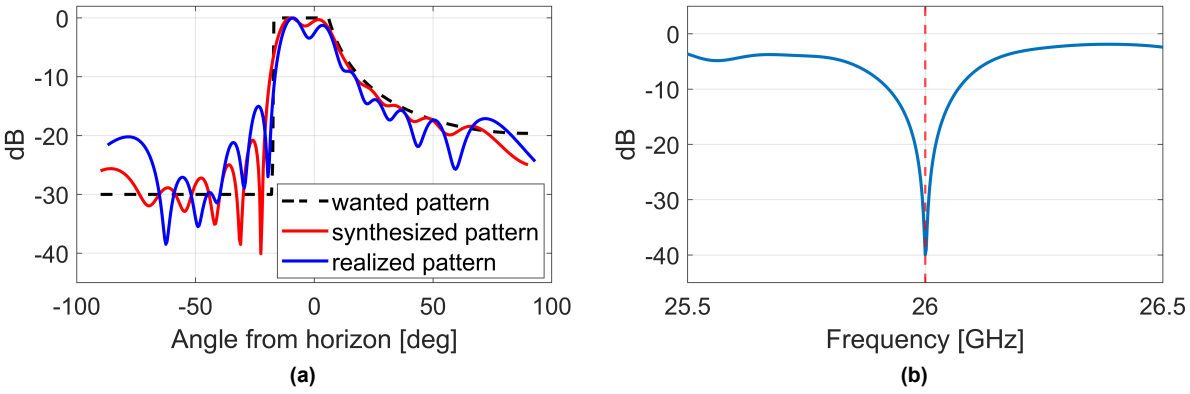

Figure 1.8: Subarray performance for Scenario-2: (a) simulated pattern, (b) reflection coefficient. [10]

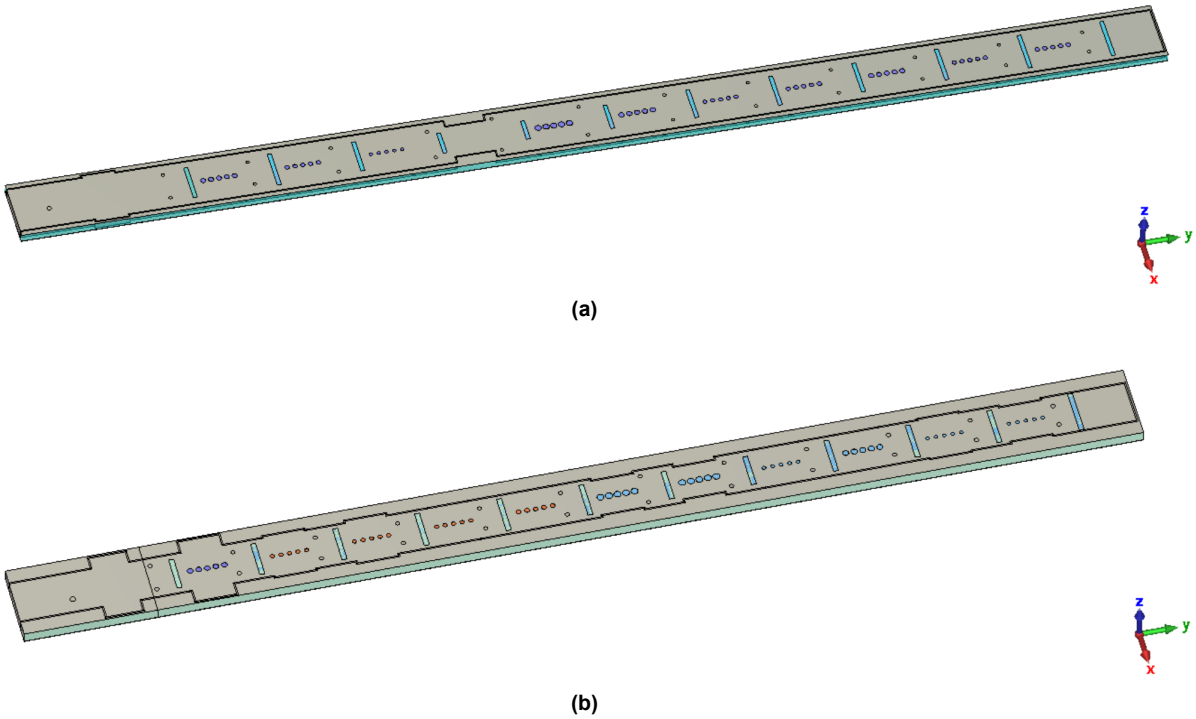

Figure 1.9: Transverse slot subarray models in CST: (a) scenario-1, (b) scenario-2.

1.3. Problem formulation

By radiating the shaped beam patterns (csc^2, $dual - csc^2$, flat-top) under desired urban scenarios, the base station is able to deliver the power equally to the users located at different distances from the base station. Therefore, keeping the pattern shape stable within the operational bandwidth is important since a distorted pattern leads to reduced power delivery efficiency.

Despite the mentioned advantages of the antenna array design in [8–10], the main drawbacks of such designs are the radiation beam squint and pattern distortion under different frequencies. In other words, although the impedance bandwidth is sufficiently large, the radiation bandwidth is very limited. According to [9], the designed array suffers from the beam squint of about $\pm 4°$ in the frequency band of 1 GHz. Here, we provide the benchmark design results based on the current research level to highlight the significance of the problem.

Figure 1.10 shows the radiation pattern of a designed 12-element subarray centered at 26 GHz with $0.65\lambda_0$ spacing between each unit cell, following the design steps described in [8] based on the SIW transverse slot subarray. The radiation pattern of the designed subarray was simulated at ± 800 MHz band, which is half of the millimeter wave band centered at 26GHz (24.25-27.5GHz) according to [11]. It can be seen that the pattern shape and main-lobe direction are highly distorted and squinted when the operating frequency is moved ± 800 MHz from the center frequency. Such beam squint and pattern distortion under different frequencies limit the radiation bandwidth of the designed antenna array and are not desired in the usage of a 5G base station.

There are two main reasons for the beam squint and pattern distortion in series-fed antenna arrays: 1) Frequency-dependent of the phase and amplitude distribution of each unit cell. 2) Mutual coupling between unit cells. During the design process of the SIW-fed slot array introduced by [8], each unit cell was tuned to a specific amplitude and phase distribution required by the pattern shape under the center frequency. However, this makes the tuning result only valid for the center frequency, since the amplitude and phase of each unit cell are highly frequency-dependent. A particular tuning result of one unit cell is shown in Figure 1.11. It can be seen that the tuned coupling coefficient and phase are highly dependent on frequency. When the operating frequency change, the phase and amplitude distribution change as well, which leads to beam squint and pattern distortion. Furthermore, mutual coupling between unit cells can also have a

significant impact on pattern shape and beam direction. Figure 1.12 shows the radiation patterns of the designed transverse slot subarray (including the mutual coupling) compared with the unit cell patterns after adding the array factor (neglecting the mutual coupling). It can be seen that after including the mutual coupling, the pattern is distorted and the beam is squinted. So, it is necessary to find a way to reduce the beam squint and pattern distortion so that the designed antenna array can operate under a wider operational bandwidth.

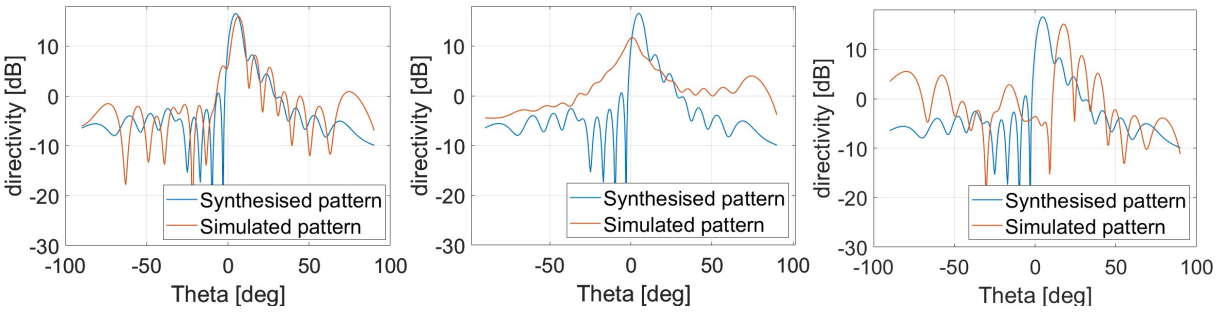

(a) Pattern at 26 GHz **(b)** Pattern at 25.2 GHz **(c)** pattern at 26.8 GHz

Figure 1.10: Pattern distortion and beam squint at different frequencies (centered at 26 GHz) on SIW-based transverse slot subarray

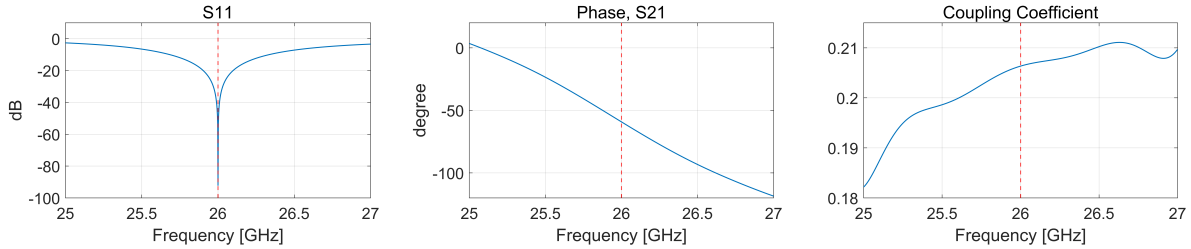

(a) Reflection coefficient S11 **(b)** Phase S21 **(c)** Coupling coefficient

Figure 1.11: Frequency dependent of the tuning results of one unit cell

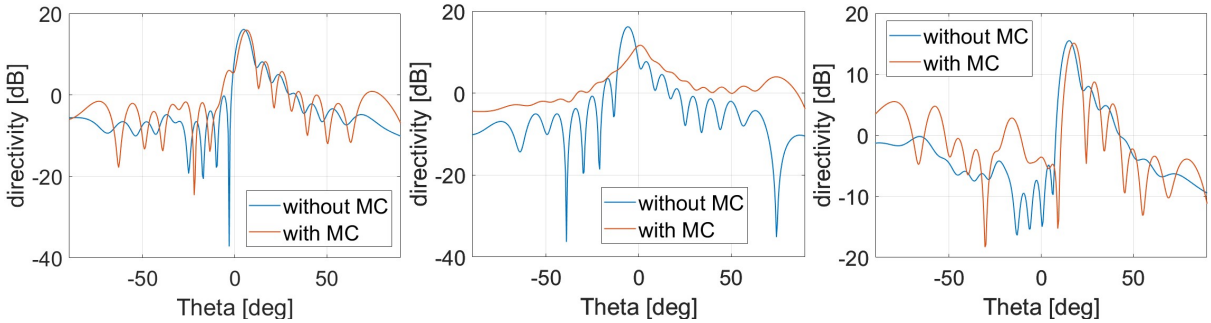

(a) Pattern at 26 GHz **(b)** Pattern at 25.2 GHz **(c)** pattern at 26.8 GHz

Figure 1.12: Pattern distortion and beam squint due to mutual coupling at different frequencies (centered at 26 GHz)

1.4. Thesis objectives and scope

1.4.1. Objectives

The objectives of this thesis are:

1. Identify and design different types of unit cells (SIW, SICL, slot, slot+patch), compare their pattern-shaping performance in an edge-fed series-fed array, quantify and compare the impact on beam squint and pattern distortion.
2. Include mutual-coupling effects in the subarray design procedure to determine its impact on pattern shaping and beam squinting.
3. Select the most-promising unit cell types, design mid-fed subarrays and compare the pattern shaping and stability performance with the edge-fed subarrays.
4. Design the array of subarrays and identify the scanning capabilities.

1.4.2. Scope

The scopes of the thesis are:

1. The pattern shape focused on in this thesis will be the cosecant-squared pattern as shown in Figure 1.4b due to its proven benefits in realistic deployment scenarios. However, once the design methodology is developed, the proposed design approaches can be used for arbitrary pattern shapes.
2. The array designed and simulated during the thesis will be centred around 26 GHz which is in the 5G mm-Wave n258 frequency band.
3. The feeding type of the sub-array focused on during this thesis will be the series-fed linear sub-array.
4. The number of unit cells within one subarray will be fixed at 12 since its optimized for the cosecant-squared beam pattern using the optimization method in [10].
5. The element spacing within the subarray will be fixed at $0.65\lambda_0$ since its optimized for the cosecant-squared beam pattern using the optimization method in [10].
6. The spacing between subarrays will be controlled around $0.5\lambda_0$ to prevent grating lobe when doing the scanning in azimuth
7. The modelling and simulation of the designed antenna array during the thesis will be done mainly in CST Microwave studio
8. Metal in the subarray structure will be replaced by PEC, and the SIW structure will be replaced by metallic walls made from PEC at first to reduce the simulation time in order to focus on pattern behaviour. In the end, the results will be given by replacing the lossless materials with the lossy ones.
9. The vertical polarization is selected during the design in this thesis since it provides better horizontal scanning performance in the previous prototype in the MS3 group.

1.5. Novelties

1. For the first time, different types of unit cells are compared based on the beam squint and pattern distortion performance in (asymmetrically) shaped beam series-fed arrays, especially for the csc^2 shaped radiation pattern.
2. For the first time, center-fed series-fed arrays are studied for shaped-beam pattern stability and compared with the edge-fed counterparts.
3. For the first time, the pattern distortions in the series-fed antenna are quantified via Root-Mean-Square (RMS) error and used as a performance metric.
4. A novel proximity-coupled patch unit cell is proposed for the most frequency-stable csc^2 shaped subarray beam pattern (i.e. less than 1-degree beam squint, less than 1.5 dB variation in the realized gain and less than 20% RMS error in the beam shape within a 700-MHz bandwidth).

1.6. Thesis structure

The outline of the thesis is the following:

Chapter 2 presents the state of the art of the existing research. In the first part, different realizations of the series-fed antenna array are discussed in terms of different feeding strategies and radiation elements. In the second part, different techniques for reducing the beam squint are explored, and the gaps in the existing techniques are explained and linked to the contribution of this thesis.

Chapter 3 presents the detailed design and analysis of edge-fed series-fed antenna subarrays. First, the csc^2 radiation pattern is synthesized for the edge-fed array configuration, with the desired excitation phase and amplitude. Then, the design of seven different unit cell structures are discussed with detailed dimensions and optimization results. The radiation patterns of the designed edge-fed antenna arrays are analyzed both with and without considering the mutual-coupling effect. The influence of the excitation amplitude and phase distribution on the pattern shape is explored. The impact of the mutual-coupling on the pattern shape is studied. The performance of the designed subarrays is compared in terms of the beam squint and pattern distortion. Finally, the subarray design with the minimum pattern distortion over the simulated bandwidth is selected in order to implement the beam squint reduction technique during further investigation.

Chapter 4 presents the detailed design and analysis of center-fed series-fed antenna subarray. First, the cec^2 radiation pattern is synthesized for the center-fed array configuration, with the desired excitation phase and amplitude. Then, the selected edge-fed subarray design from Chapter 3 is modified to fit the center-fed configuration. The radiation pattern of the center-fed subarray is analyzed both with and without mutual-coupling, and the influence of the excitation amplitude and phase on pattern shape is investigated. Finally, the performance of the edge-fed subarray and the center-fed subarray is compared in terms of the beam squint and pattern distortion.

Chapter 5 presents the design of the array of subarrays. First, the center-fed subarray design introduced in Chapter 4 is extended to a phased array of 12 subarrays. The performance of the array is compared with the 1x12 subarray. Finally, the lossless material used in array simulation will be replaced by the lossy material to make the simulation results closer to reality, the scanning performance of the lossy array will then be checked.

Chapter 6 summarizes the thesis work and gives recommendations for future research.

2

Literature review

This literature review starts with the introduction of different implementation technologies of series-fed antenna designs. Next, multiple techniques for reducing beam squint and pattern distortion will be critically discussed and the scientific gaps will be emphasized. The contributions of this thesis will be linked to these gaps in knowledge.

2.1. Series-fed antenna design techniques

In this section, different realizations of series-fed antenna arrays will be discussed. Their advantages and disadvantages will be compared and summarized at the end of the section.

2.1.1. Microstrip series-fed antennas

As one of the most common configurations of series-fed antenna arrays, designs of microstrip-based series-fed antenna arrays have been extensively studied and proposed in previous years. Microstrip series-fed arrays have been shown to constitute an effective configuration to enhance antenna efficiency since the length of feed line runs is substantially reduced in comparison to conventional corporate feed systems [12]. Some key features of a microstrip series-fed array are relative ease of construction, lightweight, low cost, low profile and extremely thin protrusion from the surface [13]. The limitations of the microstrip series-fed arrays are that they tend to radiate efficiently only over a narrow band of frequencies and cannot operate at high power levels [13].

In microstrip-fed designs, different strategies can be used to control the excitation amplitude and phase of a radiation element. The phase of each radiation elements can be controlled by simply varying the length of the feeding line to create different amount of delay between the input and the output signal. The amplitude tapering, takes the microstrip series-fed patch arrays as an example, can be achieved by line width variation [14] or patch width variation[15]. Both methods are compared in [16]. For the line-width tapering, the advantage is that the radiation characteristic of each patch element remains the same since the width of each patch is constant. However, since the line-width-tapering is more sensitive compared to patch-width-tapering, fabrication tolerances might be an issue for higher frequencies such as in mm-Wave [16]. What's more, both line-width and patch-width tapering methods can be combined together to achieve better VSWR and lower side-lobe level [17]. To achieve wide bandwidth in microstrip series-fed arrays, a multi-layer structure with aperture coupling was proposed [18]. In addition, dual-polarization can be realized in microstrip series-fed arrays by simply using two separate feeding lines coupled with two perpendicularly placed slots (Figure 2.2) [19].

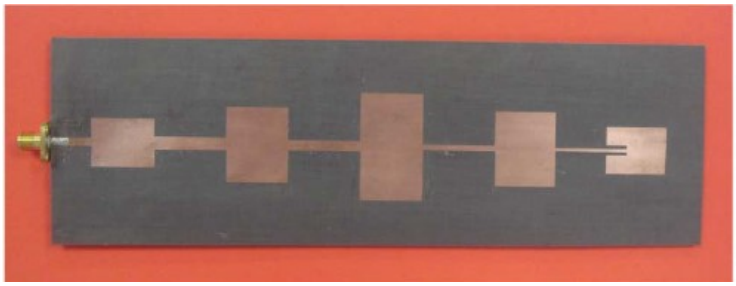

Figure 2.1: Microstrip Series-fed patch antenna array [17]

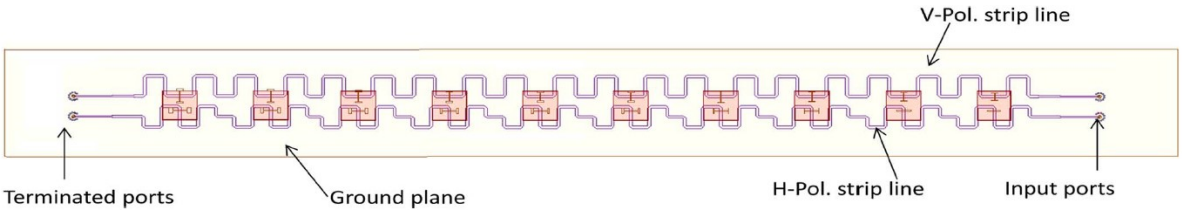

Figure 2.2: Dual-polarization microstrip series-fed aperture-coupled patch array [19]

As one of the most popular configurations of series-fed antenna arrays, microstrip series-fed antenna arrays have been extensively studied during the previous years [14–19]. Different technologies has been proposed to enhance the performance such as the bandwidth, the radiation efficiency and low side-lobe level as described in the above paragraph. However, there is no research that realized shaped-beam pattern synthesis in microstrip series-fed arrays such as the cosecant-squared beam pattern. Realizing such patterns requires accurate control of the excitation phase and amplitude of each radiation element. So, it's still worth investigating the behaviour of the microstrip series-fed antenna arrays in shaped beam patterns and compare its performance with other series-fed array configurations.

2.1.2. SIW series-fed antennas

The concept of substrate-integrated waveguide (SIW) was first developed in the early 2000s by Ke Wu in order to fulfil the miniaturization required by modern applications [20]. The basic structure of SIW is shown in Figure 2.3. As the traditional rectangular waveguide, the dominant mode propagates in the SIW structure is the TE10 mode. Compared to the traditional waveguide, SIW technology brings a more compact structure and can be manufactured easily at low cost for mass production by making densely arrayed via-holes and metal plating the surfaces [21]. Compared to the microstrip feeding networks, SIW has a high front-to-back ratio and low conduction loss for large-scale antenna arrays [22].

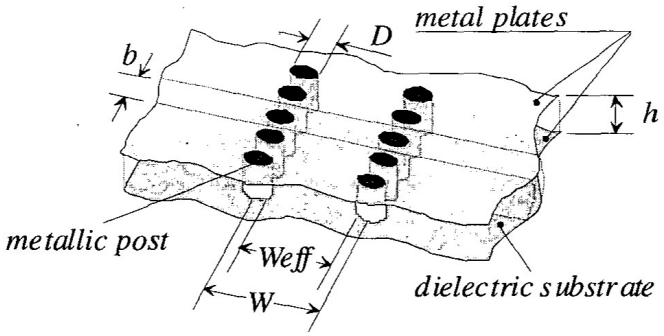

Figure 2.3: Basic SIW structure [20]

In recent years, SIW technology has been extensively used in many designs of series-fed antenna arrays. The efficiency of the series-fed aperture coupled microstrip patch antenna (AC-MPA) array can be

improved by using a SIW feeding structure [22]. Moreover, the SIW-based AC-MPA array can also be used to generate shaped beam patterns such as the cosecant-squared beam pattern, such design is proposed using the standing-wave configuration in [21]. In addition, the SIW feeding structure can bring a compact antenna structure and provides a more efficient radiation characteristic without the spurious radiation that is usually produced by a conventional feeding line such as the microstrip [21]. The design of the SIW-based series-fed arrays with transverse slots (Figure 2.4) was proposed to improve the scanning ability in azimuth and the travelling-wave configuration is used for a more flexible design and larger bandwidth, realizing a cosecant-squared beam pattern in elevation [8]. To improve the impedance bandwidth of the series-fed transverse slot arrays based on SIW, a patch layer can be added on top of the slot layer to form a transverse slot AC-MPA array based on SIW [9]. It's also possible to realize dual polarization in SIW-based series-fed arrays. However, compared to microstrip-based series-fed arrays, the realization of dual polarization in SIW-based series-fed arrays is less flexible. The main reason for this is the overlarge physical dimension of SIW due to the cutoff frequency of its TE10 mode [23]. A design that realized dual-polarization using $\pm 45°$ inclined slot arrays based on SIW was proposed, where two separate slot subarrays were needed for each polarization [24].

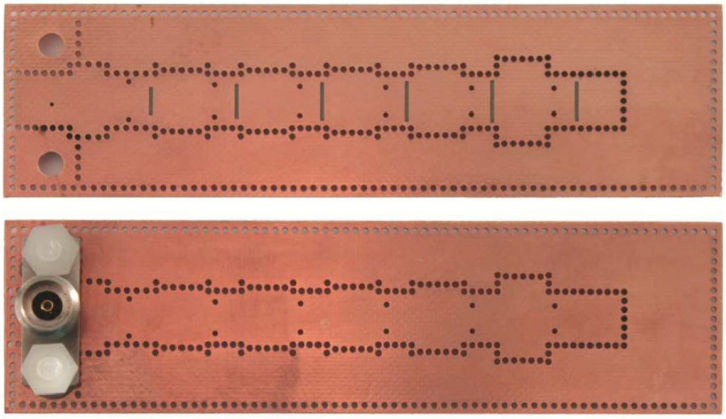

Figure 2.4: Prototype of the SIW-based series-fed transverse slot array [8]

Despite the advantages of using the SIW structure, the main problems in the current SIW-based series-fed antenna design are the beam squint and pattern distortion as described in Section 1.3, which is not desired for the 5G base station usage. Until now, there is little research on studying the beam squint and pattern distortion reduction in SIW-based series-fed antenna arrays, especially for shaped beam patterns. So, it's worth investigating the possible way to reduce beam squint and pattern distortion in SIW-based series-fed arrays.

2.1.3. SICL series-fed antennas

The substrate-integrated coaxial line (SICL) (Figure 2.5) is first introduced by [25], aiming to combine the advantages of the coaxial cables and of the planar transmission lines. SICL can be fabricated by using a simple, low-cost thin-film process or by CMOS technology, and can be easily integrated with active devices [25]. Traditional feeding structures such as microstrip line suffers from extremely high mutual coupling; the gap waveguide's structure is too complex to implement and the SIW structure is large for high frequencies, not suitable for a massive MIMO system [26]. Compared to the traditional feeding structure, SICL technology has the following three advantages [27]:

1. supporting transverse electric and magnetic (TEM) mode, which will benefit broadband single-mode operation.
2. has a smaller transverse dimension, around $0.23\lambda_0$ in longitudinal slot antenna design.
3. easy to design amplitude-tapering feeding network just as easy as microstrip line does, which is intricate for SIW structure.

According to [25], the cut-off frequency of TE_{10} mode in a SICL structure is defined using the following formula:

$$f_{TE10} = \frac{c}{2\sqrt{\epsilon_r}}(A - \frac{D^2}{0.95S})^{-1} \tag{2.1}$$

Where A, D and S are the dimensions shown in Figure 2.5, ϵ_r is the relative dielectric permittivity of the substrate and c is the speed of light in vacuum. During the design of the SICL structure, the center frequency should always below the cut-off frequency f_{TE10}, so that the dominant mode propagates in the SICL will be the TEM mode.

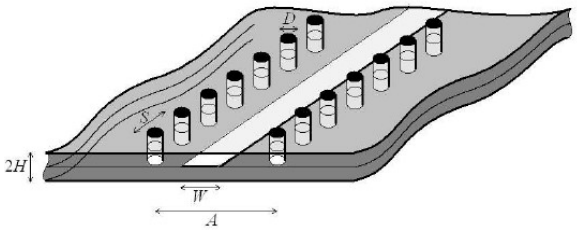

Figure 2.5: Geometry of a Substrate Integrated Coaxial Line [25]

The series-fed longitudinal-placed slot array based on SICL technique was first proposed (Figure 2.6), with a SICL feeding line design that can realize Chebyshev distribution for low side-lobe level [28]. The SICL feeding structure used for grating-lobe suppression in series-fed transverse slot array is first proposed in [29]. A 45° polarization can be realized in SICL-based series-fed slot array by placing the slot in 45° offset [30]. The SICL feeding network can also be used to suppress the back-lobe level, the side-lobe level and improve the radiation performance in series-fed AC-MPA array [27].

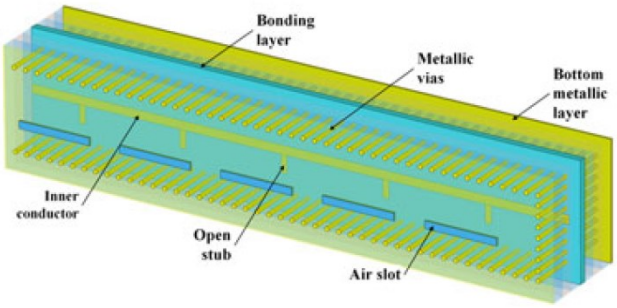

Figure 2.6: SICL-based slot array antenna Liu et al. [28]

Above all, the SICL technology has not been studied as much as the other two (microstrip, SIW) since it is a newly proposed approach during recent years. Still, some relevant researches on SICL-based series-fed arrays have been found and discussed in the above paragraph [27–30]. Those researches mostly aim for realizing amplitude tapering, side-lobe impression, back-lobe suppression and high radiation efficiency. However, no research has been done on SICL-based series-fed array for shaped beam patterns. So, it's worth to investigate a possible design for SICL-based series-fed antenna array that can realize shaped-beam patterns.

2.1.4. Comparison of the existing series-fed antenna arrays

A summary of all searched series-fed antenna arrays is listed in Table 2.1, where f_0 stands for the centre frequency and the BW stands for the impedance bandwidth. It can be seen that most of the designs use patch as the radiator since it can generator higher gain comparing to the slot. In addition, the design based on the SIW and the SICL focus more on mm-Wave band while the design based on the microstrip focus

more on lower band, since the SIW and the SICL technology were originally developed for high-frequency applications [20, 31]. From all series-fed arrays designs that have been searched, most of the patterns realized by the designs are the broadside radiation patterns with some amplitude tapering such as the Dolph-Chebyshev and Taylor. Only two of the designs have realized shaped beam pattern (cosecant-squared) and they are all based on SIW technology. So, it is worth to investigate the series-fed array design based on the other two technologies (microstrip and SICL), and see their performance on realizing shaped beam pattern. Moreover, despite it is seldom mentioned in the searched papers, one common problem of the existing series-fed array design is the beam squint and pattern distortion, which will be further discussed in Section 2.2.

Table 2.1: Comparison of different series-fed antenna arrays

Ref	Feeding	Element No.	Radiator	Tapering	f_0 (GHz)	BW (%)	Gain (dBi)
[14]	microstrip	6	patch	Dolph-Chebyshev	5.785	6.5	14
[15]	microstrip	20	patch	Taylor	76	\	17
[17]	microstrip	5	patch	-14dB side-lobe taper	5	2.8	\
[18]	microstrip	14	patch	-19.6dB side-lobe taper	1.25	7	19
[19]	microstrip	10	patch	Taylor	2.73	\	15
[22]	SIW	4	patch	No tapering	30	5.3	14.5
[21]	SIW	12	patch	Cosecant-Squared	28.5	10	15.7
[8]	SIW	6	slot	Dolph-Chebyshev	24.125	0.62	11.6
[9]	SIW	12	patch	Cosecant-Squared	28.5	20	16.3
[24]	SIW	8x5	slot	No tapering	16	\	22
[28]	SICL	5x10	slot	Dolph-Chebyshev	35	4.57	15
[29]	SICL	5x8	slot	Dolph-Chebyshev	34	5.54	12.98
[30]	SICL	5x6	slot	Dolph-Chebyshev	35	2.6	17.09
[27]	SICL	6x6	patch	Dolph-Chebyshev	42	6.4	18.34

2.2. Beam squint reduction techniques

In series-fed antenna array, the main reason that cause the beam squint in the antenna array is the frequency-dependence on phase distribution since the main beam direction is highly dependent on the exciting phase on each unit cell of the array. In this section, different method and techniques for beam squint reduction will be discussed. One of the ideal methods to reduce the beam squint is to provide a constant phase shift over a large frequency band, such idea can be realized, in general, by using wide-band phase shifter, which will be discussed in Section 2.2.1. Then, other techniques aim to reduce the beam squint in series-fed arrays will be discussed in Section 2.2.2.

2.2.1. Beam squint reduction using wide-band phase shifter

In recent years' studies, many kinds of wide-band phase shifter structures have been developed. In general, there are mainly 4 categories of wide-band phase shifters [32]: (1) Schiffman phase shifters (2) loaded-line phase shifters (3) broadside coupling phase shifters (4) other types.

The wide-band phase shifter based on microstrip line (Figure 2.7) can provide good performance with simplicity in both design and fabrication [33]. What's more, dual-wideband can be realized in microstrip-based wide-band phase shifter by using a folded coupled-line [34]. Except for the microstrip-based wide-band phase shifter, SIW technology can also be used in the wide-band phase shifter designs. By adding the air-holes along the middle line of the substrate in the SIW structure, constant phase shift can be obtained relative to an SIW line of the same length [35]. The microstrip and the SIW structure can even be combined together to form a wide-band phase shifter as shown in Figure 2.8, the slots etched on the top surface of SIW are used to counteract the phase shift slope from the microstrip delay line [36].

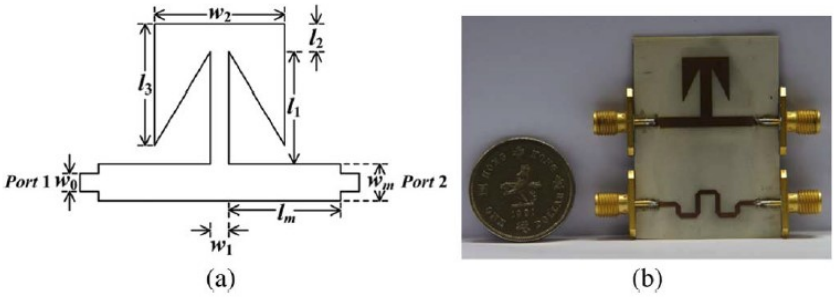

Figure 2.7: Configuration of the microstrip line based phase shifter loaded with T shape open stub [33]

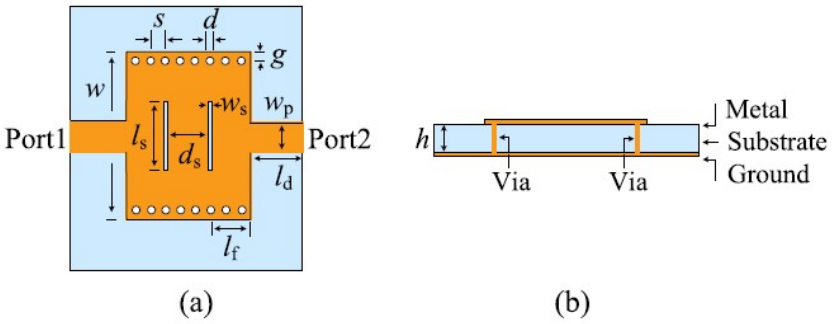

Figure 2.8: Configuration of the SIW based phase shifter [36]. (a) Top view. (b) Cross-sectional view

According to the research, many kinds of wide-band phase shifters can provide relatively constant phase shifts over a large bandwidth [33–36]. However, the provided constant phase shift is relative to a reference line, meaning the constant phase shift is obtained by subtracting the phase shift of the phase shifter from the phase shift of the reference line. Figure 2.9 shows a typical phase response of a 45° wide-band phase shifter and its reference line. It can be seen that despite the phase difference between the phase shifter and the reference line remaining constant at around 45°, the phase response of the phase shifter itself is still highly dependent on frequency. This can be a problem for the series-fed antenna array since the phase shift of each unit cell is directly related to each other, thus the traditional wide-band phase shifter design cannot be directly applied to series-fed array design. The only way to realize true constant phase shift is to use active device such as the negative delay circuit, but implement such circuits to series-fed antenna is not suitable due to the complexity and power inefficiency. So, other approaches are needed for beam squint reduction in series-fed arrays.

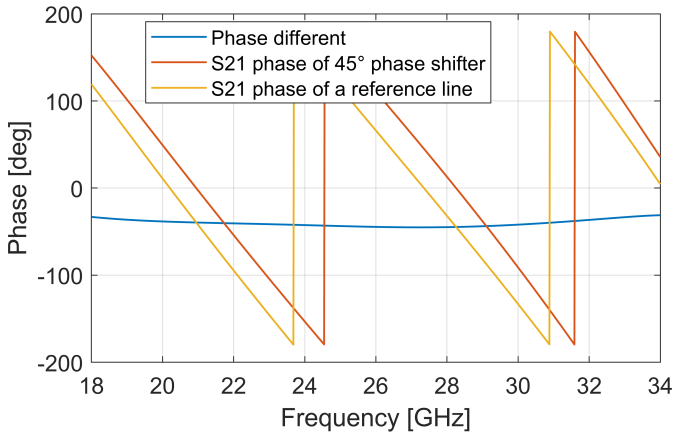

Figure 2.9: Typical phase response of a 45° wide-band phase shifter and its reference line

2.2.2. Beam squint reduction in series-fed antennas

For series-fed antenna arrays to realize broadside radiation patterns, 0° phase shift between the radiating elements is needed. Usually, this is achieved by adding a phase-shifting network in front of each radiating element to ensure the in-phase feeding. However, traditional phase-shifting networks such as half-wavelength transmission lines only provide a specific phase shift over a very narrow frequency bandwidth, which causes the beam-squint when the array is operating out of this frequency bandwidth.

In series-fed patch resonant antenna, a phase compensating network (Figure 2.10) can be used to realize a low-slope phase response according to [37]. However, after the simulation using the parameters provided by [37] in CST, the low-slope phase response claimed by the article was not realized. The beam squint in series-fed leaky-wave antennas (LWAs) can be reduced by using a one-dimensional negative-refractive-index transmission-line (NRI-TL) phase-shifting line [38]. By using the same NRI-TL structure combined with microstrip technology and a center-fed structure, zero beam squint can be realized in broadside radiation within the operational bandwidth [39]. In addition, folded structure can be used in leaky-wave antennas to reduce the size while having zero beam squint within the operational bandwidth, which is essential in mm-wave applications that requires a compact size of the antenna array designs [40].

In addition to the bean squint reduction techniques in series-fed arrays based on microstrip technology, the beam squint reduction techniques in series-fed arrays based on SIW technology were also been studied in recent years. The beam squint in series-fed leaky-wave antennas based on SIW technology can be reduced by using a several transversely-coupled Fabry-Perot SIW resonant cavities, and keeps the SIW single-layer low-profile in the vertical direction (Figure 2.12) [41]. Moreover, directive squint-free SIW-based series-fed LWA can be realized by using 3-D-shaped dielectric lenses and integrates, in the same substrate, the LWA and a focusing lens with a prism shape [42]. However, such SIW-based LWA structure shown in Figure 2.12 is too wide and is not suitable to construct the array of subarrays.

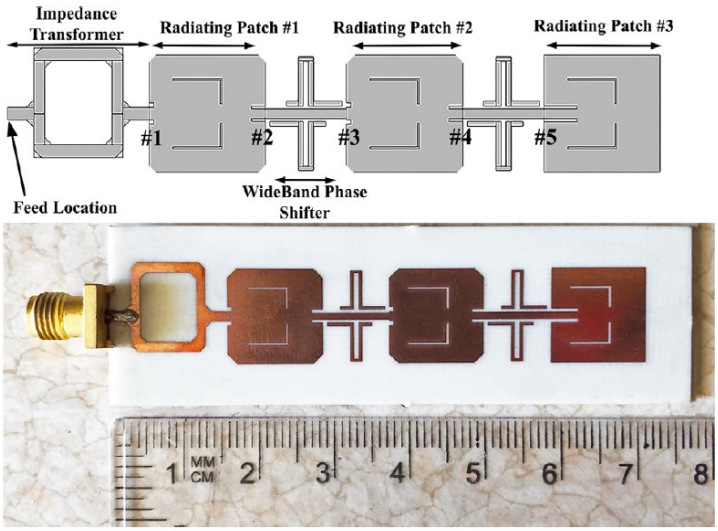

Figure 2.10: Series-fed patch resonant antenna with phase compensating network [37]

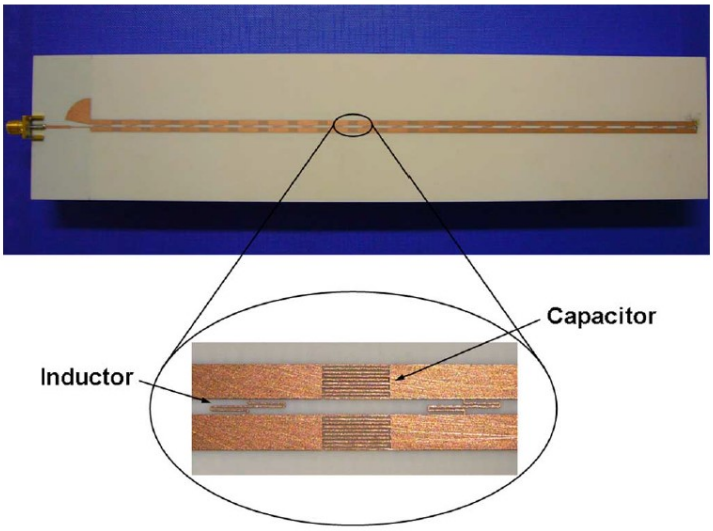

Figure 2.11: Structure of the NRI-TL leaky-wave antenna [38]

Beam squint reduction can also be done through different feeding strategies. There are basically two feeding types in series-fed arrays: edge-fed and center-fed. Usually, the edge-fed configuration is associated with long radiation waveguides, resulting in narrow frequency bandwidth as well as the beam squinting [43]. On the other hand, center-fed antenna arrays can be used to overcome the beam squint problem in edge-fed antenna arrays, due to the halved long line effect and the symmetrical structure [43]. The center-fed configuration can be implemented in series-fed slotted waveguide arrays as shown in Figure 2.13, realizing stable beam direction in broadside [43]. Bandwidth enhancement can also be achieved in SIW-based series-fed slot arrays by using the center-fed structure, both microstrip-to-SIW and coaxial-to-SIW center-fed structures for bandwidth enhancement in slotted arrays were proposed [44, 45]. However, one short-come of the common center-fed structures is the blockage occupied with the feed waveguide in the center of the array aperture which results in a reduction in the efficiency as well as the high sidelobes. To suppress the side-lobe level and reduce the blockage area in the middle of the feeding structure, a compact, parallel co-planar waveguide (CPW) center-fed SIW slot-array was proposed [46]. The middle blockage area can be further eliminated by using a multi-layer center feeding structure, such double-layer SIW-based center-fed slotted array is proposed with no blockage area in the middle and the Taylor amplitude distribution was used for side-lobe level suppression [47].

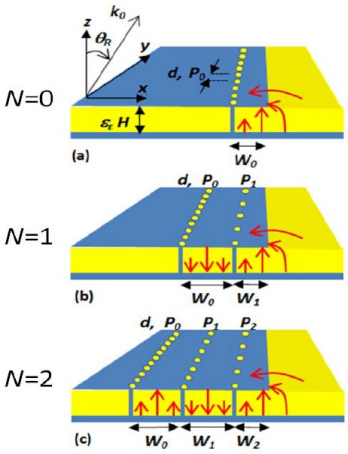

Figure 2.12: LWA structure proposed in [41]

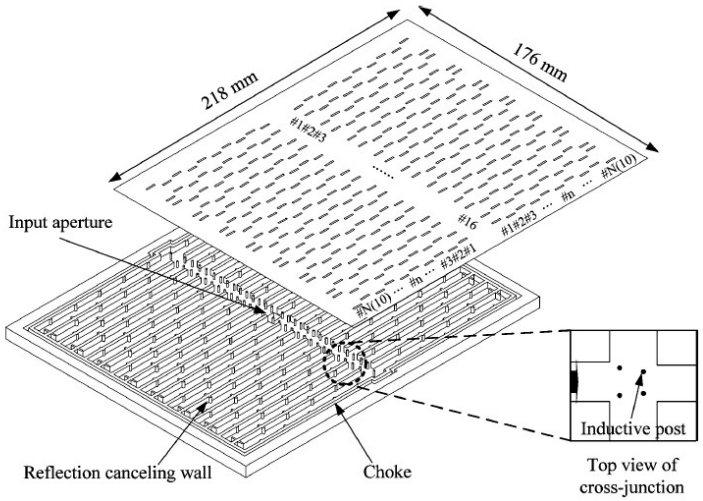

Figure 2.13: Center feed single layer slotted waveguide arrays [43]

A summary of the searched techniques of beam squint reduction in series-fed antennas is listed in Table 2.2, where the term 'Technique' stands for the technique used in that literature for beam squint reduction, the term 'f_0' stands for the center frequency and the term 'BS/BW' indicates the amount of beam squint within the certain bandwidth. It can be seen that among all searched series-fed array designs for beam squint reduction, there is no design for realizing an asymmetrical shaped beam such as the csc^2, which is one of the aims of this thesis research. In addition, despite zero-beam squint being realized in SIW-based leaky-wave antennas, the proposed structures [41, 42] are too complicated to implement and are not flexible for controlling the excitation phase and amplitude for shaped-beam patterns. What's more, up till now there is no design based on SICL technology for beam squint reduction, so, this could be an interesting research topic during the following works of the thesis.

2.3. Conclusions

In this chapter, the state-of-art in series-fed array configurations and beam squint reduction techniques were discussed. It has been shown that the previous research on series-fed array designs mostly focused on broadside radiation patterns including some amplitude tapering such as the Taylor and Dolph-Chebyshev. Only two papers were found which are from MS3 that realized shaped-beam patterns on series-fed antenna arrays and they were all based on SIW technology. So, it is worth investigating the performance of series-fed arrays based on different configurations (microstrip, SIW, SICL) in generating asymmetrically-shaped

Table 2.2: Comparison of different beam squint reduction techniques

Ref	Feeding	Technique	Element No.	Radiator	f_0 (GHz)	Tapering	BS/BW (°/GHz)	Gain (dBi)
[38]	microstrip	NRI-TL	20	strip-line	5	45° from broadside	56/1.8	\
[39]	microstrip	NRI-TL	24	strip-line	5	no tapering	0/1.15	5.3
[40]	microstrip	periodic structure	16	patch	26	no tapering	0/4	15
[41]	SIW	Fabry-Pérot cavities	\	aperture	15	30° from broadside	10/1	12
[42]	SIW	prism lens	\	aperture	34	24° from broadside	1/5	\
[43]	waveguide	center-fed	16x20	slot	25.3	no tapering	0/0.4	30.5
[44]	microstrip-to-SIW	center-fed	8	slot	9.6	no tapering	\	12.13
[45]	coaxial-to-SIW	center-fed	32x16	slot	16.88	Taylor	0/0.4	31.8
[46]	co-planar waveguide	center-fed	4x32	slot	24	Taylor	0/0.2	24
[47]	waveguide-to-SIW	center-fed	8x8	slot	35	Taylor	\	19.94

patterns. For beam squint reduction techniques, it was found that the traditional wide-band phase shifter used to provide constant phase shift over a certain bandwidth is not applicable in series-fed array design for beam squint reduction, due to the phase-dependent between unit cells. For the beam squint techniques in series-fed arrays, most methods found were not suitable for shaped beam pattern synthesis, either because they are not compact in size and too complicated or they are not flexible in controlling the excitation phase and amplitude on each unit cell. Till now, there is no relevant research that focuses on beam squint reduction on the series-fed array that generates shaped-beam patterns. What's more, no SICL-based beam squint reduction technique was found during the research. Despite most of the beam squint reduction techniques are not applicable in series-fed arrays for shaped beam patterns, the center-fed technique has great potential since it doesn't affect the design structure of the radiating components, making it possible to be implemented in the series-fed array designs that realize shaped beam patterns.

3

Edge-fed subarray design

This chapter centres on investigating the performance of edge-fed arrays employing diverse types of unit cells. Initially, the desired pattern shape, along with the requisite amplitude and phase distributions, will be delineated. Subsequently, seven distinct types of unit cells will be elucidated, followed by a comprehensive pattern analysis considering both the mutual coupling effect and its absence. The impact of unit cells on key array parameters, such as beam squint, pattern distortion, bandwidth, and realized gain, will be assessed.

3.1. csc^2 pattern shaping via element excitation control (edge-fed)

To generate the desired radiation pattern and determine the required amplitude and phase distribution for further analysis, a MATLAB code was utilized based on iterative rephasing and projection techniques [7]. In order to optimize the design of the antenna array, the element number and spacing were determined following the procedure outlined in [10], with 12 elements and 0.65 λ_0 spacing being selected and fixed, where the last element functions as a match load [8]. The resulting array factor pattern and its corresponding amplitude and phase distribution for the edge-fed antenna array are depicted in Figure 3.1. Throughout this chapter, all pattern analysis and array design are based on the amplitude and phase distribution presented in Figure 3.1. Detailed values of the excitation phase and amplitude can be found in Table 3.1. The coupling coefficient, which represents the ratio of the radiated power P_{rad} to the input power P_{in}, can be expressed in terms of both the excitation amplitude and the scattering parameters, as illustrated by Equations 3.1 and 3.2, where A denotes the excitation amplitude and N represents the total number of unit cells. The phase difference reflects the phase shift between two neighbouring elements.

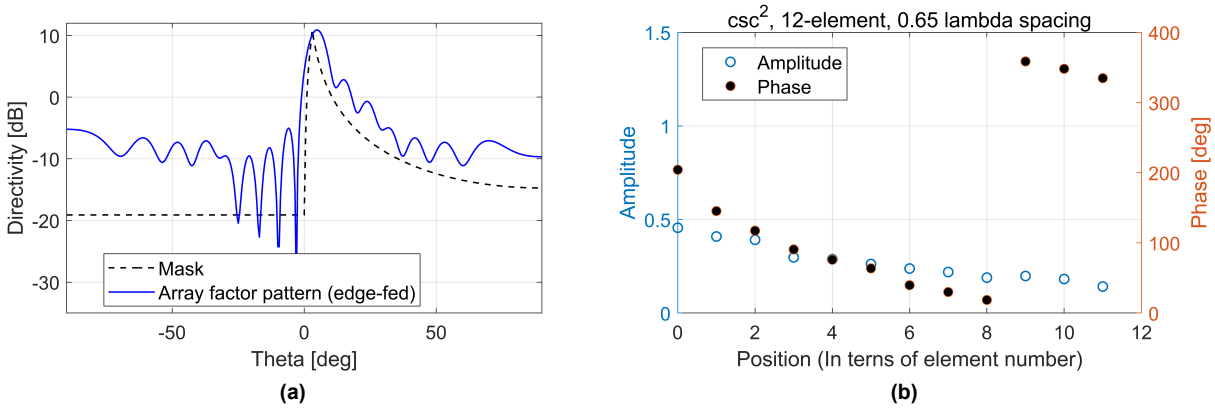

Figure 3.1: csc^2 pattern generation (edge-fed): (a) Array factor pattern, (b) amplitude and phase distribution.

$$C = \frac{P_{rad}}{P_{in}} = \frac{1 - |S_{11}|^2 - |S_{21}|^2}{1 - |S_{11}|^2} \tag{3.1}$$

$$C(n) = \frac{|A(n)|^2}{\sum_{i=n}^{N} |A(i)|^2} \tag{3.2}$$

Table 3.1: Excitation amplitude and phase

Element No.	Coupling coefficient	Phase [deg]	Phase difference [deg]
1	0.2077	204.2085	-58.8591
2	0.2110	145.3494	-28.0064
3	0.2452	117.3430	-26.6993
4	0.1873	90.6437	-14.7326
5	0.2155	75.9111	-12.2862
6	0.2278	63.6249	-24.0019
7	0.2432	39.6230	-9.7568
8	0.2728	29.8662	-11.2806
9	0.2797	19.5857	-19.9455
10	0.4246	358.6402	-10.5357
11	0.6227	348.1044	-13.3050
12	1	334.7995	\

3.2. Design of unit cells

To investigate the influence of unit cell structure on beam squint and pattern distortion, this study examines seven distinct types of unit cells. Each unit cell is designed to possess the same dimensions, with a length of 7.475mm ($0.65\lambda_0$) and a width of 5.75mm ($0.5\lambda_0$). The structure of each unit cell is described in detail in this section. Subsequently, the amplitude and phase distribution of each unit cell, as outlined in Table 3.1, are used to tune the individual units. During the tuning process, the dimensions of 12 individual unit cells are optimized separately in CST Microwave Studio with the Trust Region Framework optimizer. The tuning results of each unit cell are also presented in this section.

3.2.1. SIW-Slot Unit Cell

The SIW-Slot unit cell was initially developed in [10] for the purpose of generating two distinct beam patterns in series-fed antenna arrays. Figure 3.2 illustrates the structure of the SIW-Slot unit cell, which is powered by a substrate integrated waveguide (SIW) structure. The metallic post structure of the SIW as shown in Figure 2.3 is substituted by two metallic walls here to enable fast simulation. The length of the transverse slot regulates the excitation amplitude, while the excitation phase is determined by the radius of the four via holes, which can be filled with the dielectric material. The unit cell's matching is controlled by the location of the two metallic vias on the left side of the slot.

The substrate material with a relative permittivity of 3.37 was employed in the unit cell design, with the via holes filled with high relative permittivity material ($\epsilon_r = 20, \epsilon_r = 30$) to achieve the necessary phase shift [10]. The structure's dimensions are presented in Figure 3.3, with certain parameters having fixed values in millimetres, namely ys=3, ws=0.35, offset=0.75, and dv=0.3. The ground plane and slot layer thickness were both set to 0.02mm, while the substrate thickness was established at 0.76mm. The width of the metallic wall W_{siw} was determined based on the cut-off frequency of the TE10 mode, and was computed using the following equations:

$$f_{cutoff} = \frac{f_0}{1.5} = \frac{26 \cdot 10^9}{1.5} = 17.3\,GHz \tag{3.3}$$

$$c = \frac{c_0}{\sqrt{\epsilon_r}} = \frac{c \cdot 10^8}{\sqrt{3.37}} = 1.634 \cdot 10^8\,m/s \tag{3.4}$$

$$W_{siw} = \frac{c}{2 \cdot f_{cutoff}} = 4.7\,mm \tag{3.5}$$

The tuning result is shown in Figures 3.4 and 3.5. The optimized dimensions are shown in Table 3.2.

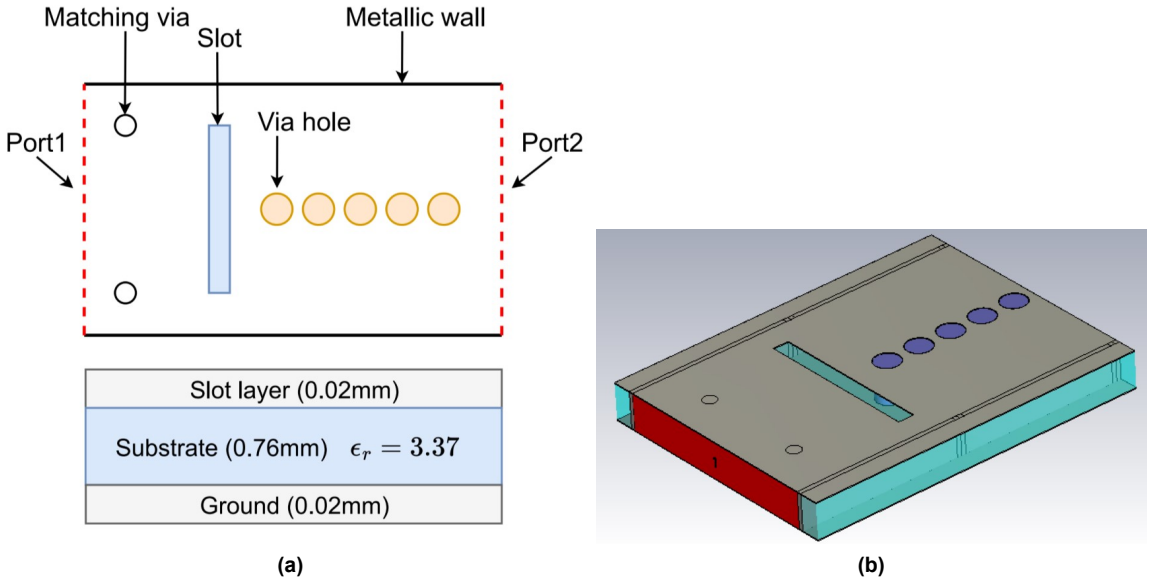

Figure 3.2: SIW-slot unit cell: (a) structure schematic, (b) CST model.

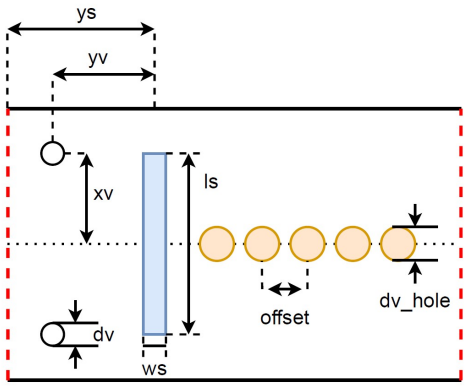

Figure 3.3: SIW-slot unit cell: dimensions

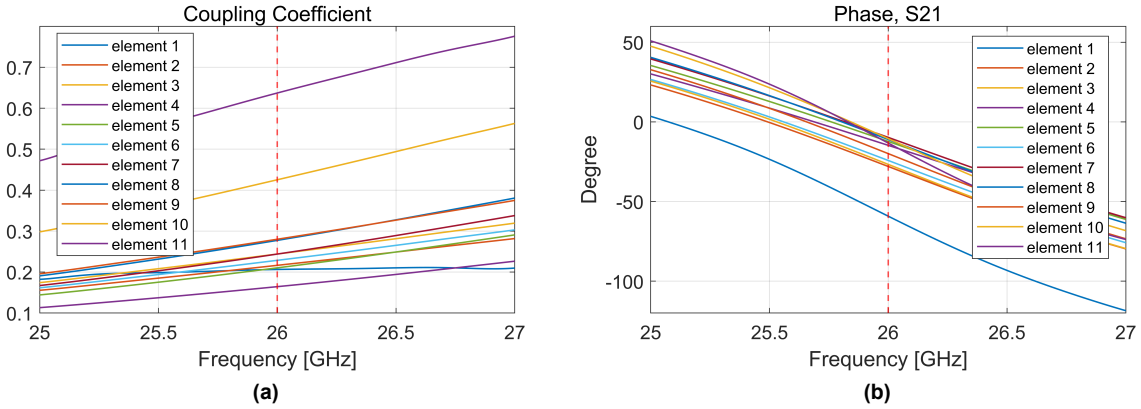

Figure 3.4: SIW-slot unit cell tuning result: (a) coupling coefficient, (b) phase.

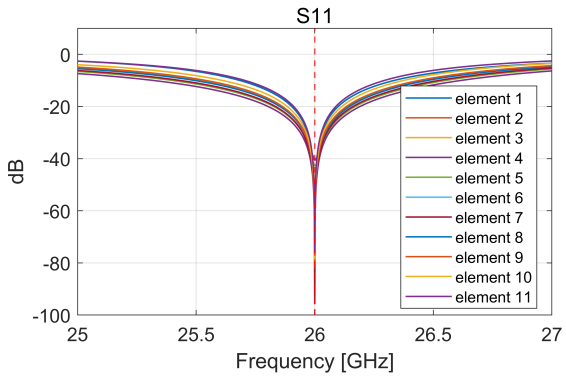

Figure 3.5: SIW-slot unit cell tuning result: S11

Table 3.2: SIW-slot unit cell tuning result: optimized dimensions (in mm)

Element No.	ls	xv	yv	dv_{hole}
1	3.04	1.25	2.31	0.62
2	3.12	1.34	1.27	0.60
3	3.17	1.32	2.25	0.59
4	3.07	1.41	2.24	0.51
5	3.18	1.37	2.21	0.49
6	3.16	1.34	2.25	0.57
7	3.24	1.35	2.18	0.47
8	3.29	1.32	2.17	0.48
9	3.26	1.31	2.21	0.54
10	3.46	1.25	2.12	0.48
11	3.65	1.18	2.06	0.51
12	3.98	1.12	1.96	\

3.2.2. SIW-Slot Unit Cell (with metallic walls)

The SIW-Slot unit cell (with metallic walls), as illustrated in Figure 3.6, features two wall structures on both sides, building upon the structure of the SIW-Slot unit cell. The addition of the wall structure was aimed at

increasing the element gain, improving thermal properties and forming a horn-like radiating element [48]. The width of the wall was established at 4.9mm, with a height of 5mm and a thickness of 0.1mm. The tuning results of the SIW-Slot unit cell (with metallic walls) are depicted in Figures 3.7 and 3.8, with the optimized dimensions presented in Table 3.3.

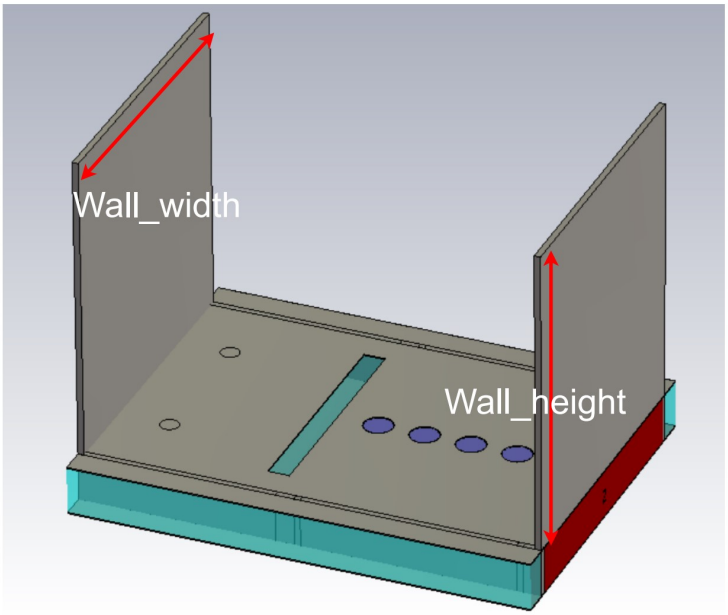

Figure 3.6: SIW-slot unit cell (with metallic walls) model in CST

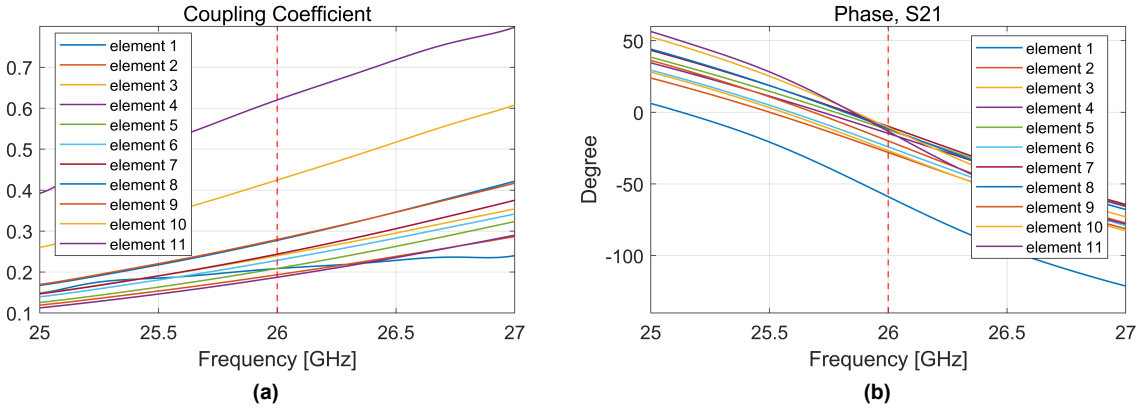

Figure 3.7: SIW-slot unit cell (with metallic walls) tuning result: (a) coupling coefficient, (b) phase.

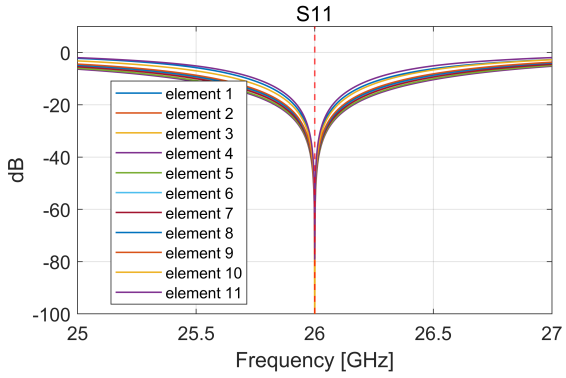

Figure 3.8: SIW-slot unit cell (with metallic walls) tuning result: S11

Table 3.3: SIW-slot unit cell (with metallic walls) tuning result: optimized dimensions (in mm)

Element No.	ls	xv	yv	dv_{hole}
1	3.09	1.24	2.37	0.58
2	3.19	1.34	2.28	0.56
3	3.28	1.31	2.25	0.55
4	3.24	1.37	2.21	0.48
5	3.30	1.35	2.19	0.46
6	3.27	1.32	2.24	0.53
7	3.36	1.32	2.17	0.45
8	3.40	1.29	2.16	0.46
9	3.36	1.29	2.20	0.51
10	3.56	1.22	2.12	0.46
11	3.71	1.15	2.07	0.48
12	3.98	1.12	1.96	\

3.2.3. SIW-Slot-Patch Unit Cell

To improve the gain and the impedance bandwidth of the subarray, the SIW-slot-patch unit cell was developed by adding another patch layer on top of the slot layer of the existing SIW-slot unit cell, while keeping all other parameters unchanged. As reported in [9], this modification leads to more broadband performance. In this unit cell design, the excitation amplitude is regulated by the length of the slot (ls), patch width (wp) and patch length (lp), while the excitation phase is controlled by the radius of the via holes and the dielectric material used to fill them. The structure of the SIW-slot-patch unit cell is depicted in Figure 3.9.

To ensure proper bonding between the patch and slot layers, a dielectric bonding layer with a relative permittivity of 2.7 was inserted in between. The substrate material for the patch layer was selected to be Rogers RT5880, which has a relative permittivity of 2.2. The thickness of the bonding layer was set to 0.096mm, while the thickness of the patch layer's substrate was chosen as 0.508mm. The thickness of the patch itself was set to 0.02mm. The dimensions of the SIW-slot-patch unit cell were tuned in order to reach the required amplitude and phase distribution, and the optimized dimensions are presented in Table 3.4. The tuning results in terms of the coupling coefficient, the phase shift and the reflection coefficient are then depicted in Figures 3.10 and 3.11.

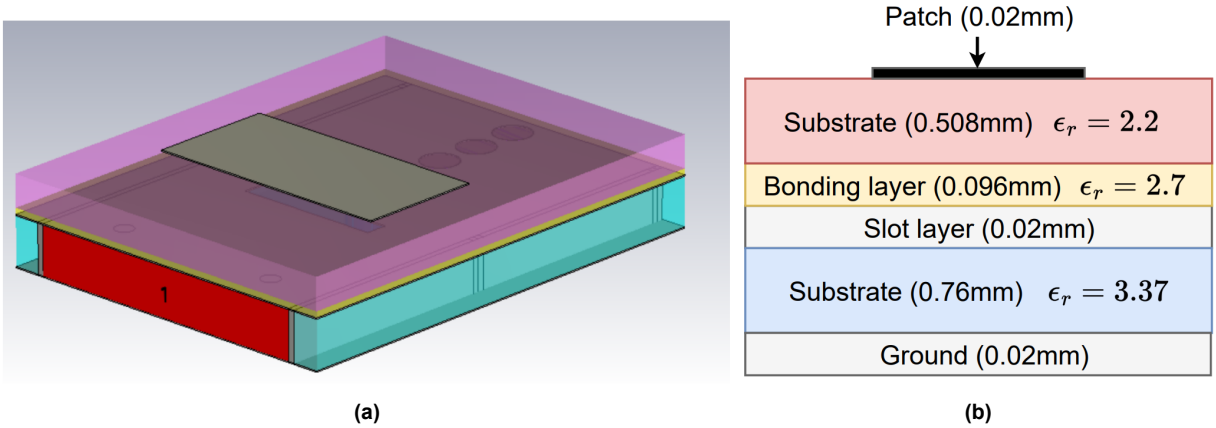

Figure 3.9: SIW-slot-patch unit cell: (a) CST model, (b) layers

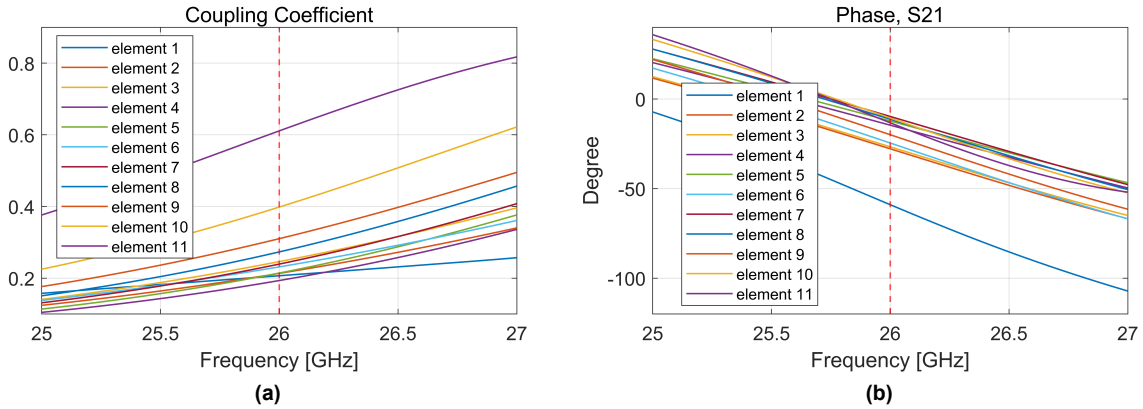

Figure 3.10: SIW-slot-patch unit cell tuning result: (a) coupling coefficient, (b) phase.

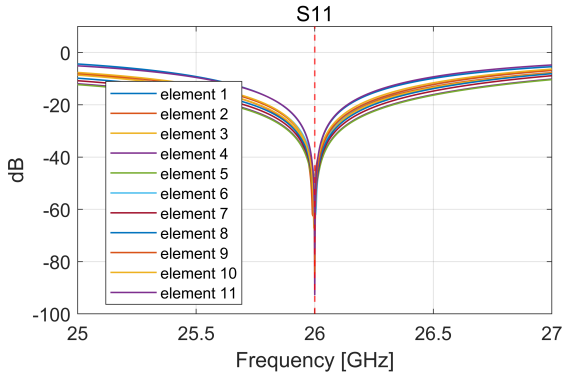

Figure 3.11: SIW-slot-patch unit cell tuning result: S11

Table 3.4: SIW-slot-patch unit cell tuning result: optimized dimensions (in mm)

Element No.	ls	lp	wp	xv	yv	dv_{hole}
1	2.34	1.98	4.00	1.40	2.36	0.59
2	2.34	2.06	4.00	1.55	2.37	0.43
3	2.35	2.13	4.00	1.55	2.33	0.42
4	2.33	2.14	3.77	1.63	2.27	0.36
5	2.33	2.19	2.70	1.64	2.22	0.35
6	2.50	1.76	3.74	1.50	2.30	0.41
7	2.47	1.96	3.34	1.57	2.17	0.34
8	2.51	1.94	3.30	1.54	2.16	0.35
9	2.53	1.90	3.29	1.49	2.20	0.39
10	2.64	1.85	3.15	1.45	2.09	0.35
11	2.78	1.77	3.05	1.36	2.00	0.37
12	2.54	2.78	4.47	2.20	2.62	\

3.2.4. SIW-Slot-Patch Unit Cell (with metallic walls)

As a comparison with the SIW-slot unit cell (with metallic walls), the SIW-slot-patch unit cell (with metallic walls) was designed by adding two metallic walls to the SIW-slot-patch unit cell, as shown in Figure 3.12. The width and height of the walls were set at 4.7mm and 5mm, respectively. The tuning results, including the optimized dimensions, are presented in Figures 3.13 and 3.14 and Table 3.5, respectively.

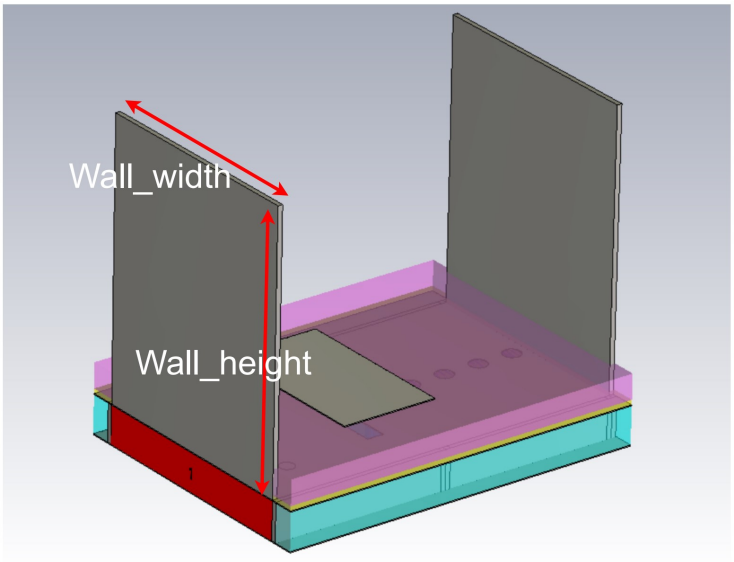

Figure 3.12: SIW-slot-patch unit cell (with metallic walls): model in CST

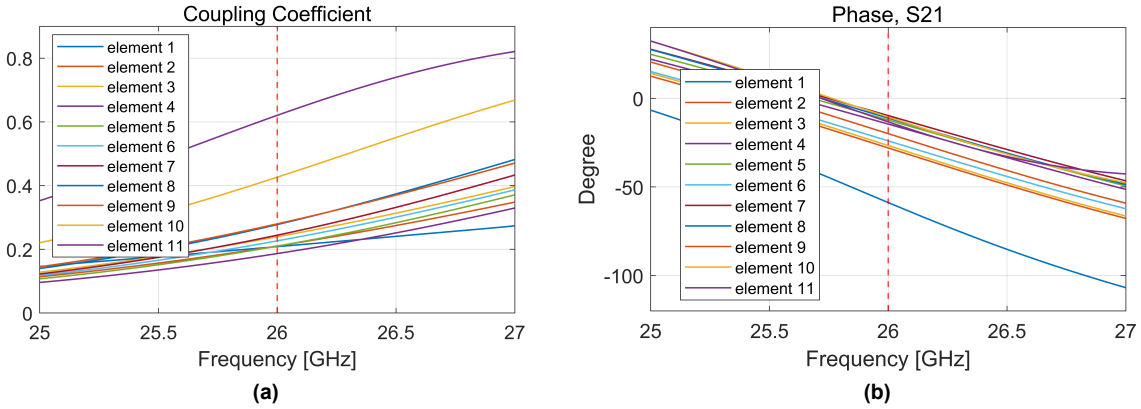

Figure 3.13: SIW-slot-patch unit cell (with metallic walls) tuning result: (a) coupling coefficient, (b) phase.

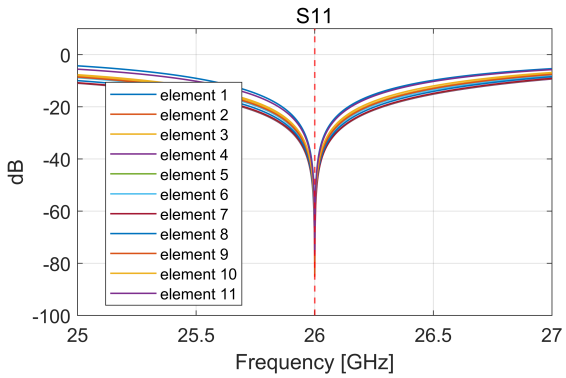

Figure 3.14: SIW-slot-patch unit cell (with metallic walls) tuning result: S11

Table 3.5: SIW-slot-patch unit cell (with metallic walls) tuning result: optimized dimensions (in mm)

Element No.	ls	lp	wp	xv	yv	dv_{hole}
1	2.33	1.96	4.00	1.40	2.36	0.59
2	2.35	1.98	4.00	1.53	2.37	0.43
3	2.40	1.98	3.95	1.53	2.33	0.42
4	2.40	1.92	3.99	1.60	2.26	0.36
5	2.44	1.92	3.94	1.58	2.22	0.35
6	2.36	2.04	3.86	1.55	2.32	0.41
7	2.45	1.99	3.80	1.57	2.17	0.34
8	2.48	1.99	3.76	1.55	2.16	0.35
9	2.47	1.96	3.80	1.52	2.23	0.39
10	2.59	1.98	3.61	1.47	2.06	0.35
11	2.68	1.98	3.46	1.40	1.98	0.37
12	2.54	2.78	4.47	2.20	2.62	\

3.2.5. SICL-Slot-Patch Unit Cell

The SICL-slot-patch unit cell was designed using the SICL technology, which involves a strip line and metallic via holes (replaced by metallic walls for fast simulation) on the sides. The unit cell comprises five layers, with the ground plane at the bottom having a thickness of 0.02mm. The substrate, made from Arlon CuClad 233, is placed on top of the ground plane with a thickness of 0.2mm, and the 50Ω strip line is embedded within it. The PEC slot layer with a thickness of 0.02mm is added on top of the substrate, and the H-shaped slot is embedded within it. A bonding layer, made from a dielectric material with a relative permittivity of 2.7 and a thickness of 0.1mm, is then added on top of the slot layer. A substrate made from Rogers RT5880 (with a relative permittivity of 2.2) is then placed on top of the bonding layer with a thickness of 0.2mm. Finally, the patch made from PEC is placed on top of the structure. The detailed structure of the SICL-slot-patch unit cell is illustrated in Figure 3.15.

The dimensions of the SICL-slot-patch unit cell are presented in Figure 3.18. The excitation amplitude of the unit cell can be controlled by tuning the dimensions of the slot (ls and lh) and the patch (lp and wp). To control the excitation phase, a phase shifter structure based on the strip line is incorporated into the design, where the width of the phase shifter (wps1 and wps2) is tuned to manipulate the excitation phase of the unit cell. Additionally, two radial stubs are added to the strip line to ensure wide-band matching. The unit cell can be matched by tuning the parameters offset_r1, offset_r2, lstub1, lstub2, theta1, and theta2. Some fixed dimensions in the design are w1=2.2mm, w2=5mm, w=0.12mm, offset_ps=3.2mm, lps=0.54mm, ws=0.35mm, and ys=5mm. The tuning results of the SICL-slot-patch unit cell are shown in Figures 3.16 and 3.17, and the optimized dimensions are listed in Table 3.6.

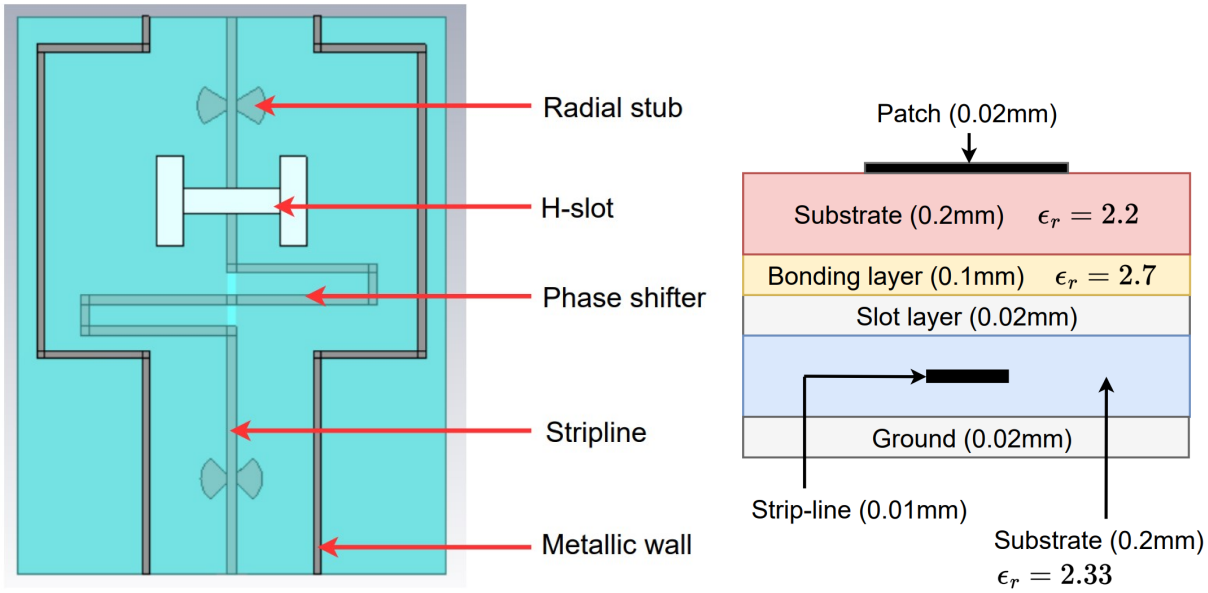

Figure 3.15: SICL-slot-patch unit cell: (a) CST model without the patch layer, (b) layers

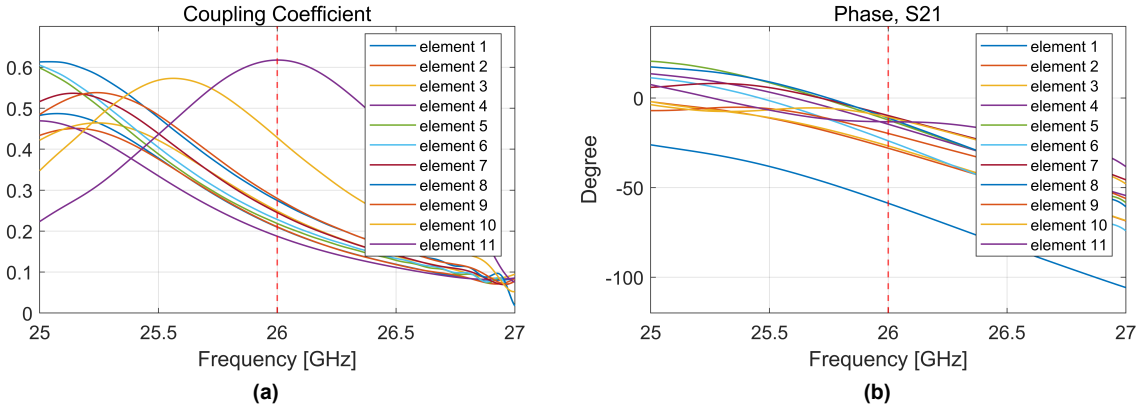

Figure 3.16: SICL-slot-patch unit cell tuning result: (a) coupling coefficient, (b) phase.

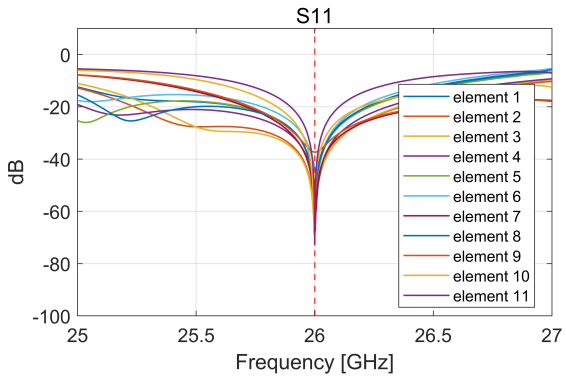

Figure 3.17: SICL-slot-patch unit cell tuning result: S11

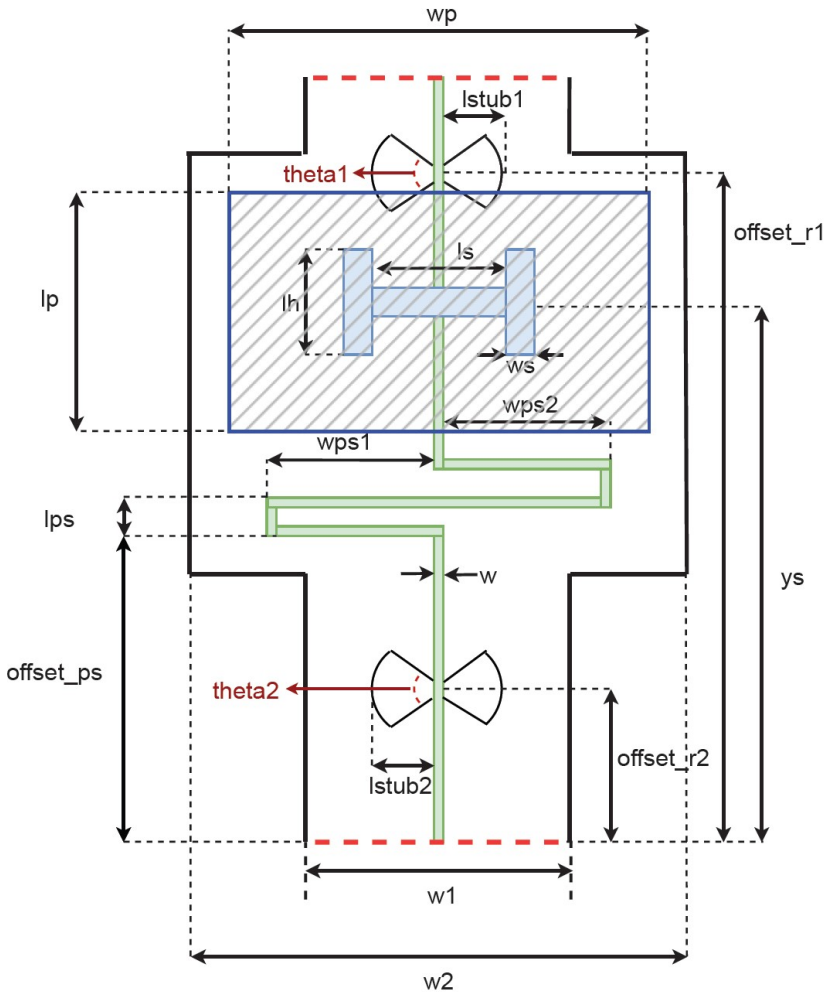

Figure 3.18: SICL-slot-patch unit cell: dimensions

Table 3.6: SICL-slot-patch unit cell tuning result: optimized dimensions (in mm and deg)

No.	ls	lh	wp	lp	wps1	wps2	lstub1	lstub2	offset_r1	offset_r2	theta1	theta2
1	1.01	1.20	3.83	3.47	1.97	1.89	0.40	0.35	6.22	1.22	38.88	50.35
2	1.63	1.03	4.49	3.25	1.93	1.84	0.32	0.29	6.66	1.20	55.27	45.17
3	1.63	1.03	4.49	3.25	1.92	1.84	0.32	0.29	6.66	1.19	55.09	44.97
4	1.66	1.02	4.31	3.29	1.83	1.91	0.28	0.26	6.65	0.99	47.79	43.00
5	1.61	1.08	4.44	3.26	1.69	1.93	0.33	0.28	6.68	0.91	50.03	47.42
6	1.60	1.09	4.54	3.24	1.80	1.90	0.33	0.30	6.74	1.20	54.43	44.35
7	1.56	1.07	4.56	3.24	1.73	1.88	0.31	0.28	6.74	0.97	55.51	47.99
8	1.60	1.09	4.50	3.21	1.77	1.86	0.32	0.28	6.73	1.00	55.71	46.15
9	1.63	1.03	4.67	3.22	1.76	1.91	0.35	0.29	6.68	1.06	50.40	46.74
10	1.73	1.05	4.91	3.11	1.76	1.85	0.36	0.29	6.71	1.05	52.94	44.53
11	1.56	1.33	5.42	2.98	1.74	1.87	0.27	0.29	6.53	1.27	47.16	48.03
12	2.21	0.88	3.83	2.67	\	\	\	0.16	\	1.96	\	29.96

3.2.6. Microstrip-Slot-Patch Unit Cell

The design of the microstrip-slot-patch unit cell comprises a 50Ω microstrip line on the bottom, an H-shaped slot embedded in the middle layer and a patch located on the top layer. The structure of the microstrip-slot-patch unit cell is shown in Figures 3.19 and 3.20. The substrate used in the design is made from Arlon CuClad 233 ($\epsilon_r = 2.33$) with a thickness of 0.2mm. The slot layer and the patch all have the same thickness of 0.02mm.

Figure 3.21 shows the dimensions of the designed microstrip-slot-patch unit cell. In the microstrip-slot-patch unit cell, the excitation amplitude is controlled by tuning the H-shape slot and the patch: ls, lh, lp and wp. The excitation phase can be controlled by tuning the width of the phase shifter: wps1 and wps2. The unit cell matching can be achieved by adjusting the dimensions of the radial stubs (offset_r1, offset_r2, lstub1, lstub2, theta1 and theta2). The design also includes several fixed parameters, including w_feed=0.56mm, l_feed=0.2mm, w=0.12mm, offset_ps=2.9mm, l_ps=0.4mm, ys=5mm and ws=0.35mm.

The tuning result of the microstrip-slot-patch unit cell is shown in Figures 3.22 and 3.23. During the optimization process, some unit cells cannot match well to the center frequency as shown in Figure 3.23 even after extensive iterations using the optimizer. Considering that the pattern shape is not influenced by the matching of the unit cell and to save time, the optimization process of those unit cells for the matching purpose stopped when the -10 dB constraint is met. The optimized dimensions are shown in Table 3.7.

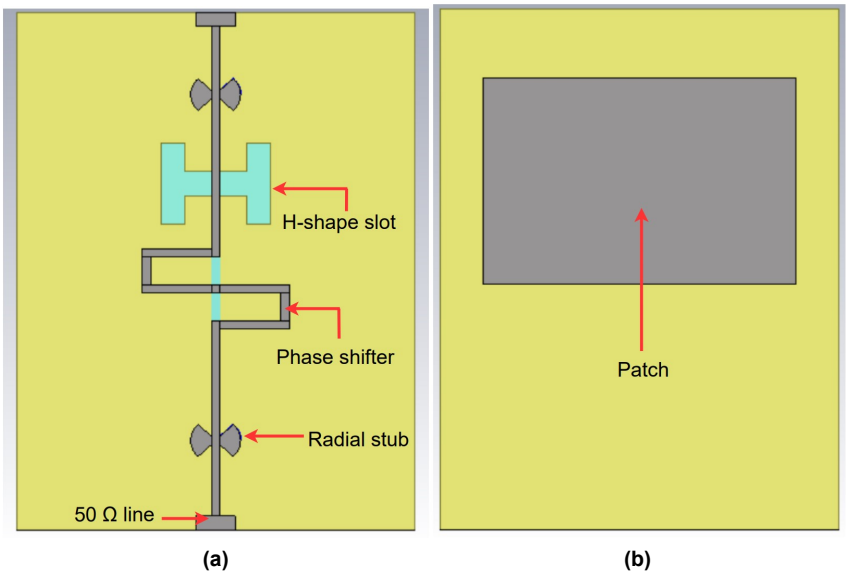

Figure 3.19: Microstrip-slot-patch unit cell structure: (a) bottom view, (b) top view.

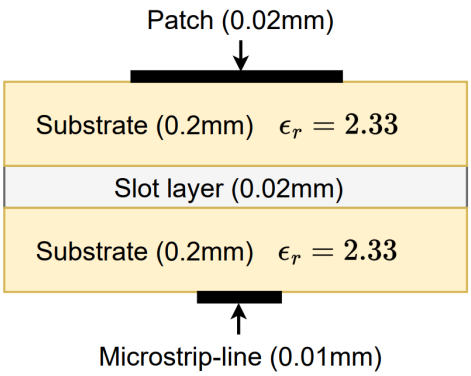

Figure 3.20: Microstrip-slot-patch unit cell structure: layers

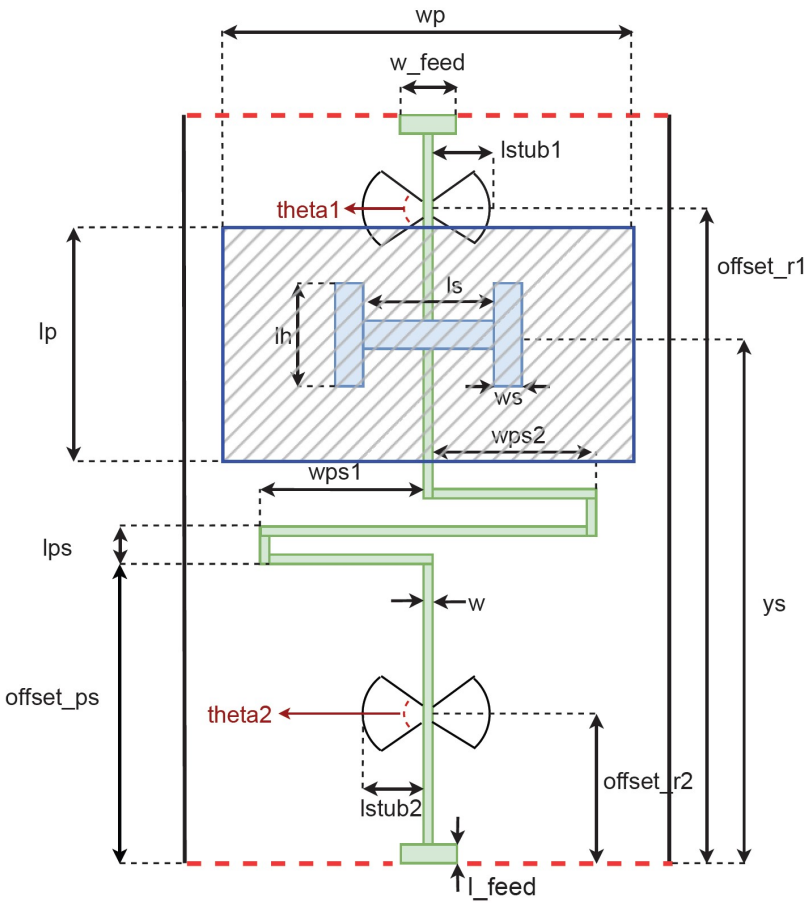

Figure 3.21: Microstrip-slot-patch unit cell: dimensions

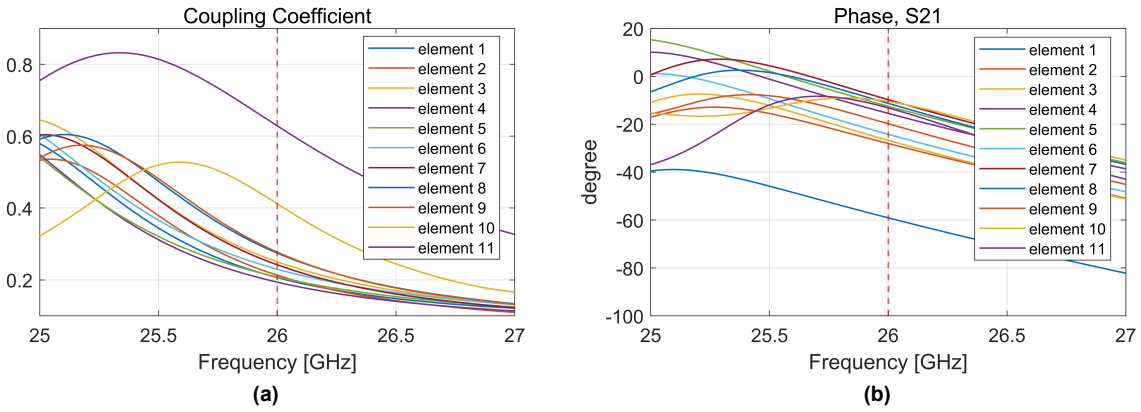

Figure 3.22: Microstrip-slot-patch unit cell tuning result: (a) coupling coefficient, (b) phase.

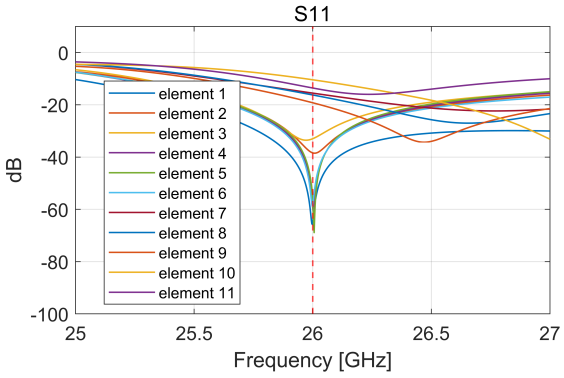

Figure 3.23: Microstrip-slot-patch unit cell tuning result: S11

Table 3.7: Microstrip-slot-patch unit cell tuning result: optimized dimensions (in mm and deg)

No.	ls	lh	wp	lp	wps1	wps2	lstub1	lstub2	offset_r1	offset_r2	theta1	theta2
1	1.42	0.85	4.84	3.33	0.54	0.67	0.33	0.27	6.54	0.89	53.49	49.68
2	1.32	0.96	4.88	3.31	0.57	0.49	0.21	0.15	6.34	0.86	30.50	34.83
3	1.63	0.82	4.54	3.14	0.77	0.31	0.25	0.17	6.45	0.61	31.12	40.37
4	1.63	0.81	4.49	3.20	0.68	0.21	0.24	0.15	6.28	1.39	20.51	20.00
5	1.75	0.81	4.57	3.13	0.65	0.21	0.26	0.15	6.27	0.49	20.68	20.01
6	1.75	0.82	4.59	3.12	0.55	0.50	0.26	0.17	6.49	0.79	37.46	29.35
7	1.60	0.84	4.64	3.17	0.44	0.53	2.00	0.15	6.55	0.54	33.78	27.90
8	1.60	0.56	4.77	3.15	0.32	0.67	0.20	0.15	6.58	0.50	35.67	36.51
9	1.58	0.87	4.82	3.15	0.20	0.88	0.20	0.15	6.80	0.50	41.38	31.03
10	1.42	0.97	5.09	3.17	0.21	0.80	0.15	0.15	6.79	0.50	46.49	42.34
11	1.59	1.16	4.50	2.97	0.71	0.22	0.33	0.12	6.23	1.23	48.07	20
12	1.50	1.09	4.78	2.89	\	\	\	0.32	\	1.34	\	52.60

3.2.7. Proximity-Coupled Unit Cell

The design of the proximity-coupled unit cell is first proposed in [49]. The designed unit cell structure is shown in Figures 3.24 and 3.25. In the proximity-coupled unit cell, the coupling occurs at the end of the first feed line at the open termination upwards to the patch above, then downwards through the substrate to the next feed line below the patch on its other side [49]. The substrate used here is made from Arlon CuClad 233 ($\epsilon_r = 2.33$) with a thickness of 0.508mm. The thickness of the ground plane, strip line and patch is 0.02mm.

The dimensions of the designed proximity-coupled unit cell are shown in Figure 3.26. In the proximity-coupled unit cell, the excitation amplitude is controlled by the width of the patch wp. The excitation phase is controlled by tuning the width of the phase shifter wps1 and wps2. The matching of the unit cell to the desired can be done by tuning the length of the open termination sl, and dimensions of two radial stubs: offset_r1, offset_r2, lstub1, lstub2, theta1 and theta2. Some fixed parameters of the unit cell are: l_feed=0.2mm, w_feed=0.32mm, w=0.12mm, offset_ps=2.4mm, ys=5mm and lps=0.2mm.

The tuning results of the proximity-coupled unit cell are shown in Figures 3.27 and 3.28. The optimized dimensions are listed in Table 3.8.

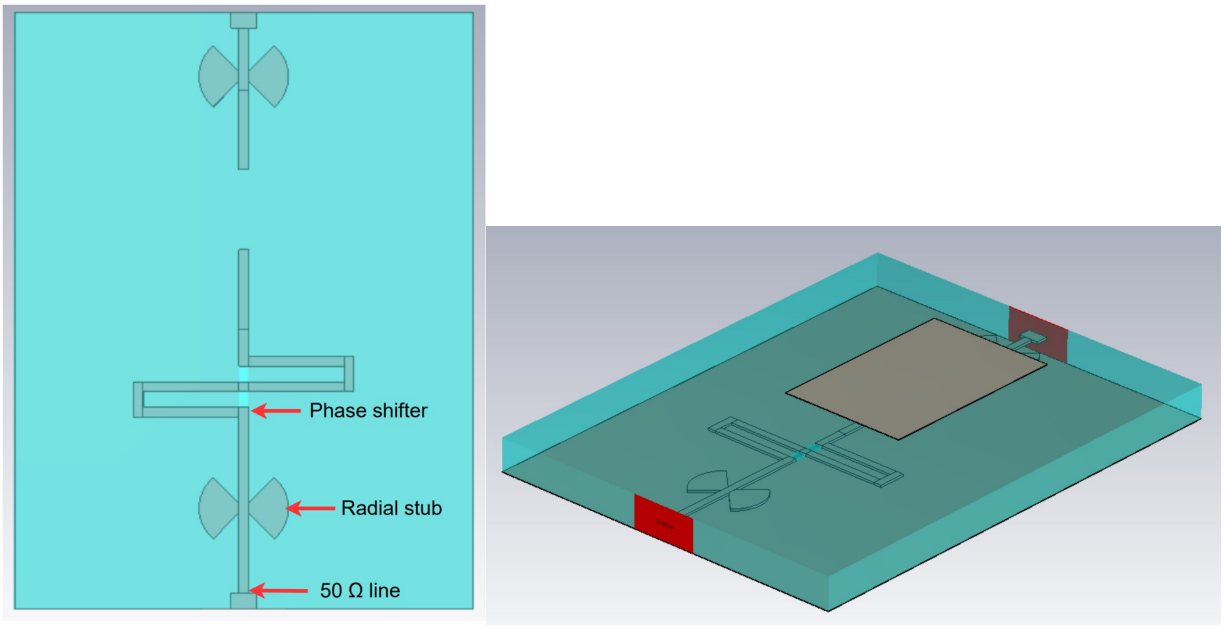

Figure 3.24: Proximity-Coupled unit cell structure: (a) top view (without patch), (b) side view.

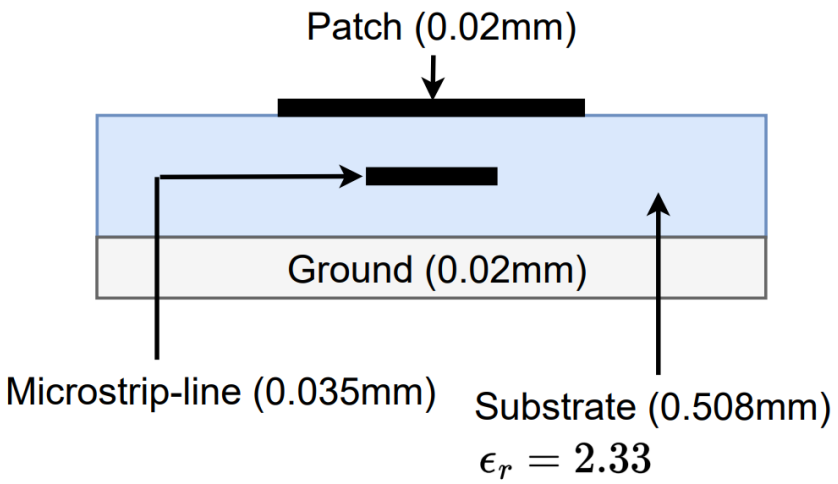

Figure 3.25: Proximity-Coupled unit cell structure: layers

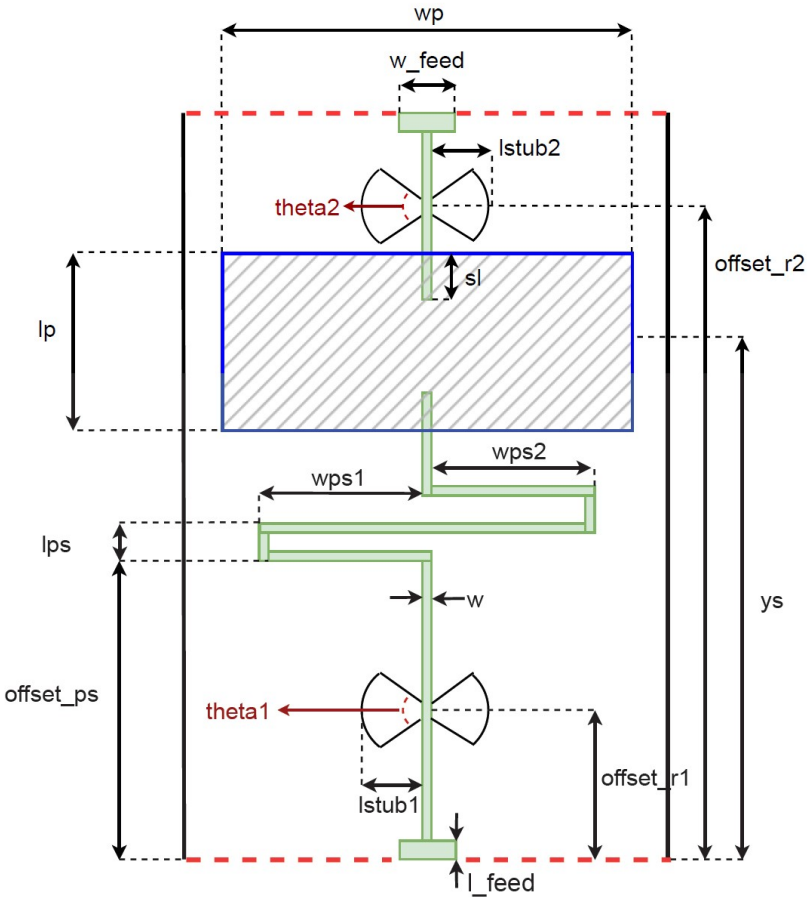

Figure 3.26: Proximity-Coupled unit cell: dimensions

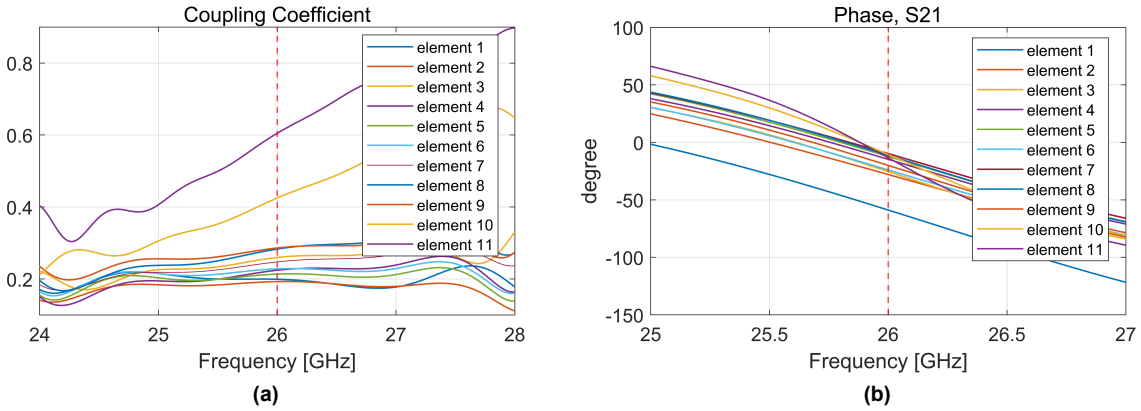

Figure 3.27: Proximity-Coupled unit cell tuning result: (a) coupling coefficient, (b) phase.

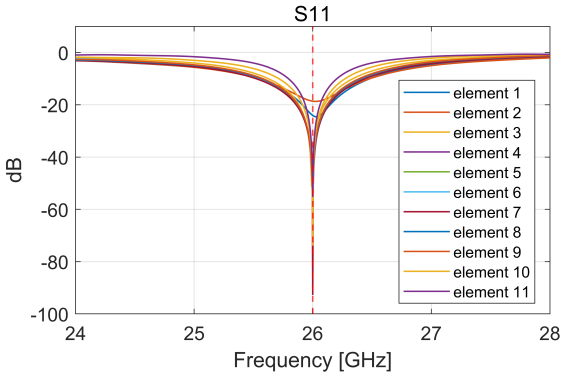

Figure 3.28: Proximity-Coupled unit cell tuning result: S11

Table 3.8: Proximity-Coupled unit cell tuning result: optimized dimensions (in mm and deg)

No.	sl	wp	lp	wps1	wps2	lstub1	lstub2	offset_r1	offset_r2	theta1	theta2
1	1.50	0.30	3.81	1.84	2.28	0.11	0.60	1.74	6.87	37.14	49.51
2	1.50	0.94	3.81	1.74	1.89	0.28	0.29	1.62	6.21	42.99	36.16
3	1.50	1.12	3.81	1.80	1.70	0.39	0.31	1.46	6.52	44.67	35.21
4	1.50	0.64	3.81	2.03	1.62	0.25	0.32	1.64	6.60	51.86	34.91
5	1.50	0.87	3.81	1.95	1.56	0.36	0.22	1.44	6.60	56.29	36.28
6	1.50	0.99	3.81	1.98	1.59	0.33	0.25	1.53	6.19	48.42	32.36
7	1.57	1.50	3.81	1.64	1.42	0.57	0.38	0.73	6.22	52.43	51.38
8	1.57	1.50	3.81	1.58	1.48	0.56	0.40	0.73	6.22	52.62	53.54
9	1.57	1.50	3.81	1.89	1.27	0.59	0.43	0.92	6.50	54.94	47.00
10	1.57	2.22	3.81	1.00	1.93	0.70	0.38	0.70	7.00	59.99	46.40
11	1.60	3.02	3.60	1.04	1.81	0.66	0.39	0.75	6.61	56.74	58.88
12	0.81	2.92	3.39	\	\	0.53	\	1.09	\	48.06	\

3.2.8. Conclusion - Edge-fed unit cell design

In this section, seven different unit cells were designed and tuned to the amplitude and phase distribution listed in Table 3.1. Three properties of each unit cell that depends on the frequency are plotted which are the reflection coefficient S11, the coupling coefficient and the phase shift. After comparing the performance of different unit cell structures, a summary is made in the following paragraph.

When considering the reflection coefficient S11, the Microstrip-slot-patch unit cell shows the widest bandwidth which is about 4.8 GHz. While the narrowest bandwidth appears in the SIW-slot unit cell which is about 600 MHz. The possible reason is the radial stub applied in the design of the microstrip-slot-patch unit cell which ensures a large bandwidth, on the other hand, the SIW feeding structure in the SIW-slot unit cell results in a narrow bandwidth. For the coupling coefficient, the proximity-coupled unit cell shows the flattest curve of the coupling coefficient versus the frequency, this is because the excitation amplitude of the proximity-coupled unit cell only depends on the width of the patch. Since the pattern shape distortion is mostly due to the change of the excitation amplitude with frequency, a flat curve of the coupling coefficient can probably lead to a stable pattern shape in a subarray. Last but not least, the microstrip-slot-patch unit cell shows the flattest phase response with respect to the frequency. Since the beam squint is mainly caused by the change of the phase shift over the frequency, the microstrip-slot-patch unit cell can probably lead to the smallest beam squint among the other unit cell structures.

In the following sections, the subarray patterns will be analysed without considering the mutual coupling effect, in order to see the performance of the unit cell structure itself. Then, the complete subarray will be simulated in CST to obtain the patterns including the mutual coupling effect.

3.3. Pattern analysis without mutual coupling effect

In this section, the radiation pattern of the subarray without considering the mutual coupling effect will be analyzed for seven unit cell structures. The subarrays' performance in pattern distortion and beam squint will be analyzed and compared. The radiation pattern without mutual coupling $|E^{rad}|$ can be simply obtained using Equation 3.6, where A(n) and β(n-1) are the excitation coefficient and phase shift of the n-th unit cell at the measured frequency (β(0) = 0 as reference), k is the propagation constant, d is the spacing between the unit cells and $|E^{el}(\theta)|$ is the isolated radiation pattern of the first unit cell in each subarray type.

$$|E^{rad}(\theta)| = |E^{el}(\theta)||\sum_{n=1}^{12} A(n)e^{j(kd\sin\theta+\beta(n-1))}| \tag{3.6}$$

The subarray patterns were calculated from 25.2 GHz to 26.8 GHz with 0.2 GHz steps. The input excitation amplitude $A(n)$ and phase $\beta(n)$ to the array factor in 3.6 were directly obtained from the tuning result of each type of unit cell. As a reference, the synthesized pattern $|E^{syn}|$ is obtained by scaling the array factor pattern in Figure 3.1 with $|E^{el}(\theta)|$. To quantify the pattern distortion between the subarray pattern $|E^{rad}|$ and the synthesized pattern $|E^{syn}|$, an RMS error function (RMSE) shown in Equation 3.7 was used [50]. The comparison was done in the 0° to 90° range of the csc^2 pattern shape. The main-lobe direction of the realized pattern was aligned with the synthesized pattern (giving E'^{rad}), and both patterns are normalized in 3.7 to quantify the shape distortions only.

$$RMSE = \sqrt{\frac{\sum_{\theta=0}^{90} |\frac{|E^{syn}(\theta)|}{max|E^{syn}(\theta)|} - \frac{|E'^{rad}(\theta)|}{max|E^{rad}(\theta)|}|^2}{\sum_{\theta=0}^{90} |\frac{E^{syn}(\theta)}{maxE^{syn}(\theta)}|^2}} \tag{3.7}$$

After analysing the subarray patterns, it was found that the smoothness of the pattern is related to the excitation amplitude. Figures 3.29 to 3.32 show the subarray patterns, the excitation amplitude and the phase shift of two unit cell structures (SIW-slot-patch and SICL-slot-patch) operated at 25.2GHz and 26.8GHz. By comparing the radiation patterns of two types of unit cells at the same frequency, it can be seen that at 25.2 GHz, the SICL-slot-patch unit cell shows a smoother radiation pattern than the SIW-slot-patch unit cell, while at 26.8 GHz it is the other way around. Since the phase shift distributions of two unit cells at the same frequency show a similar trend compared to the desired phase shift distribution, the smoothness of the radiation pattern is probably related to the excitation amplitude. By comparing the excitation amplitude of the two unit cells at the same frequency, it was found that for a smooth radiation pattern, the value of the tuned excitation amplitude is higher than the desired value. To obtain a smooth radiation pattern, the actual excitation amplitude distribution should be greater or equal to the desired value. For the beam squint in the radiation pattern, it can be seen that when the slope of the actual excitation phase is higher than the desired one, the main lobe direction is shifted to the right, and when the slope of the actual excitation phase is lower than the desired one, the main lobe direction is shifted to the left.

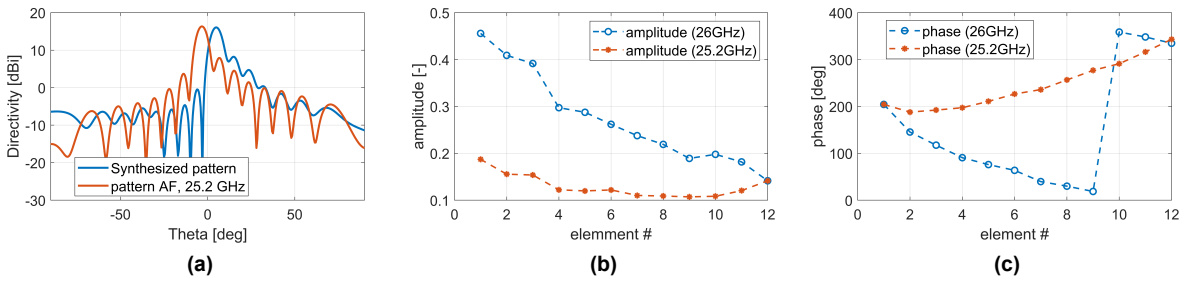

Figure 3.29: Subarray pattern analysis for SIW-slot-patch unit cell at 25.2GHz: (a) radiation pattern, (b) excitation amplitude, (c) phase shift.

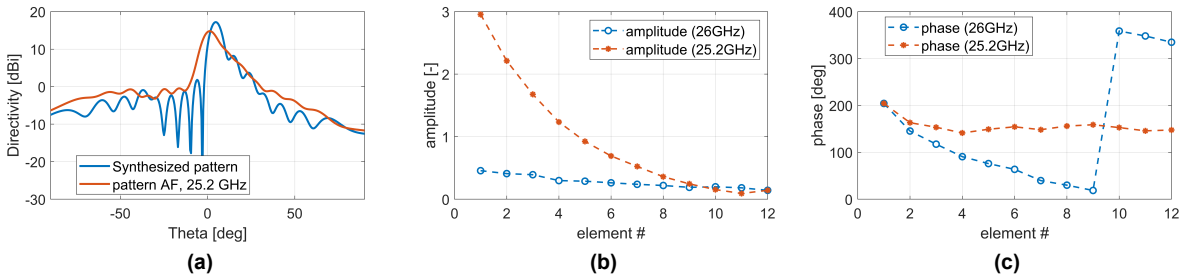

Figure 3.30: Subarray pattern analysis for SICL-slot-patch unit cell at 25.2GHz: (a) radiation pattern, (b) excitation amplitude, (c) phase shift.

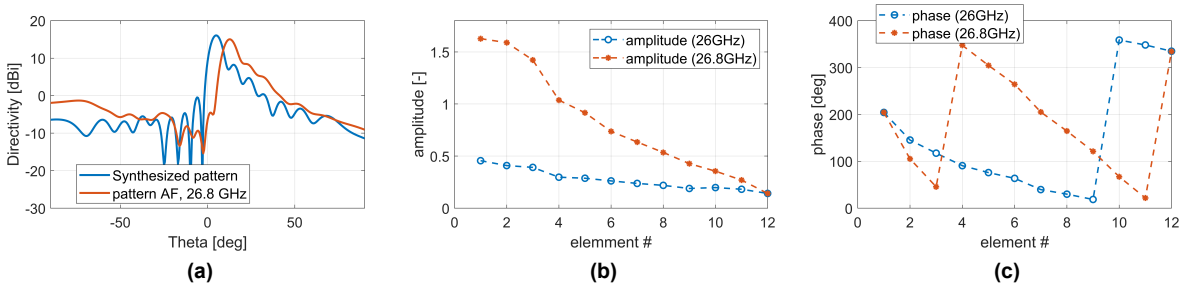

Figure 3.31: Subarray pattern analysis for SIW-slot-patch unit cell at 26.8GHz: (a) radiation pattern, (b) excitation amplitude, (c) phase shift.

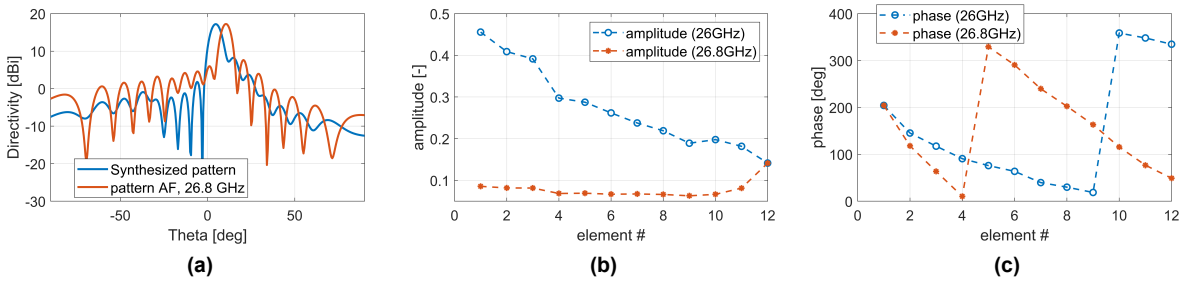

Figure 3.32: Subarray pattern analysis for SICL-slot-patch unit cell at 26.8GHz: (a) radiation pattern, (b) excitation amplitude, (c) phase shift.

Figure 3.33 compares the subarray patterns from seven unit cell structures in beam squint and pattern distortion. The microstrip-slot-patch unit cell shows the smallest amount of beam squint, which is about $\pm 4°$ within $\pm 800MHz$ frequency range. While the proximity-coupled unit cell shows the largest amount of beam squint, which is about $\pm 10°$ within $\pm 800MHz$ frequency range. Besides, the SICL-slot-patch unit cell shows the second smallest amount of beam squint which is quite close to the performance of the microstrip-slot-patch unit cell. For the pattern distortion, the best matching appears on the SIW-slot unit cell and the SIW-slot-fin unit cell, however, the matching gets worse when the operating frequency is shifted from the centre frequency. The proximity-coupled unit cell shows the most stable radiation patterns with only 7.7% error on average within the evaluated bandwidth.

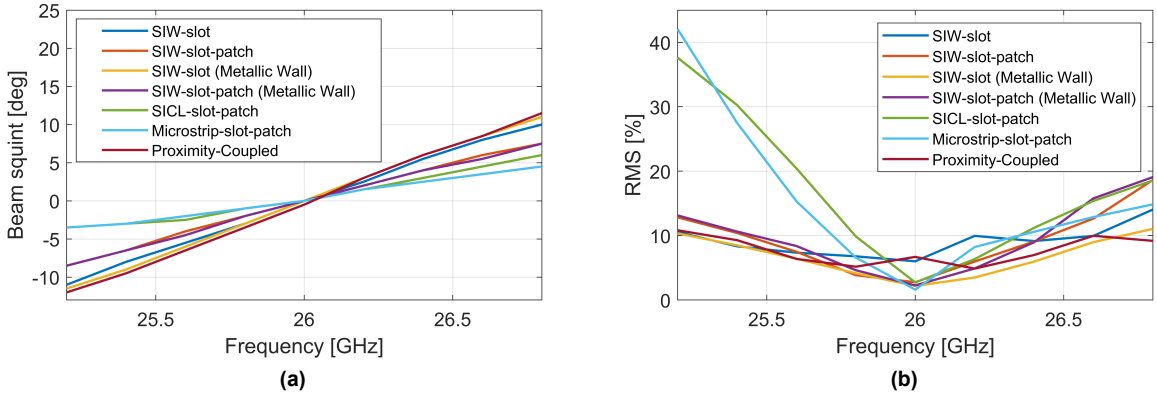

Figure 3.33: Subarray patterns comparison without coupling: (a) beam squint, (b) pattern distortion.

In conclusion, after analysing the subarray radiation patterns using the array factor, the microstrip-slot-patch unit cell and the SICL-slot-patch unit cell show good performance in beam squint reduction compared to the others. For pattern distortion reduction, the proximity-coupled unit cell shows the most stable radiation pattern and thus has great potential for pattern distortion reduction in subarray design.

3.4. Pattern analysis with mutual coupling effect

In this section, the patterns of the subarrays are analyzed including the mutual-coupling effect by simulating the complete subarray structure in CST. Figure 3.34 shows the CST model of the 12-element subarray based on the SIW-slot unit cell and the SIW-slot unit cell with metallic walls. All patterns were obtained from 25.2 GHz to 26.8 GHz with a 0.2 GHz step. Figures 3.35 to 3.41 show the subarray patterns compared with the synthesized pattern under three different frequencies. By comparing Figure 3.35 and 3.36, it can be seen that after adding the metallic walls to the SIW-slot subarray, the pattern becomes smoother and there is less ripple. The same situation can be found in Figures 3.37 and 3.38. It shows the wall structure can reduce the pattern distortion and improve the pattern shape but only around the centre frequency.

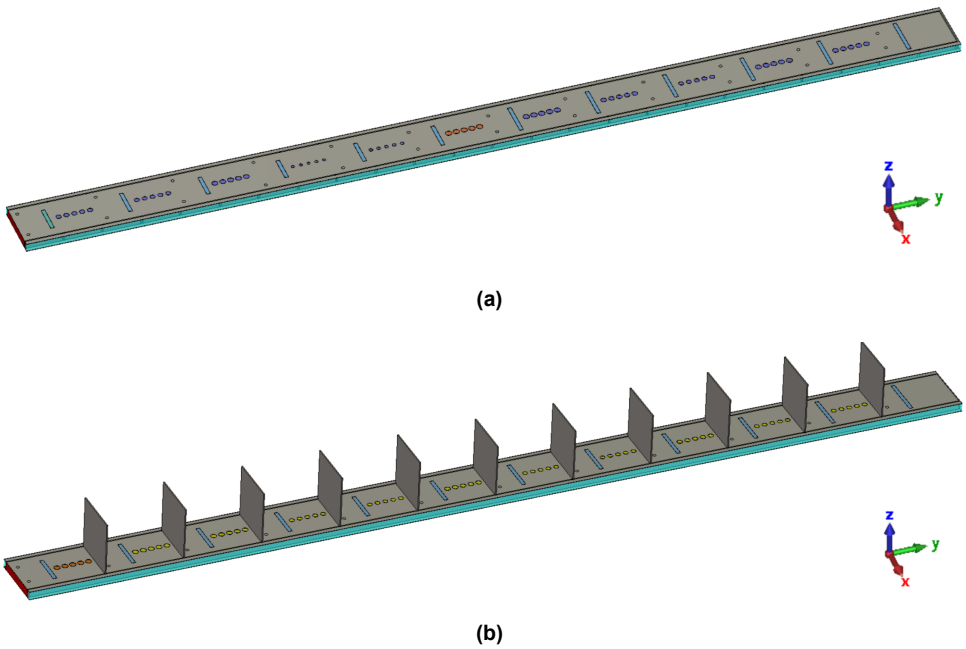

Figure 3.34: Edge-fed series-fed subarray models in CST: (a) SIW-slot subarray, (b) SIW-slot subarray with metallic walls.

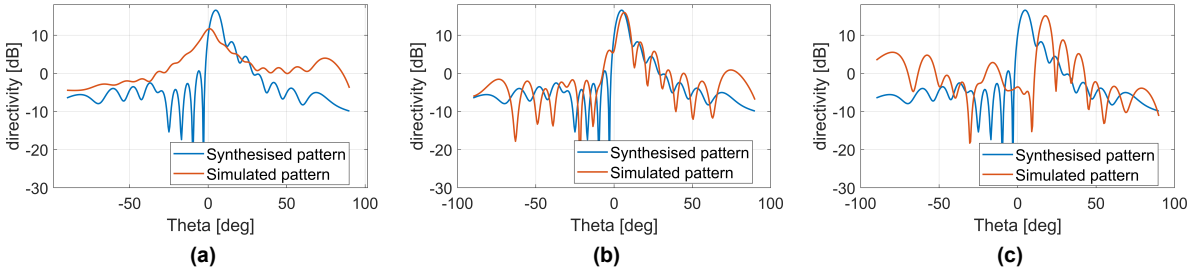

Figure 3.35: Radiation patterns of the SIW-slot subarray: (a) 25.2GHz, (b) 26GHz, (c) 26.8GHz.

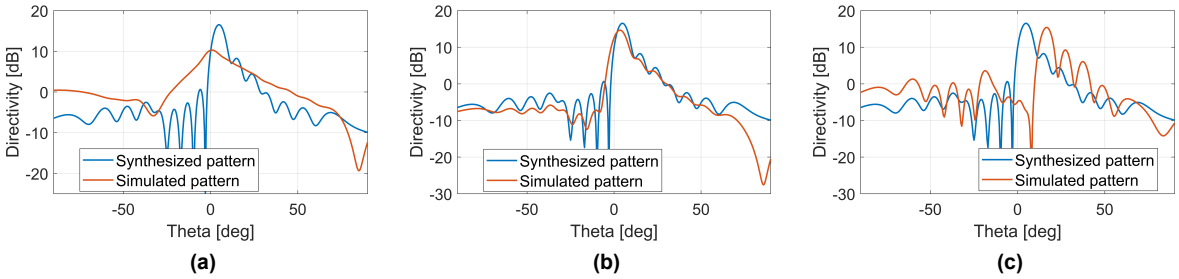

Figure 3.36: Radiation patterns of the SIW-slot (Metallic Wall) subarray: (a) 25.2GHz, (b) 26GHz, (c) 26.8GHz.

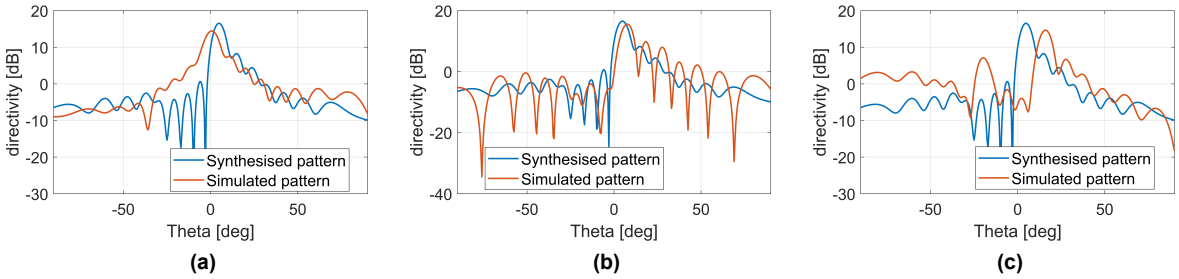

Figure 3.37: Radiation patterns of the SIW-slot-patch subarray: (a) 25.2GHz, (b) 26GHz, (c) 26.8GHz.

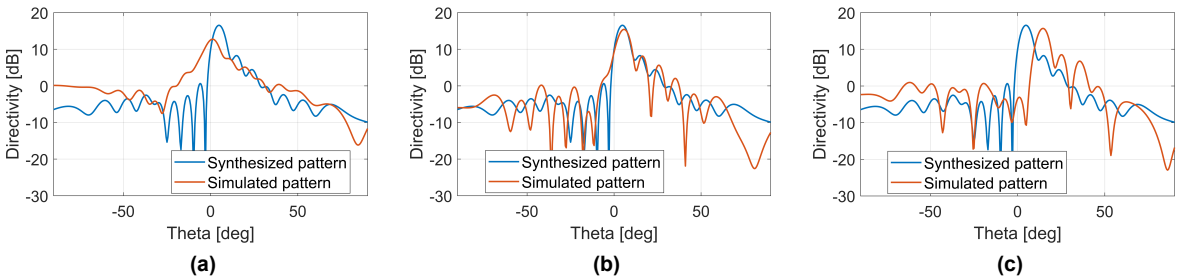

Figure 3.38: Radiation patterns of the SIW-slot-patch (Metallic Wall) subarray: (a) 25.2GHz, (b) 26GHz, (c) 26.8GHz.

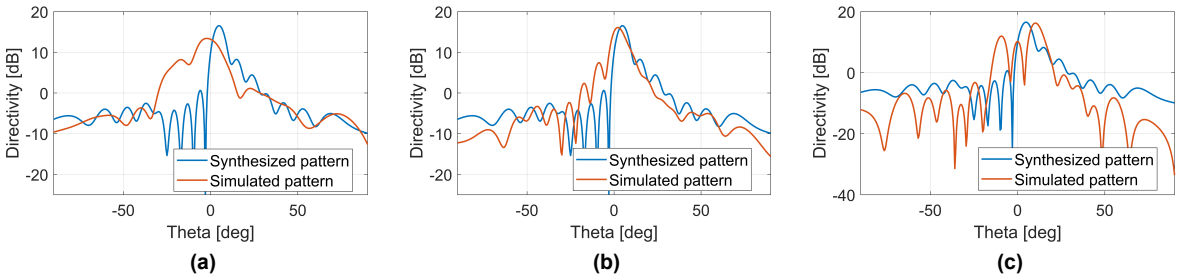

Figure 3.39: Radiation patterns of the SICL-slot-patch subarray: (a) 25.2GHz, (b) 26GHz, (c) 26.8GHz.

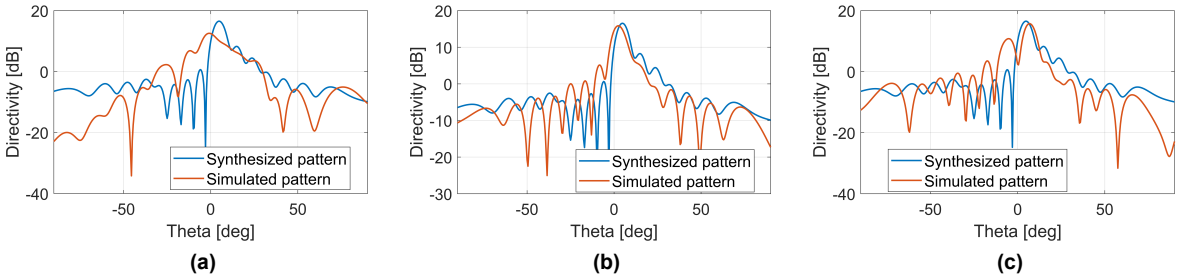

Figure 3.40: Radiation patterns of the microstrip-slot-patch subarray: (a) 25.2GHz, (b) 26GHz, (c) 26.8GHz.

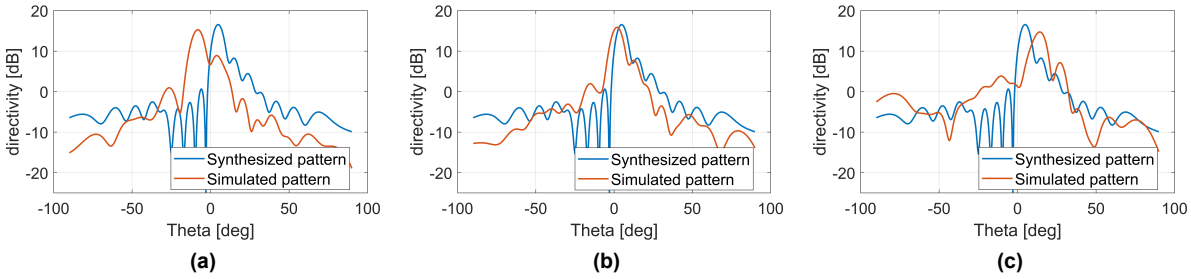

Figure 3.41: Radiation patterns of the proximity-coupled subarray: (a) 25.2GHz, (b) 26GHz, (c) 26.8GHz.

Figure 3.42 shows the amount of beam squint and pattern distortion of seven subarrays. The pattern distortion was again measured by using the equation 3.7. Compared with the situation without the mutual-coupling effect, the pattern distortion increased two times in terms of the RMS value after considering the mutual-coupling effect. On the other hand, the amount of the beam squint is less affected by the mutual-coupling effect. It can be seen that among all seven subarrays, the microstrip-slot-patch subarray shows the least amount of beam squint, ranging from -6° to 2° within the simulated 6% frequency range. For the pattern distortion, the proximity-coupled subarray again shows the most stable patterns among all subarrays, with 15.7% average error compared to the synthesized pattern from 25.2 GHz to 26.8 GHz.

Figure 3.43 shows the reflection coefficient and the realized gain of seven subarrays. Among all seven subarrays, the SICL-slot-patch subarray shows the largest bandwidth which is about 1.9 GHz. On the other hand, the bandwidth of the SIW-slot subarray with metallic walls is the smallest of the seven subarrays which is about 500 MHz and as a result, the SIW-slot subarray with metallic walls also performs the worst of the seven subarrays in terms of realized gain, with a variation from -0.95 dBi to 15.46 dBi within the simulated bandwidth. In addition, the proximity-coupled subarray shows the most steady realized gain among the seven subarrays, with less than 1.5 dB variation within the evaluated bandwidth.

The cross-polarization level is an important parameter in base station antenna design, especially when the base station is aiming to send different data streams with different polarizations to increase the data rate and capacity. Although the optimization of the cross-polarization level is not included in this research, the cross-polarization (horizontal) level of the seven subarrays is still measured from the simulation results. It is observed that the cross-polarization levels of the SIW-slot subarray, the SIW-slot-fin subarray and the SICL-slot-patch subarray are all below -60 dBi in the beamforming plane. The cross-polarization levels of the SIW-slot-patch subarray and the SIW-slot-patch-fin subarray are all below -40 dBi in the beamforming plane, while the cross-polarization level of the microstrip-slot-patch subarray is lower than -20 dBi in the beamforming plane. However, the cross-polarization level of the proximity-coupled subarray is relatively high (above 0 dBi) which is caused by the current flows on the phase shifter which has a perpendicular direction related to the current flows on the patch. The cross-polarization level on the proximity-coupled subarray is reduced in Chapter 4 by using a shorter phase shifter during the design of the center-fed subarray.

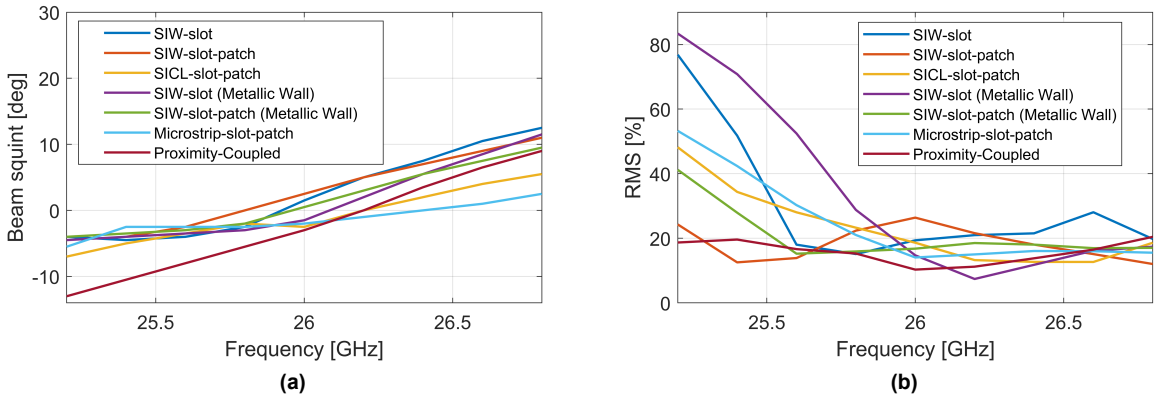

Figure 3.42: Subarray patterns analysis: (a) Beam squint, (b) pattern distortion.

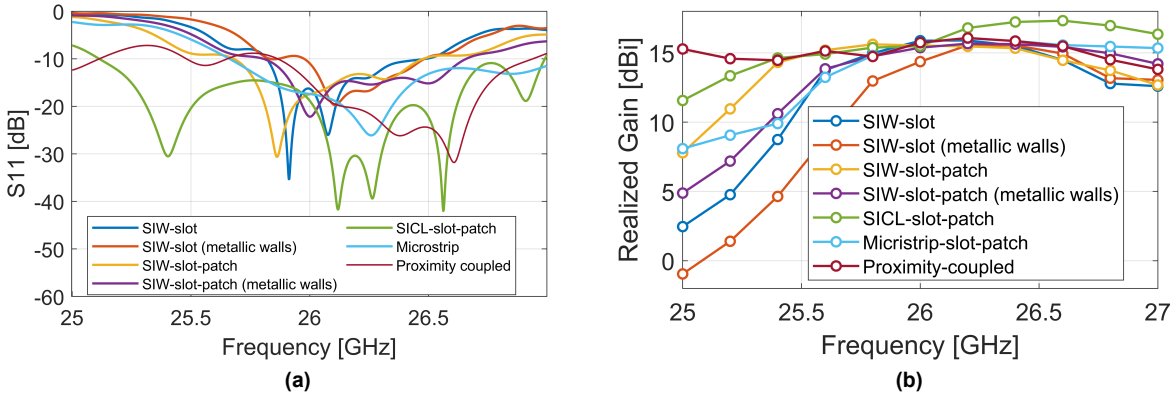

Figure 3.43: Subarray performance analysis: (a) S11, (b) realized gain.

3.5. Unit cell tuning with the presence of neighbouring unit cells

In previous sections, the unit cells are tuned under the isolated condition. In this section, to further minimize the influence of the mutual-coupling effect, the unit cell is tuned with the presence of other elements. By doing so, part of the mutual-coupling effect can be taken into account during the optimization process. To save the simulation time, only the SIW-slot unit cell will be investigated in this section.

Figure 3.44 shows the CST model where the unit cell is optimized under the presence of two neighbouring elements. As shown in Figure 3.44a, when the target unit cell is located in the middle of the subarray, it is tuned with two neighbouring elements before and after it. The electromagnetic wave is then excited from port-1 (marked with yellow) and absorbed at port-2 (marked with red). When the target unit cell is located on the side of the subarray, as shown in Figure 3.44b, it is tuned with two neighbouring elements after it. In order to investigate the influence of the number of iterations and the number of neighbouring elements present during the tuning process, three conditions were considered: (1) The unit cells were tuned with one iteration under the presence of two neighbouring elements, (2) The unit cells were tuned with two iterations under the presence of two neighbouring elements, (3) The unit cells were tuned with one iteration under the presence of four neighbouring elements (Figure 3.46). During one iteration, the dimensions of the neighbouring elements were taken from the previous results. More specifically, in the first iteration, the dimensions of the neighbouring elements were taken from the tuning results where only the isolated unit cell was considered; in the second iteration, the dimensions of the neighbouring elements were taken from the results of the first iteration.

After the tuning process, the subarray is simulated in CST to get the results considering the mutual-coupling effect. Figures 3.45 and 3.47 show the comparisons of the subarray tuned with and without considering the neighbouring elements. As shown in Figure 3.45a, the average amount of beam squint of the SIW-slot subarray over the evaluated bandwidth is reduced by 1 degree after considering the neighbouring elements. After increasing the number of iterations or the number of present neighbouring elements, the amount of beam squint is not further improved. Figure 3.45b shows the comparison of the pattern distortion in terms of the RMS value. It can be seen that the improvement of the RMS value after considering the neighbouring elements is mainly around the center frequency, in the low-frequency region, the pattern distortion is even worse than in the case where only isolated unit cell is considered. At 26 GHz, the RMS value decreased by 5% when considering two neighbouring elements. After increasing the number of iterations to two while remaining the number of the present neighbouring elements, the RMS value is not further improved at 26 GHz. On the other hand, when considering four neighbouring elements during the tuning process, the RMS value at 26 GHz decreased by 5% compared to the case where only two neighbouring elements are considered. Compared with the results where no neighbouring element is considered, the average RMS value over the evaluated bandwidth is increased by 5% when two neighbouring elements are considered with 1-iteration. The increment of the average RMS value is due to the increment of the RMS value in the frequency range from 25 GHz to 25.6 GHz. When increasing the number of iterations to two, the average RMS value over the evaluated bandwidth is close to the results where no neighbouring element is considered (the difference is within 1%). What's more, when four neighbouring elements are considered during the tuning process, the RMS value over the evaluated bandwidth is decreased by 2% compared to the case when no neighbouring element is considered. Figure 3.47 shows the comparison of the S-parameters, compared with the result when no neighbouring element is considered, it is observed that the bandwidth of the subarray increased by 200 MHz when four neighbouring elements are considered during the tuning process. In the case when only two neighbouring elements are considered, there is no improvement in terms of the S-parameter.

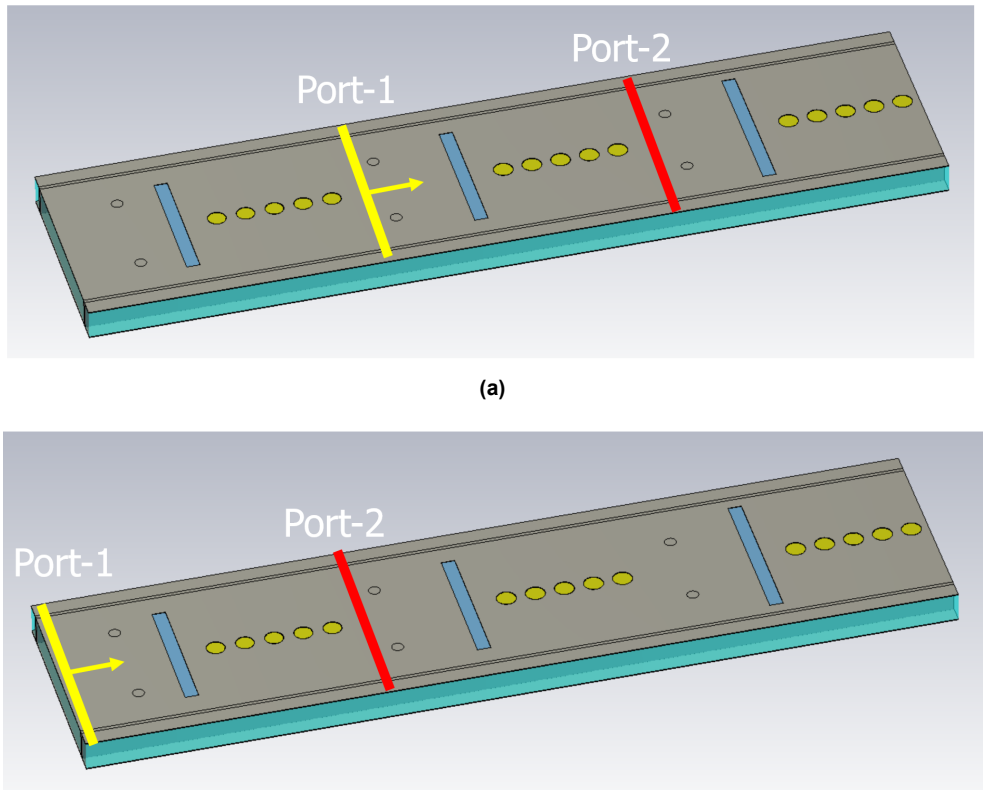

Figure 3.44: Unit cell tuning set-up with the presence of two neighbouring elements: (a) tuning the middle element, (b) tuning the side element.

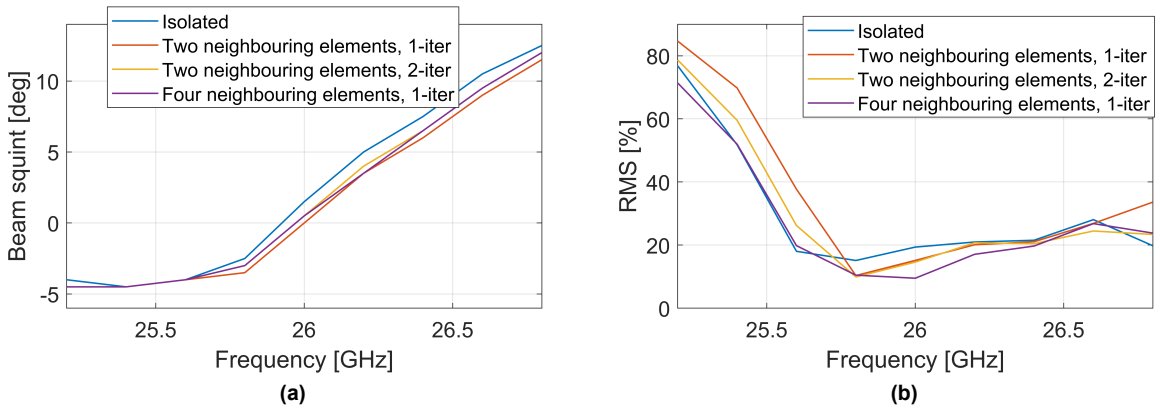

Figure 3.45: SIW-slot subarray performance analysis (tuning with the presence of neighbouring elements): (a) beam squint, (b) pattern distortion.

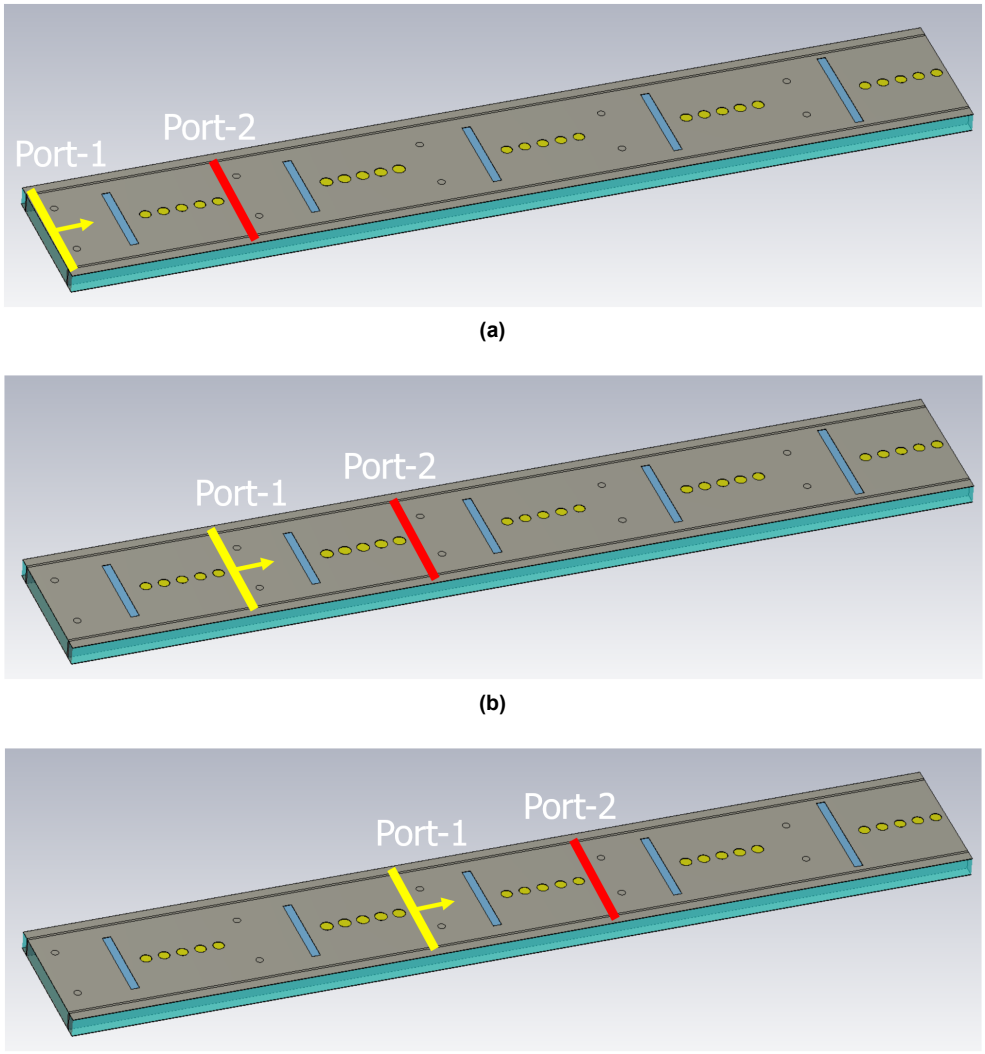

Figure 3.46: Unit cell tuning set-up with the presence of four neighbouring elements: (a) tuning the side element case-1, (b) tuning the side element case-2 (c) tuning the middle element.

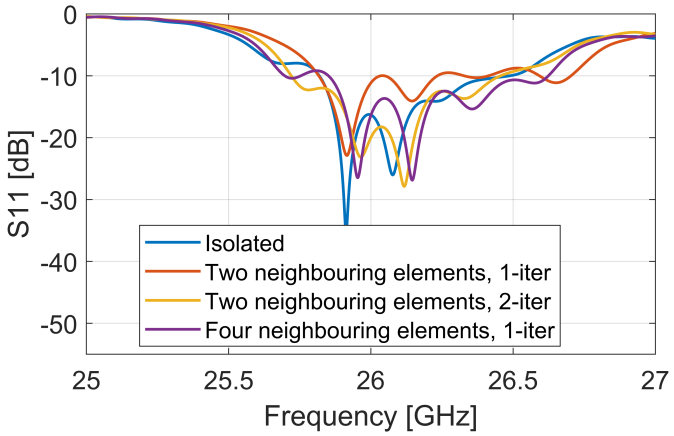

Figure 3.47: S-parameters of the SIW-slot subarrays tuned under the presence of the neighbouring elements

3.6. Conclusion - edge-fed subarrays

In conclusion, for edge-fed subarray, the beam squint cannot be completely eliminated for all seven unit cell structures, as well as for the pattern distortion. However, among all seven unit cell structures, the microstrip-slot-patch unit cell shows the least amount of beam squint in subarray patterns, which is from $-5°$ to $2°$ within the $\pm 800MHz$ frequency range. In order to further minimize the beam squint, the centre-fed subarray structure will be investigated in the next chapter. For the pattern distortion, the proximity-coupled subarray shows the most steady radiation pattern which is consistent with the previous result where the mutual coupling effect is neglected. However, the beam squint in proximity-coupled subarray is quite significant, which is about $-11°$ to $7.5°$ within the $\pm 800MHz$ frequency range. Thus, it is worth investigating the application of the centre-fed structure in proximity-coupled subarray to see if the beam squint can be further reduced while making the pattern shape stable. In addition, among all subarrays, the SICL-slot-patch subarray shows the largest impedance bandwidth which is about 1.9 GHz, while the smallest bandwidth appears on the SIW-slot subarray which is about 500 MHz. As a result, the realized gain of the SIW-slot subarray varied from -0.95 dBi to 15.46 dBi within the evaluated bandwidth. The most stable realized gain appears on the proximity-coupled subarray with less than 1.5 dB variation within the evaluated bandwidth. Moreover, the beam squint and pattern distortion in edge-fed subarray can be reduced by considering the neighbouring elements during the tuning process of the unit cells. Increasing the number of neighbouring elements is more effective than increasing the number of iterations. However, the amount of improvement is quite limited. Compared with the results when no neighbouring element is considered, the average amount of beam squint over the evaluated bandwidth decreased only by 1 degree. On the other hand, the RMS value at the center frequency is decreased by 5% when considering two neighbouring elements and is decreased by 10% when considering four neighbouring elements.

4

Centre-fed subarray design

This chapter centers on investigating the performance of the center-fed array. In chapter 3, the edge-fed proximity-coupled subarray was proved to have the most frequency-stable radiation pattern (15.7% RMS value on average) but with a quite significant beam squint ($\pm 10°$) within the evaluated bandwidth. To reduce the amount of beam squint, the center-fed proximity-coupled subarray is designed in this chapter. First, the pattern generated from MATLAB for the center-fed configuration will be discussed. Then, the design of the center-fed proximity-coupled unit cell and the center-fed coax-to-microstrip-line feeding structure will be introduced. Finally, the performance of the center-fed proximity-coupled subarray will be compared with the edge-fed proximity-coupled subarray in terms of the beam squint and pattern distortion.

4.1. csc^2 pattern shaping via element excitation control (center-fed)

The generation of the csc^2 radiation pattern for the center-fed configuration is again using the same code as in section 3.1. In center-fed configuration, an extra spacing of 3mm in the middle of the subarray, which is allocated for the feeding structure, is considered in the MATLAB algorithm. Figure 4.1 shows the array factor pattern and the corresponding amplitude and phase distribution in center-fed configuration. Compared with the amplitude distribution in edge-fed configuration, having a larger amplitude in the middle region is required in center-fed configuration which makes the pattern matching more challenging and pattern errors with respect to the mask increased.

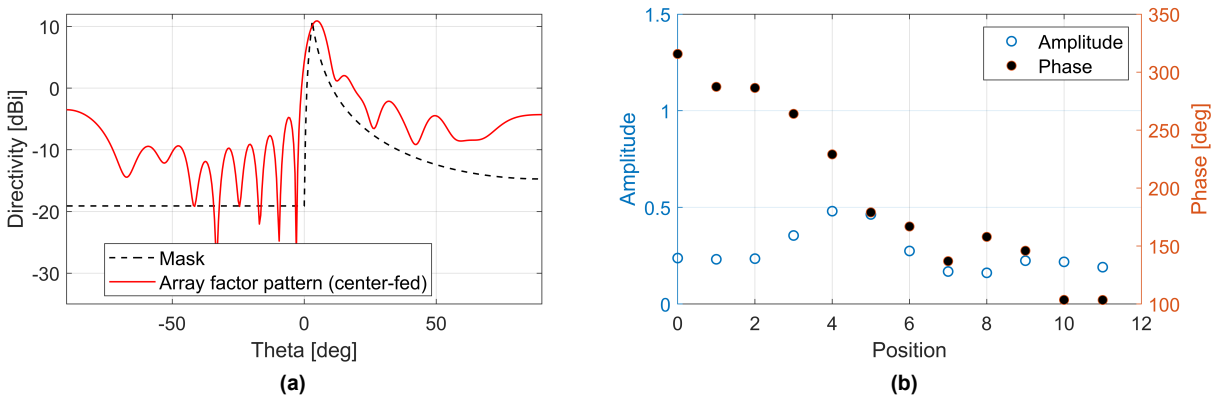

Figure 4.1: csc^2 pattern generation (center-fed): (a) Array factor pattern, (b) amplitude and phase distribution.

4.2. Center-fed proximity-coupled subarray design

In series-fed antenna arrays, center-fed configuration has a quasi-symmetrical structure and halved long-line effect compared to edge-fed configuration, making it ideal for overcoming the beam squint issues [43], [46]. The design of the center-fed proximity-coupled subarray starts from the re-configuration of the unit cell

structure in order to make the subarray symmetric. The structure of the center-fed proximity-coupled unit cell is shown in Figure 4.2. The comparison between the simulation models of the edge-fed and center-fed proximity-coupled csc^2 arrays are shown in Figure 4.3, where 50Ω transmission lines are used. In the center-fed configuration, both ports are simultaneously excited and a 180-degree phase shift is added to the left part of the array due to the mirroring of the structure. Compared with the edge-fed subarray structure where the 12th element functions as a matched load, in center-fed subarray structure, the 1st element and the 12th element both function as the matched load.

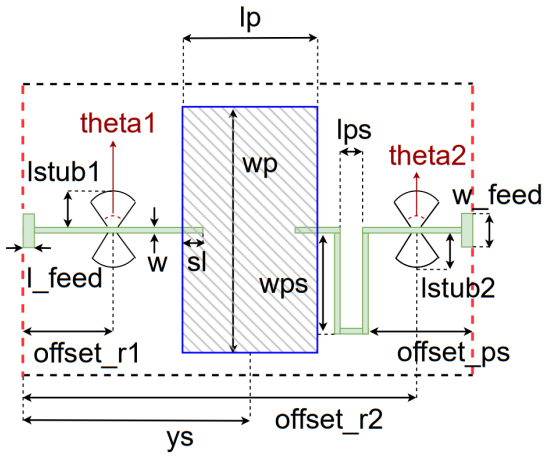

Figure 4.2: Center-fed proximity-coupled unit cell: dimensions

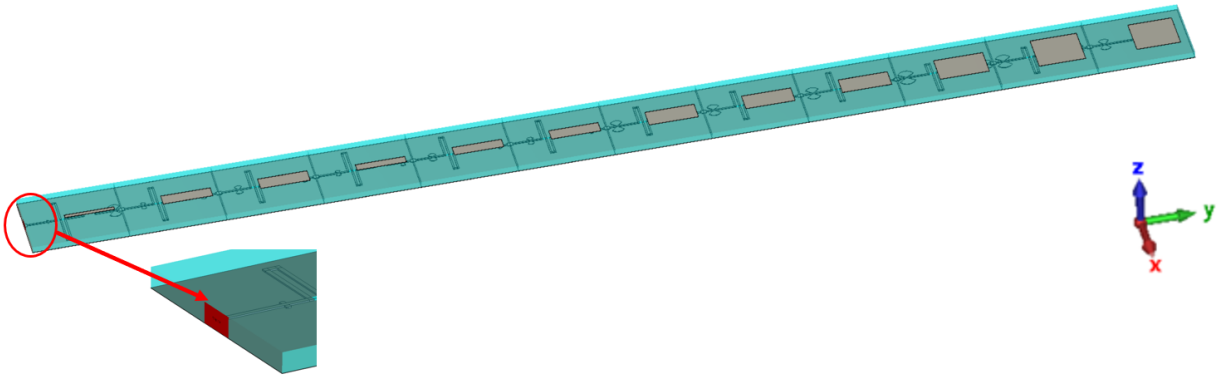

(a)

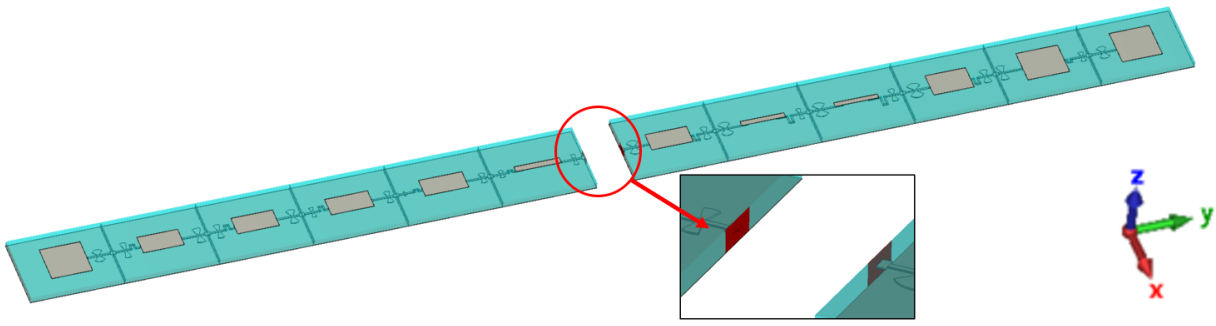

(b)

Figure 4.3: Feeding strategies in a proximity-coupled csc^2 array model: (a) edge-fed, (b) center-fed

In order to obtain a better impedance matching in the center-fed proximity-coupled subarray, a coax-to-microstrip-line feeding structure is designed. The CST model and the detailed structure of the designed coax-to-microstrip-line feeding structure are shown in Figures 4.4 and 4.5 respectively. The turns in the microstrip line and the offset of the coax feeding position create the desired phase shift between the left and the right part of the subarray. The ring slot placed in between the coax and the substrate controls the impedance transition from the coax to the microstrip line.

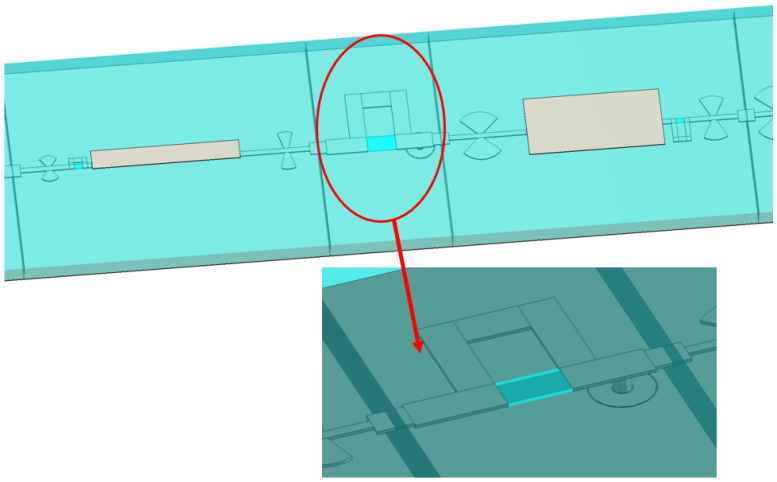

Figure 4.4: Coax-to-microstrip-line feeding

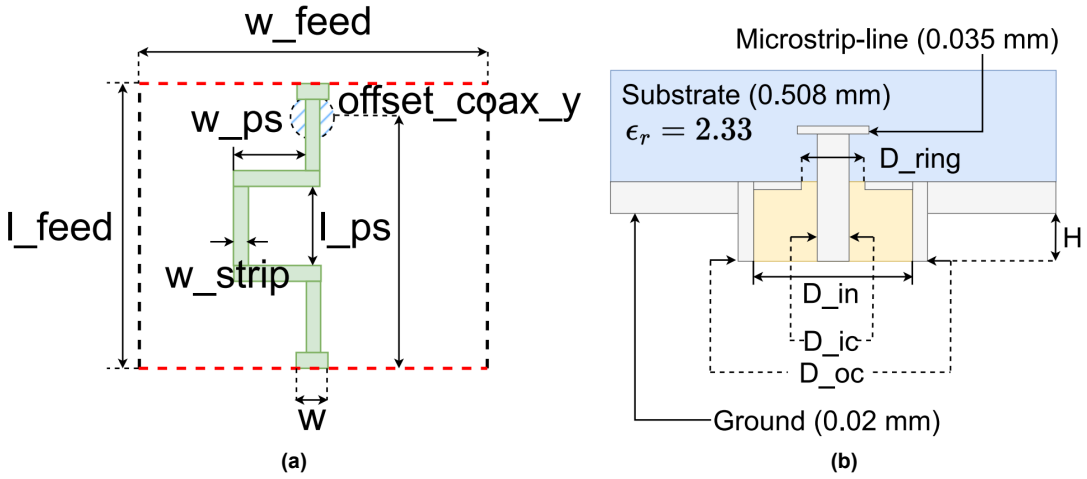

Figure 4.5: Coax-to-microstrip-line feeding structure: (a) top view, (b) side view

The tuning process of each unit cell in the center-fed proximity-coupled subarray follows exactly the same process as the edge-fed proximity-coupled subarray. Each unit cell was tuned in CST to realise the desired amplitude and phase distribution shown in Figure 4.1b. Figures 4.6 and 4.7 show the tuning result of the center-fed proximity-coupled subarray. Table 4.1 shows the optimized dimensions of each center-fed proximity-coupled unit cell.

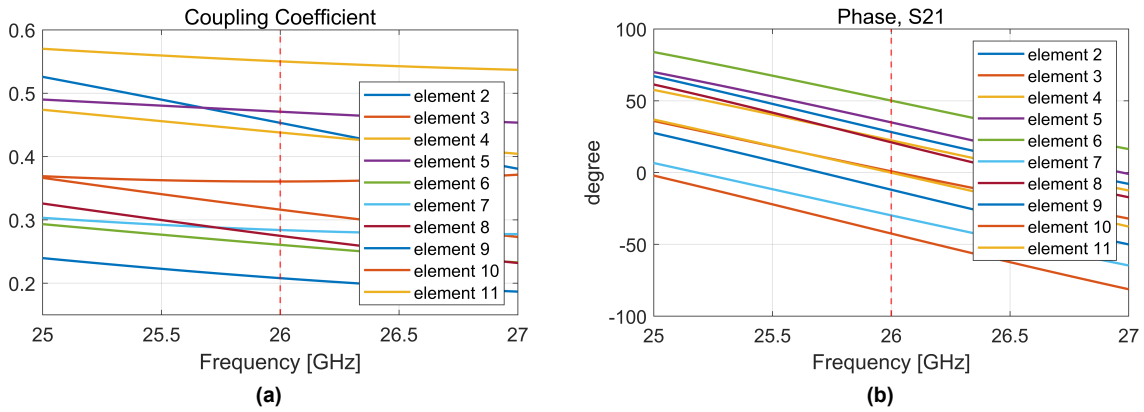

Figure 4.6: Center-fed Proximity-Coupled unit cell tuning result: (a) coupling coefficient, (b) phase.

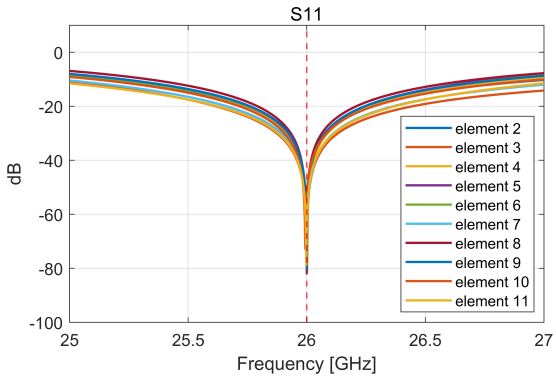

Figure 4.7: Center-fed Proximity-Coupled unit cell tuning result: S11

Table 4.1: Proximity-Coupled unit cell tuning result for center-fed configuration: optimized dimensions (in mm and deg)

No.	sl	wp	lp	wps	lstub1	lstub2	offset_r1	offset_r2	theta1	theta2
1	1.03	2.91	3.22	\	0.53	\	1.08	\	47.58	\
2	0.53	0.17	3.23	0.26	0.65	0.67	0.62	6.41	30.51	21.21
3	0.73	1.57	3.30	0.30	0.61	0.59	0.69	6.52	35.19	23.60
4	0.65	1.57	3.41	0.26	0.50	0.42	0.54	6.56	29.84	23.76
5	0.66	1.57	3.46	0.05	0.42	0.15	0.52	6.73	38.67	20.02
6	0.68	0.49	3.61	0.05	0.46	0.30	0.71	6.52	22.62	44.97
7	0.94	1.55	3.31	0.40	0.60	0.52	0.91	6.61	49.44	31.78
8	0.61	0.41	3.50	0.54	0.70	0.46	0.74	6.69	52.90	23.51
9	0.75	0.38	3.49	0.62	0.62	0.53	0.83	6.66	51.28	29.18
10	0.92	1.97	3.25	0.44	0.65	0.58	0.96	6.60	52.23	34.15
11	0.63	2.71	3.35	0.15	0.64	0.42	0.48	6.88	31.00	33.63
12	1.05	2.93	3.22	\	0.53	\	1.08	\	47.78	\

4.3. Center-fed proximity-coupled subarray pattern analysis

In this section, the radiation pattern of the center-fed proximity-coupled subarray will be analyzed in terms of the beam squint and pattern distortion. First, the subarray will be analyzed without considering the mutual-coupled effect. By doing so, the effect of the excitation amplitude and phase on the radiation pattern shaping can be investigated. Then, the subarray will be simulated in CST to include the mutual-coupling effect. The center-fed and the edge-fed proximity-coupled subarray will then be compared in terms of their performance on beam squint and pattern distortion.

4.3.1. Pattern analysis without mutual-coupling effect

Figure 4.8 shows the amount of beam squint and pattern distortion of the center-fed proximity-coupled subarray compared with its edge-fed configuration without considering the mutual coupling effect. It can be seen that the amount of beam squint reduced significantly from 25.6 GHz to 26.8 GHz. Compared with the edge-fed configuration, the RMS value of the center-fed subarray remains almost unchanged at the center frequency (26 GHz), but around other evaluated frequencies, the RMS value increased by 29% at 25.6 GHz and 10% at 25.8 GHz. The average RMS value of the center-fed subarray over the evaluated bandwidth increased by 14% compared to the edge-fed configuration.

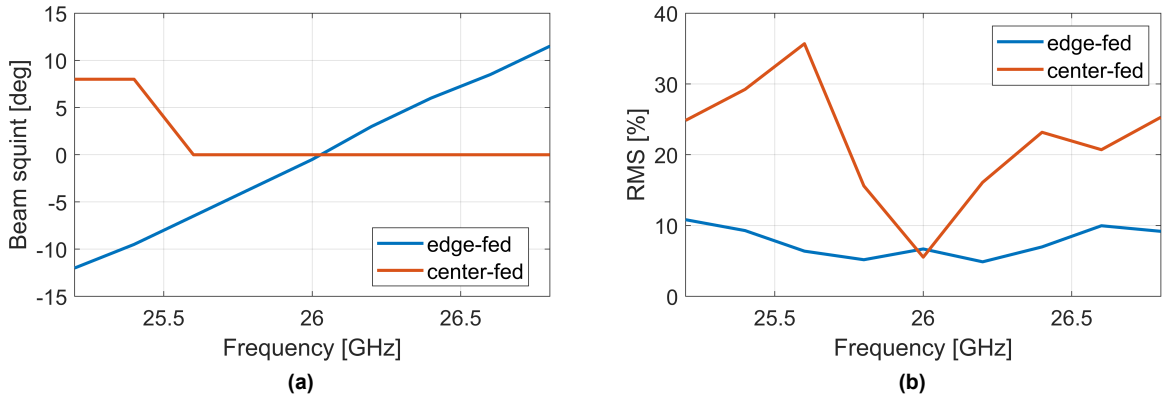

Figure 4.8: Center-fed vs edge-fed proximity-coupled subarray (no MC): (a) beam squint, (b) pattern distortion.

Figures 4.9 and 4.10 show the radiation patterns of the center-fed proximity-coupled subarray with the corresponding excitation amplitude and phase, respectively. The excitation amplitude at 25.2 GHz and at 26.8 GHz, although numerically different from the desired distribution, follow the same general trend. However, upon comparing the excitation phase with the desired phase distribution, it was observed that the tuned phase shift increased from elements 6 to 12 at 25.2 GHz, which contradicts the desired phase distribution's decreasing trend. Similarly, at 26.8 GHz, elements 1 to 6 exhibit an opposite trend in the tuned phase distribution as compared to the desired phase distribution. Due to the difference between the desired and the tuned excitation amplitude and phase distribution, the radiation patterns at the evaluated frequencies are distorted compared to the synthesized pattern. On the other hand, similar absolute values of the slope between the desired and the tuned phase distribution leads to a steady main-lobe direction.

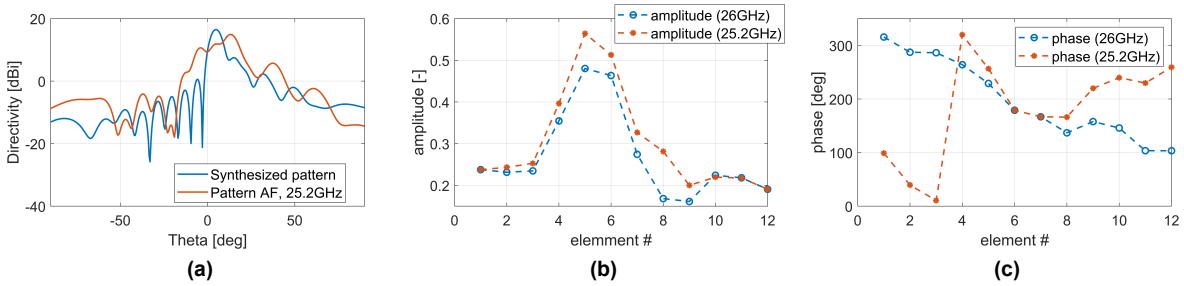

Figure 4.9: Subarray pattern analysis for center-fed proximity-coupled subarray at 25.2 GHz: (a) radiation pattern, (b) excitation amplitude, (c) phase shift.

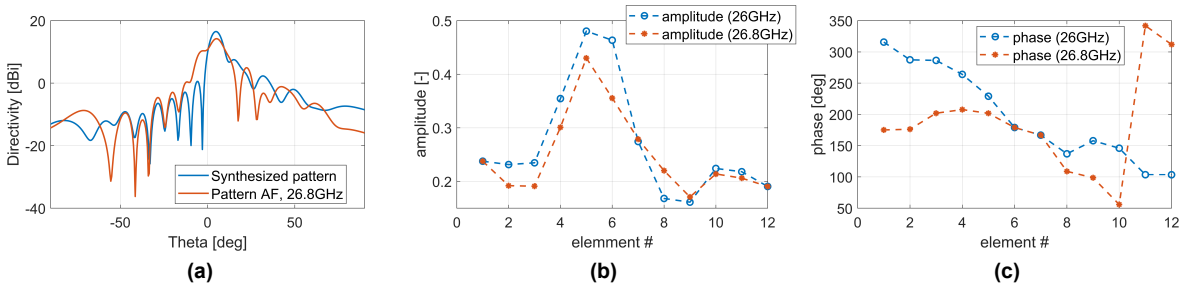

Figure 4.10: Subarray pattern analysis for center-fed proximity-coupled subarray at 26.8 GHz: (a) radiation pattern, (b) excitation amplitude, (c) phase shift.

To further investigate the influence of the excitation phase and amplitude on the pattern distortion, comparisons are made under three situations: (a) the radiation pattern is calculated with amplitude and phase distribution at the excitation frequency, (b) the radiation pattern is calculated with amplitude distribution at 26 GHz and phase distribution at the excitation frequency, (c) the radiation pattern is calculated with phase distribution at 26 GHz and amplitude distribution at the excitation frequency. Figures 4.11 and 4.12 show the comparisons at 25.2 GHz and 26.8 GHz, respectively. It can be seen that when the radiation pattern is calculated using the amplitude distribution at 26 GHz, the pattern is still highly distorted compared to the synthesized pattern. However, when the pattern is calculated using the phase distribution at 26 GHz, the distortion is reduced significantly under both excitation frequencies. The above results show that the pattern distortion in center-fed proximity-coupled subarray is mainly caused by the difference between the phase distribution at 26 GHz center frequency and the phase distribution at the actual excitation frequency when neglecting the effect of mutual-coupling.

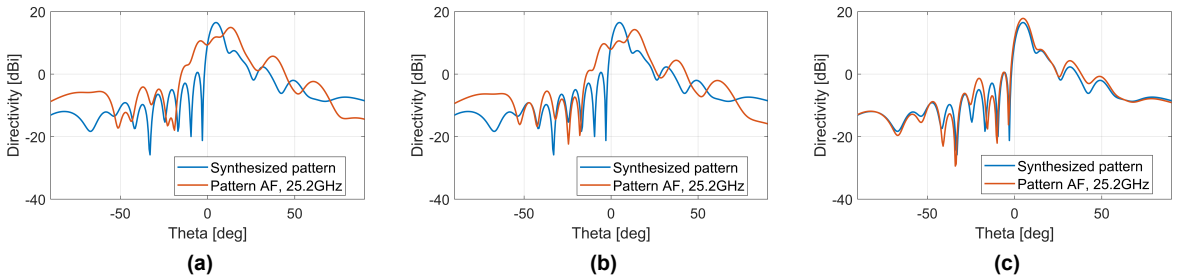

Figure 4.11: Subarray pattern analysis for center-fed proximity-coupled subarray at 25.2 GHz: (a) radiation pattern, (b) radiation pattern with amplitude distribution at 26 GHz, (c) radiation pattern with phase distribution at 26 GHz.

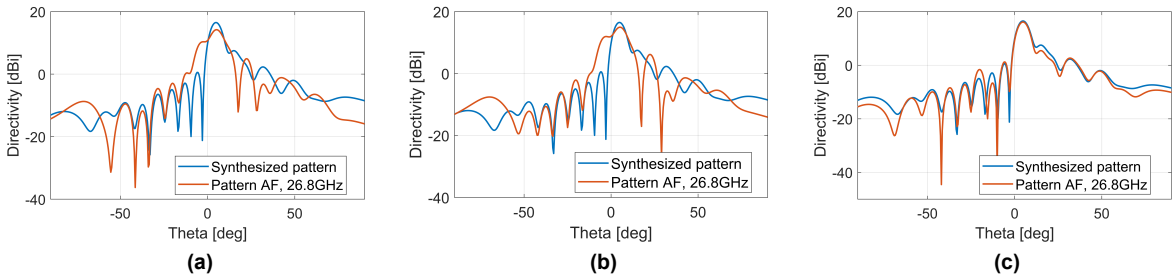

Figure 4.12: Subarray pattern analysis for center-fed proximity-coupled subarray at 26.8 GHz: (a) radiation pattern, (b) radiation pattern with amplitude distribution at 26 GHz, (c) radiation pattern with phase distribution at 26 GHz.

4.3.2. Pattern analysis with mutual-coupling effect

To include the mutual coupling effect, the center-fed proximity-coupled subarray was modeled and simulated in CST. Before the simulation, an additional tuning process has been done to the dimensions of each unit cell to reach the desired amplitude and phase distribution with the presence of other unit cells in the subarray. By doing so, the influence of the mutual coupling to the pattern shape can be further reduced. Figure 4.13 shows the comparison between the edge-fed and the center-fed proximity-coupled subarray in terms of the beam squint and pattern distortion with the presence of the mutual-coupled effect. It can be seen that the center-fed configuration significantly reduces beam squint to within 1.5° between 25.6-26.8 GHz. However, the RMS error is within 20% only between 25.8-26.5 GHz in the center-fed array and the average RMS value increased for about 6.2% compared with the edge-fed configuration. Compared with the situation without mutual coupling effect, the amount of beam squint on the center-fed subarray does not change too much (within $\pm 1°$), while the average increment of the RMS value is around 4%. Figure 4.14 shows the radiation patterns and reflection coefficient (S11) of the designed center-fed proximity-coupled array. The reflection coefficient of the center-fed proximity-coupled subarray shows good matching (S11 below -10 dB) from 25 GHz to 26.6 GHz. The polarization level of the center-fed proximity-coupled subarray is controlled by limiting the length of the phase shifter. Figure 4.15 shows the polarization level of the center-fed proximity-coupled subarray in the U-V plane, it can be seen that the cross-polarization level is 21.8 dB lower than the co-polarization level.

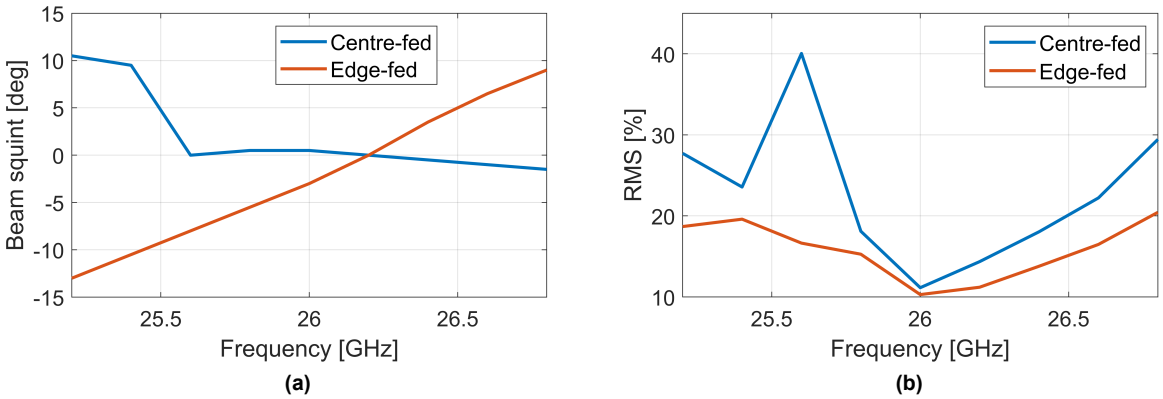

Figure 4.13: Center-fed vs edge-fed proximity-coupled array: (a) beam squint, (b) pattern distortion

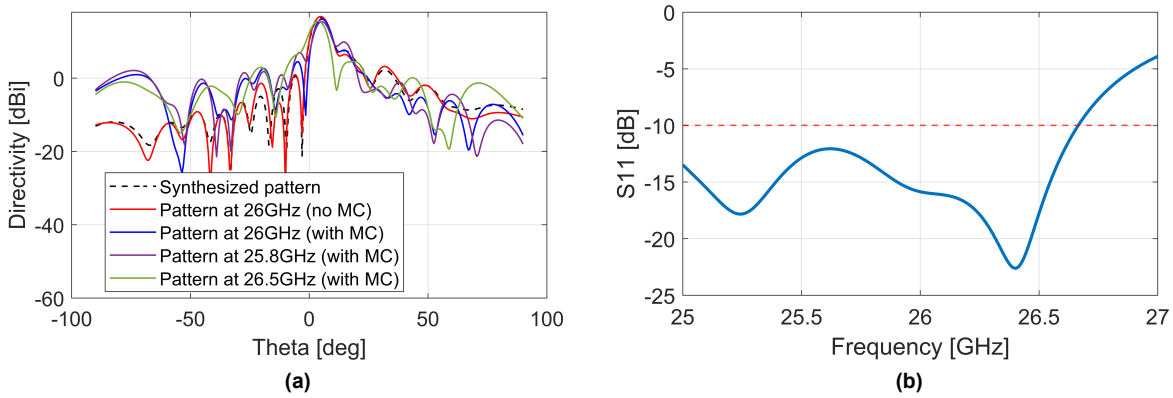

Figure 4.14: Center-fed proximity-coupled array performance: (a) radiation patterns, (b) reflection coefficient

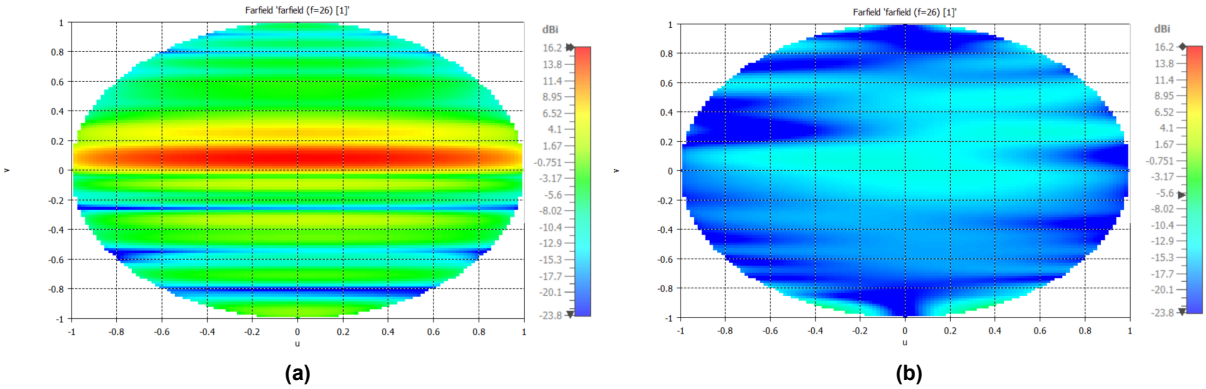

Figure 4.15: Polarization level of the center-fed proximity-coupled subarray at 26 GHz: (a) co-pol, (b) x-pol

4.4. Conclusion - center-fed array

From the simulation results of the center-fed proximity-coupled subarray, it is shown that by using the center-fed structure, the beam squint of the series-fed array can be significantly reduced. Compared to the edge-fed subarray, the center-fed subarray suffers more from pattern distortion. This is because the actual phase distribution at the excitation frequency on the left and the right part of the center-fed subarray show an opposite slope compared to the phase distribution at 26 GHz center frequency. The above results show that there is a trade-off between beam squint reduction and pattern distortion reduction.

5

Array of subarrays

In this chapter, the center-fed proximity-coupled subarray which is investigated in Chapter 4 will be analyzed in the array of subarrays. First, a comparison will be made between the center-fed proximity-coupled subarray and the center-fed proximity-coupled phased array of 12 subarrays. Then, the performance of the array using lossless material and using lossy material will be compared in terms of the reflection coefficient, realized gain, scanning ability, port-to-port coupling and cross-polarization level. Besides, a design of the array with fins structure has been done aiming to improve the thermal performance of the array and can be found in Appendix A.

5.1. Comparison between the subarray and the array of subarrays

Figure 5.1 shows the CST model of the center-fed proximity-coupled array. The model was created by directly transforming and copying the model of the center-fed proximity-coupled subarray with half-wavelength spacing.

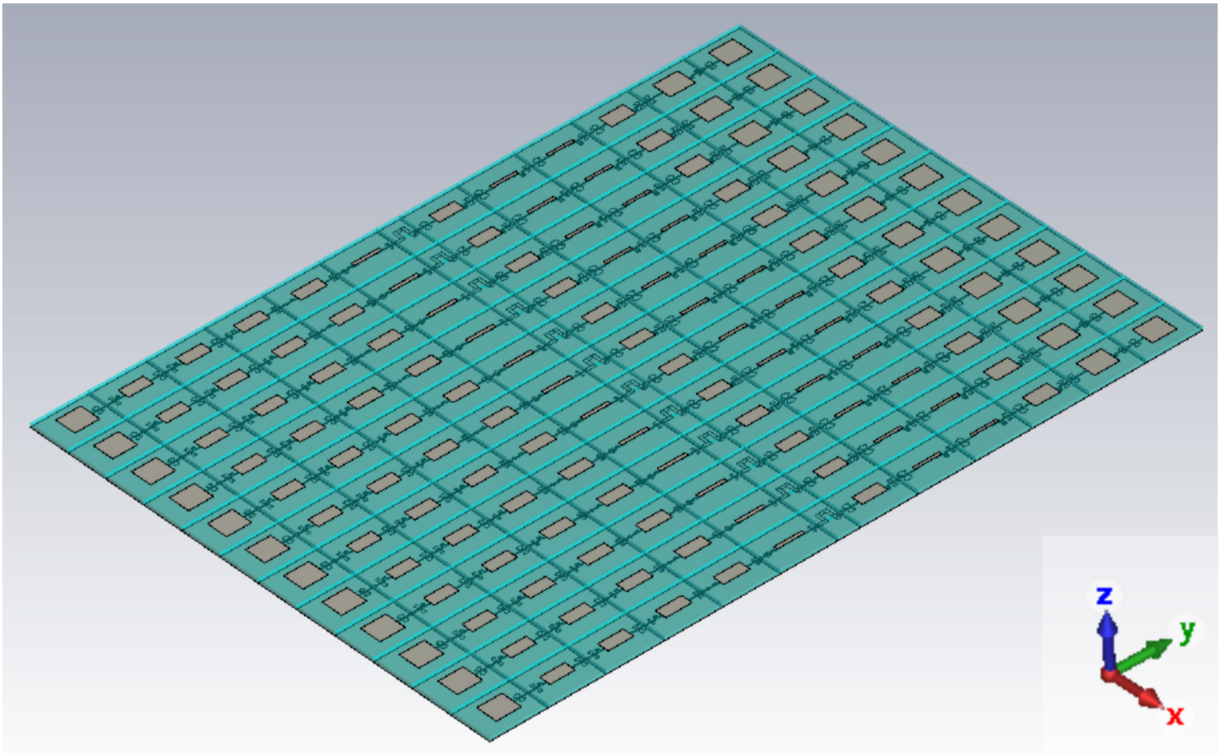

Figure 5.1: Center-fed proximity-coupled array: CST model

Figures 5.2 show comparisons of the radiation patterns and the reflection coefficient between the 1x12

subarray and the array of subarrays. After extending the subarray to the array, the maximum directivity increased from 16 dBi to 26 dBi. From Figure 5.2b, it can be seen that the matching becomes better around 26.4 GHz after extending the subarray to the array, and the bandwidth remains almost unchanged. In addition, the reflection coefficients from the center subarray (S66) and the edge subarray (S11) in the array behave similarly to each other, indicating that the mutual coupling between subarrays does not bring too much influence to the matching condition.

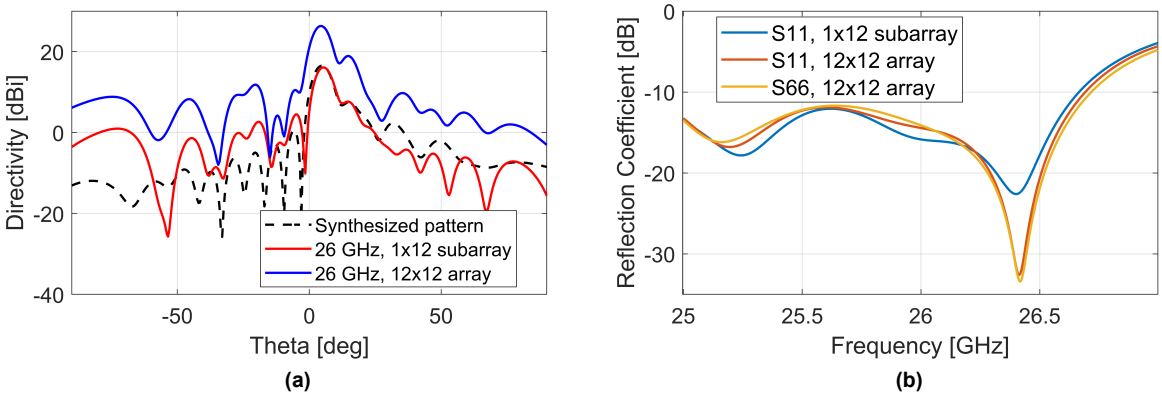

Figure 5.2: Radiation pattern comparison at 26GHz: (a) Radiation patterns, (b) Reflection coefficient

Figures 5.3 show the comparisons of the beam squint and pattern distortion between the 1x12 subarray and the array of subarrays. Again, the calculation of the RMS value of the array of subarrays is based on the synthesized pattern as shown in Figure 5.2a which is obtained by scaling the mask with the isolated proximity-coupled unit cell pattern. From Figure 5.3a, it can be seen that the beam squint of the array has an overall offset of about 0.5 degrees compared to the 1x12 subarray, while the amount of beam squint from 25.6 GHz to 26.8 GHz remains unchanged. The RMS value of the array, as shown in Figure 5.3b, increased by 8% on average between 25.6 GHz and 26 GHz, while the RMS value at 25.2 GHz drops for about 4%. The average RMS value of the array over the evaluated frequency band increased by 2% compared to the subarray. The difference between the RMS value of the 1x12 subarray and the array is probably due to the increment of the mutual coupling after extending the subarray to an array. Within the frequency from 25.8 GHz to 26.5 GHz, the beam squint is still controlled within 1 deg and the average amount of pattern distortion is controlled below 20%.

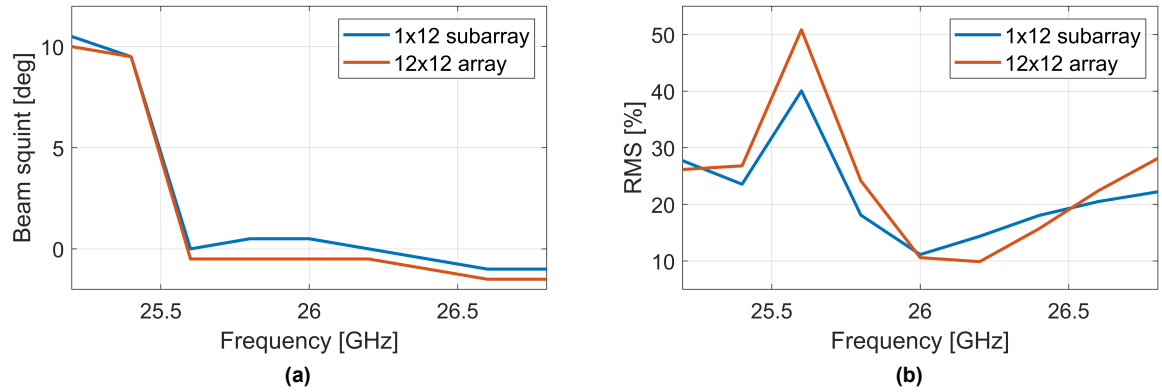

Figure 5.3: Pattern analysis between the 1x12 subarray and the array of subarrays: (a) Beam squint, (b) Pattern distortion

5.2. Array of subarrays analysis with lossy material

In this section, the simulation of the array of subarrays will be done with lossy material. More specifically, the PEC was replaced by copper (pure) and the substrate material Arlon CuClad 233 (lossless) was replaced by the Arlon CuClad 233 (lossy). Figure 5.4 shows the simulation results between the array using lossless materials and the array using lossy materials in terms of the radiation pattern and the reflection coefficient. From Figure 5.4a, it can be seen that the pattern shape remains unchanged after using the lossy materials, while the maximum gain drops about 0.6 dBi. On the other hand, Figure 5.4b shows the reflection coefficient of the edge element (S11) and the center element (S66), it is observed that the -10 dB bandwidth remains the same when changing the materials to the lossy ones, and the main difference is the matching around the resonant frequency. After changing the material to the lossy ones, the matching around the resonant frequency becomes deeper for the edge element which is from -32.3 dB to -45 dB. And for the center element, the matching around the resonant frequency becomes worse which is from -33.4 dB to -26.8 dB.

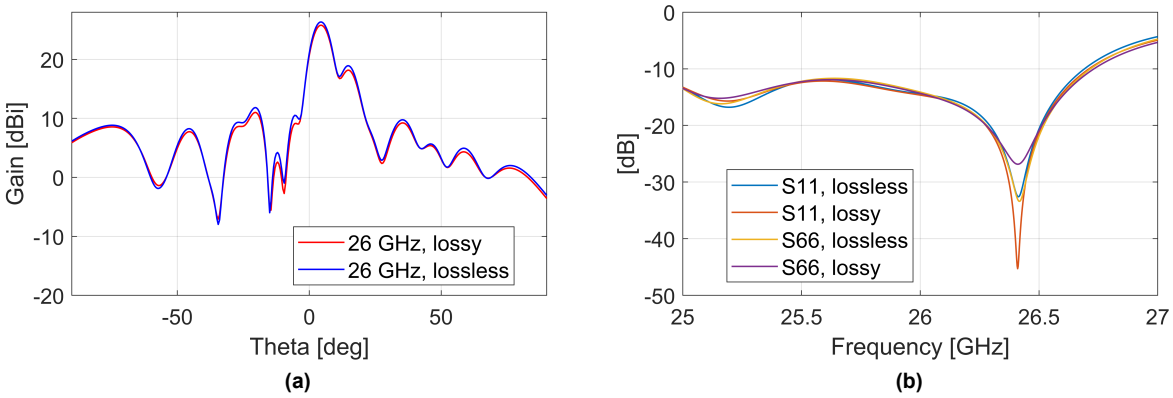

Figure 5.4: Radiation pattern comparison at 26GHz: (a) Radiation patterns, (b) Reflection coefficient

Figure 5.5a shows the port-to-port coupling of the array with the lossy materials, where S21 represents the coupling between the edge elements and S76 represents the coupling between the center elements. It can be seen that both S21 and S76 are below -20 dB within the evaluated bandwidth, meaning that the port-to-port coupling is well controlled. Figure 5.5b shows the maximum realized gain under the corresponding excitation frequency. It is observed that the drop of the maximum is controlled within -3 dB from 25 GHz to 26.8 GHz, which is well-matched to the -10 dB bandwidth as shown in Figure 5.4b.

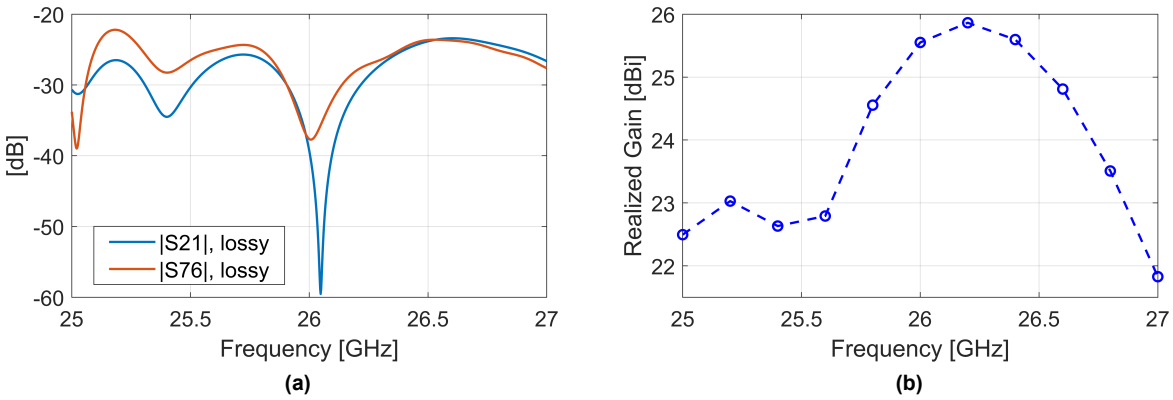

Figure 5.5: Lossy array simulation results: (a) port-to-port coupling, (b) realized gain

The scanning ability of the phased array in the azimuth plane is investigated by setting appropriate

phase shift between subarrays. Figures 5.6, 5.7 and 5.8 show the radiation patterns in the U-V plane scanning at 0 deg, 30 deg and 60 deg. It can be seen from the co-pol plots that the total amount of gain drop is within 3 dB when scanning from 0 deg to 60 deg. On the other hand, the cross-pol level is always below -20 dB relative to the co-pol level during the scanning.

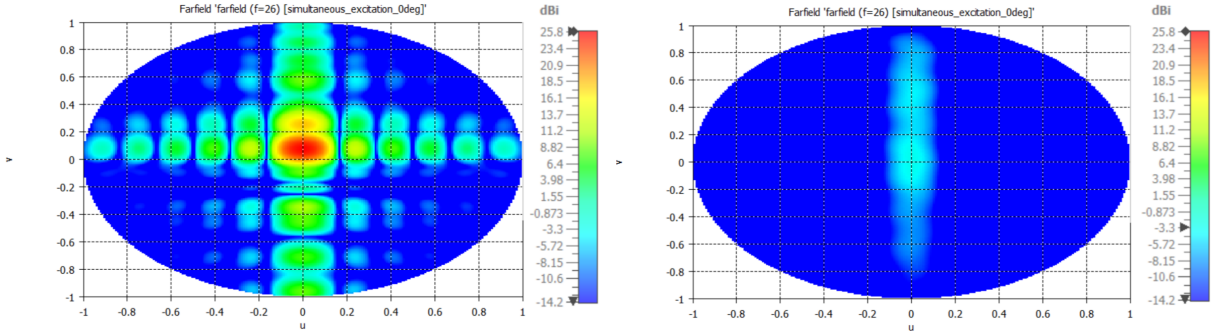

(a) **(b)**

Figure 5.6: Lossy array pattern at 26 GHz, scanning at 0 deg: (a) co-pol, (b) x-pol

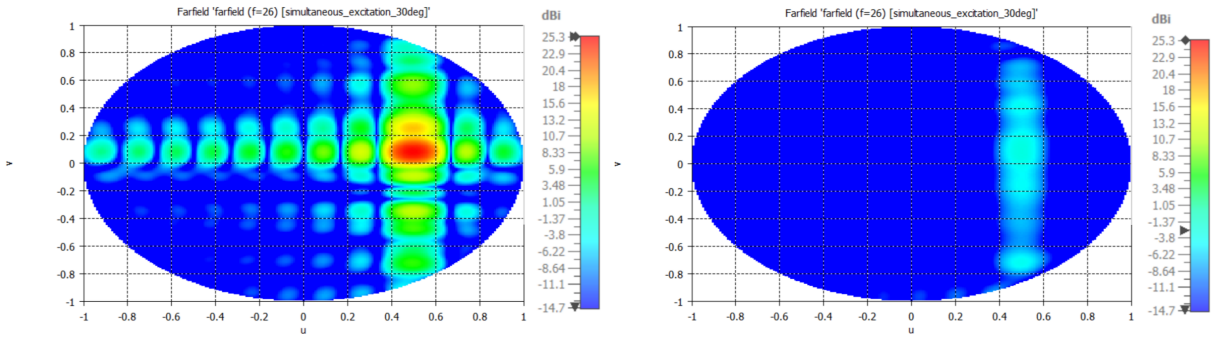

(a) **(b)**

Figure 5.7: Lossy array pattern at 26 GHz, scanning at 30 deg: (a) co-pol, (b) x-pol

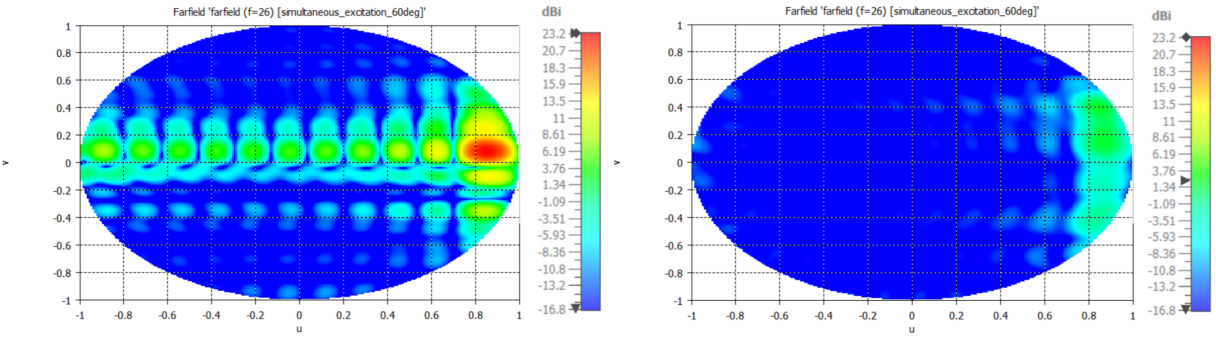

(a) **(b)**

Figure 5.8: Lossy array pattern at 26 GHz, scanning at 60 deg: (a) co-pol, (b) x-pol

5.3. Conclusion on the array of subarrays

The performance of the array of proximity-coupled subarrays is discussed in this chapter. Results show that the array still has the ability to reduce the beam squint but with an overall offset compared with the subarray. Due to the increment of the mutual coupling when extending the subarray to the array, the RMS value of the array increased by 8% between 25.6 GHz and 26 GHz. On the other hand, the average RMS value of the array over the evaluated frequency band increased only by 2% compared to the subarray. After applying the lossy material, the results show that the array has a -20 dB port-port coupling, the drop of the realized gain is below 3 dB within the -10 dB bandwidth, the scanning loss from 0 deg to 60 deg is within -3 dB and the cross-polarization level is controlled below -20 dB. Based on the above results, the array of proximity-coupled subarrays shows promising performance and is able to reduce the beam squint while having a reasonable pattern distortion (around 20% difference compared to the synthesized pattern) within the frequency range from 25.8 GHz to 26.5 GHz.

6

Conclusions and recommendations

This chapter illustrates the conclusions of the thesis in terms of its novel contributions to the existing literature and the major conclusions. Following this, the recommendations will be provided for the future investigation.

6.1. Conclusions

6.1.1. Relevance and novel contributions

In order to reduce the power consumption, heat generation and complexity of the antenna array used in the mm-wave base stations for 5G and beyond, the MS3 team at TU Delft has proposed implementing hybrid beam-forming by using an array of series-fed analog subarrays which can (ideally) radiate frequency-stable shaped beam patterns (csc2) in the elevation plane. However, the existing structures of series-fed subarrays suffer from significant beam squint and pattern distortion which limits the radiation bandwidth of the antenna.

To address this problem at low-complexity, this thesis proposes two innovative ideas, one at element-design level and one at array-design level. At the element-design level, the novel approach is to design a unit cell (feeding + radiating component) for the realization of the most frequency-stable amplitude-phase coefficients. At the array-design level, feeding the array from the center is proposed for the first time for an asymmetrically-shaped pattern synthesis.

In details, this thesis makes four main novel contributions:

1. A novel center-fed proximity-coupled patch-based subarray and its phased array are proposed with the best performance reported so far. The designed subarray centered at 26 GHz is able to radiate csc^2 shaped beam pattern with $\pm 1°$ beam squint within the frequency band from 25.6 GHz to 26.8GHz. The pattern distortion is controlled within 20% in terms of the RMS value from 25.8 GHz to 26.5 GHz. The reflection coefficient is below -10 dB from 25 GHz to 26.6 GHz. The phased array of 12 subarrays is able to scan from 0° to 60° in the azimuth plane with a gain drop within 3 dB and the cross-polarization level is 20 dB lower than the co-polarization level.
2. The performance comparison of seven types of unit cells in terms of beam squint and pattern distortion in (asymmetrically) shaped beam series-fed edge-fed subarrays under the conditions both with and without mutual coupling. Re-design of the best-performing unit cell.
3. Introduction of Root-Mean-Square error in synthesized patterns of the series-fed antennas as the performance metric.
4. Study on the impact of mutual coupling on beam squint and pattern distortion of the edge-fed and center-fed subarrays.

The novel results achieved resulted in the preparation and submission of two conference papers. One of them entitled ”Cosecant-Squared Pattern Stability With Frequency in Series-Fed Antennas at mm-Waves” has been written and will be submitted to CAMA 2023, and the other which is about the cosecant-squared shaped pattern seires-fed antennas design in mm-wave with heatsink structure will be prepared and submitted to EuCAP 2024.

6.1.2. Major conclusions

The major conclusions of the thesis are:

1. When mutual coupling is ignored, the amount of beam squint in series-fed subarrays is mainly due to the difference in the absolute slope between the phase distribution along the subarray at the center frequency and phase distribution along the subarray at the actual excitation frequency. When the absolute slope of the phase distribution along the subarray increases, the main-lobe direction will be squinted to the right. When the absolute slope of the phase distribution along the subarray decreases, the main-lobe direction will be squinted to the left. On the other hand, the pattern distortion under no mutual coupling is influenced by both amplitude and phase distribution.
2. The mutual coupling effect in series-fed subarrays can increase the pattern distortion. In edge-fed series-fed subarrays, the average RMS value increased by 13% on average over the evaluated frequency band after considering the mutual coupling. While in the center-fed proximity-coupled subarray, the RMS value at 26 GHz increased from 5.5% to 11% after considering the mutual coupling, while the average RMS over the evaluated frequency band stays almost the same which is around 21.8% both with and without mutual coupling. On the other hand, the amount of beam squint is less affected by the mutual coupling effect. For both edge-fed and center-fed subarrays, the difference in the average beam squint of a subarray over the evaluated bandwidth is within 1° with and without considering mutual coupling.
3. By using the center-fed configuration based on the proximity-coupled subarray, the amount of beam squint can be significantly reduced compared to the edge-fed configuration. The amount of beam squint on the center-fed subarray has been controlled within $\pm 1°$ within the frequency band from 25.6 GHz to 26.8 GHz, while in the edge-fed configuration, the amount of beam squint is 17° within the same frequency band.
4. Compared to edge-fed series-fed subarray, the center-fed series-fed subarray suffers more from pattern distortion based on the corresponding synthesized pattern. Based on the analysis of the proximity-coupled subarray, the average RMS value of the center-fed proximity-coupled subarray over the evaluated bandwidth increased by 14% and 6.2% without and with mutual coupling effect respectively compared to the edge-fed configuration. The main reason for the increment of the pattern distortion in the center-fed subarray is due to the presence of both positive and negative slopes in phase distribution along the subarray within the evaluated frequency band.
5. The center-fed proximity-coupled array has been designed and simulated which consists of 12 subarrays. Compared with the center-fed subarray, the array of 12 subarrays is still able to control the amount of beam squint within $\pm 1°$ from 25.6 GHz to 26.8 GHz but with an overall offset of about 0.5°. For the pattern distortion, the average RMS value of the center-fed array over the evaluated frequency band increased by about 1.84% compared to the center-fed subarray considering the mutual coupling effect. After applying lossy materials, the center-fed proximity-coupled array shows promising scanning ability from 0° to 60° in azimuth with less than 3 dB scan loss and the cross-polarization level is 20 dB lower than the co-polarization level.

6.2. Recommendations

The performance of different kinds of series-fed subarrays radiating the csc^2 shaped beam pattern has been investigated in this thesis. The following are some potential improvements that can be further studied in future research:

1. This thesis focused only on the csc^2 shaped beam pattern. Since the design and analysis process in this thesis can also be applied to other shaped beam patterns such as dual-csc^2 and flat-top, further investigation can be done by implementing the design and analysis process to other shaped beam patterns and studying the performance of the array in terms of the pattern stability.
2. In this thesis, only single polarization (vertical) is considered. Since the antenna arrays used in based stations can benefit from dual polarization, the series-fed arrays with dual polarization can be implemented.
3. In this thesis, the beam squint reduction techniques using only passive components are considered. There are also techniques using active components for beam squint reduction such as the non-foster circuit and the true time delay circuit. Such techniques with active components can be implemented

during further research to check their performance in beam squint reduction and also the increment of power consumption.

4. In this thesis, a simple coax-to-strip line feeding structure is implemented on the center-fed proximity-coupled subarray for impedance matching. Since this thesis is focused on the structure of the unit cell, no further study has been done on the influence of different feeding structures. During further investigation, different feeding structures can be implemented to the designed array to improve the impedance bandwidth.
5. In this thesis, the $\csc^2$ radiation pattern is synthesized using a pre-defined MATLAB code based on an iterative re-phasing method. Currently, the code is able to generate the synthesized pattern based on a radiation pattern from a single isolated unit cell. In order to complement the influence brings by the mutual coupling effect, it is desired that the code is able to synthesize the pattern based on the embedded pattern of each unit cell. In future research, the code can be improved to realise the pattern synthesizing based on embedded patterns. In addition, during the optimization process of the subarray, sometimes it is hard to reach a certain value of excitation amplitude or phase due to the limitation of dimensions. For example, in the design of the proximity-coupled subarray, the length of the phase shifter should be controlled within certain dimensions to reduce the cross-polarization level. What's more, since in center-fed configuration, the pattern shape is sensitive to the phase distribution, improvement of the pattern stability can be made by limiting the range of the phase variation during the synthesis process. Therefore, it is desired that the MATLAB code is able to set some constraints to the amplitude or phase distribution, for example, limit the range of phase or synthesize the pattern with an amplitude-only algorithm. Such possibilities can be studied during further research.
6. This thesis focused on simulation-only results. During further research, the sensitivity check against design errors can be done on the designed center-fed proximity-coupled array, followed by the fabrication process of the designed array. Then, measurements can be done on the fabricated prototype to get the experimental results.

References

[1] *IEEE International Network Generations Roadmap, 1st edition, hardware roadmap, 2019*. URL: https://futurenetworks.ieee.org/roadmap/.

[2] Emil Björnson et al. “Massive MIMO: Ten myths and one critical question”. In: *IEEE Communications Magazine* 54.2 (2016), pp. 114–123.

[3] Yanki Aslan et al. “Multiple beam synthesis of passively cooled 5G planar arrays using convex optimization”. In: *IEEE Transactions on antennas and propagation* 68.5 (2019), pp. 3557–3566.

[4] Han Yan et al. “10.1109/MCAS. 2019.2909447”. In: *IEEE circuits and systems magazine* 19.2 (2019).

[5] Wei Hong et al. “Multibeam antenna technologies for 5G wireless communications”. In: *IEEE Transactions on Antennas and Propagation* 65.12 (2017), pp. 6231–6249.

[6] Yun Hu et al. “A novel hybrid analog-digital multibeam antenna array for massive MIMO applications”. In: *2018 IEEE Asia-Pacific Conference on Antennas and Propagation (APCAP)*. IEEE. 2018, pp. 42–45.

[7] Antoine Roederer et al. “Shaped Elevation Patterns for 5G Base Stations”. In: *2021 IEEE International Symposium on Antennas and Propagation and USNC-URSI Radio Science Meeting (APS/URSI)*. IEEE. 2021, pp. 795–796.

[8] Tomas Mikulasek et al. “Transverse slot with control of amplitude and phase for travelling-wave SIW antenna arrays”. In: *IET Microwaves, Antennas & Propagation* 14.15 (2020), pp. 1943–1946.

[9] Jan Puskely et al. “5G SIW-Based Phased Antenna Array With Cosecant-Squared Shaped Pattern”. In: *IEEE Transactions on Antennas and Propagation* 70.1 (2021), pp. 250–259.

[10] Zhao Changxu et al. “Shaped-beam subarrays for equi-power urban area coverage with modularity and low cost”. In: *European Conference on Antennas and Propagation* (2022).

[11] Aggeliki Sgora. “5G spectrum and regulatory policy in Europe: an overview”. In: *2018 Global Information Infrastructure and Networking Symposium (GIIS)*. IEEE. 2018, pp. 1–5.

[12] Thomas Metzler. “Microstrip series arrays”. In: *IEEE transactions on Antennas and Propagation* 29.1 (1981), pp. 174–178.

[13] R Mailloux et al. “Microstrip array technology”. In: *IEEE transactions on antennas and propagation* 29.1 (1981), pp. 25–37.

[14] Chenhui Niu et al. “Design and simulation of linear series-fed low-sidelobe microstrip antenna array”. In: *2007 Asia-Pacific Microwave Conference*. IEEE. 2007, pp. 1–4.

[15] YI Chong et al. “Microstrip series fed antenna array for millimeter wave automotive radar applications”. In: *2012 IEEE MTT-S International Microwave Workshop Series on Millimeter Wave Wireless Technology and Applications*. IEEE. 2012, pp. 1–3.

[16] Z Chen et al. “A taper optimization for pattern synthesis of microstrip series-fed patch array antennas”. In: *2009 European Wireless Technology Conference*. IEEE. 2009, pp. 160–163.

[17] Tao Yuan et al. “A novel series-fed taper antenna array design”. In: *IEEE antennas and wireless propagation letters* 7 (2008), pp. 362–365.

[18] Andrea Vallecchi et al. “Design of dual-polarized series-fed microstrip arrays with low losses and high polarization purity”. In: *IEEE Transactions on Antennas and Propagation* 53.5 (2005), pp. 1791–1798.

[19] Shaya Karimkashi et al. “A dual-polarized series-fed microstrip antenna array with very high polarization purity for weather measurements”. In: *IEEE transactions on antennas and propagation* 61.10 (2013), pp. 5315–5319.

[20] Ke Wu et al. “The substrate integrated circuits - a new concept for high-frequency electronics and optoelectronics”. In: *6th International Conference on Telecommunications in Modern Satellite, Cable and Broadcasting Service, 2003. TELSIKS 2003.* Vol. 1. 2003, P–III. DOI: 10.1109/TELSKS.2003.1246173.

[21] Jan Puskely et al. “SIW based antenna array with power equalization in elevation plane for 5G base stations”. In: (2018).

[22] Hussam Al-Saedi et al. “SIW series-fed patch antenna array based on transverse slot excitation for millimeter wave (MMW) applications”. In: *2016 IEEE International Symposium on Antennas and Propagation (APSURSI)*. IEEE. 2016, pp. 1593–1594.

[23] Yu-Hang Yang et al. “TFSIW-excited dual-polarized array antenna with 30° beam-pointing for millimeter-wave applications”. In: *IEEE Transactions on Antennas and Propagation* 67.8 (2019), pp. 5740–5745.

[24] Dong-yeon Kim et al. “Prototype Ku-band dual polarization SIW monopulse antenna”. In: *Proceedings of 2014 3rd Asia-Pacific Conference on Antennas and Propagation*. IEEE. 2014, pp. 565–568.

[25] Fabrizio Gatti et al. “A novel substrate integrated coaxial line (SICL) for wide-band applications”. In: *2006 European Microwave Conference*. IEEE. 2006, pp. 1614–1617.

[26] HRD Filgueiras et al. “SICL-based Antenna Array for 5G Massive MIMO Applications in mm-waves”. In: *2021 Antenna Measurement Techniques Association Symposium (AMTA)*. IEEE. 2021, pp. 1–5.

[27] Ke Xing et al. “Backlobe and sidelobe suppression of a Q-band patch antenna array by using substrate integrated coaxial line feeding technique”. In: *IEEE Antennas and Wireless Propagation Letters* 16 (2017), pp. 3043–3046.

[28] Bing Liu et al. “A novel slot array antenna with a substrate-integrated coaxial line technique”. In: *IEEE Antennas and Wireless Propagation Letters* 16 (2017), pp. 1743–1746.

[29] Bing Liu et al. “A novel substrate-integrated coaxial line transverse slot array antenna”. In: *IEEE Transactions on Antennas and Propagation* 67.9 (2019), pp. 6187–6192.

[30] Bing Liu et al. “A 45° Linearly Polarized Slot Array Antenna With Substrate Integrated Coaxial Line Technique”. In: *IEEE Antennas and Wireless Propagation Letters* 17.2 (2018), pp. 339–342.

[31] Fabrizio Gatti et al. “A novel substrate integrated coaxial line (SICL) for wide-band applications”. In: *2006 European Microwave Conference*. IEEE. 2006, pp. 1614–1617.

[32] Sensong An et al. “Ultrawideband Schiffman Phase Shifter Designed With Deep Neural Networks”. In: *IEEE Transactions on Microwave Theory and Techniques* 70.11 (2022), pp. 4694–4705. DOI: 10.1109/TMTT.2022.3189655.

[33] Shao Yong Zheng et al. “Broadband Phase Shifter Using Loaded Transmission Line”. In: *IEEE Microwave and Wireless Components Letters* 20.9 (2010), pp. 498–500. DOI: 10.1109/LMWC.2010.2050868.

[34] Yun-Peng Lyu et al. “Dual-Band Differential Phase Shifter Using Phase- Slope Alignment on Coupled Resonators”. In: *IEEE Microwave and Wireless Components Letters* 28.12 (2018), pp. 1092–1094. DOI: 10.1109/LMWC.2018.2875997.

[35] Israël Boudreau et al. “Broadband phase shifter using air holes in substrate integrated waveguide”. In: *2011 IEEE MTT-S International Microwave Symposium*. IEEE. 2011, pp. 1–4.

[36] Wei Zhang et al. “A compact wideband phase shifter using slotted substrate integrated waveguide”. In: *IEEE Microwave and Wireless Components Letters* 29.12 (2019), pp. 767–770.

[37] Omid Niksan et al. “Miniaturized array antenna with reduced beam squinting”. In: *AEU-International Journal of Electronics and Communications* 117 (2020), p. 153110.

[38] Marco A. Antoniades et al. “A CPS Leaky-Wave Antenna With Reduced Beam Squinting Using NRI-TL Metamaterials”. In: *IEEE Transactions on Antennas and Propagation* 56.3 (2008), pp. 708–721. DOI: 10.1109/TAP.2008.916965.

[39] Kypros M. Kossifos et al. “A NRI-TL Metamaterial Leaky-Wave Antenna Radiating at Broadside With Zero Beam-Squinting”. In: *IEEE Antennas and Wireless Propagation Letters* 17.12 (2018), pp. 2223–2227. DOI: 10.1109/LAWP.2018.2871722.

[40] Kyriakos Neophytou et al. “Compact Folded Leaky-Wave Antenna Radiating a Fixed Beam at Broadside for 5G mm-Wave Applications”. In: *IEEE Antennas and Wireless Propagation Letters* 21.2 (2022), pp. 292–296. DOI: 10.1109/LAWP.2021.3128563.

[41] José Luis Gómez-Tornero et al. “Substrate integrated waveguide leaky-wave antenna with reduced beam squint”. In: *2013 European Microwave Conference*. 2013, pp. 491–494. DOI: 10.23919/EuMC.2013.6686699.

[42] Lei Wang et al. “Substrate Integrated Waveguide Leaky-Wave Antenna With Wide Bandwidth via Prism Coupling”. In: *IEEE Transactions on Microwave Theory and Techniques* 66.6 (2018), pp. 3110–3118. DOI: 10.1109/TMTT.2018.2818149.

[43] Sehyun Park et al. “Center feed single layer slotted waveguide array”. In: *IEEE transactions on antennas and propagation* 54.5 (2006), pp. 1474–1480.

[44] Min Chen et al. “Bandwidth enhancement of substrate integrated waveguide (SIW) slot antenna with center-fed techniques”. In: *2011 International Workshop on Antenna Technology (iWAT)*. IEEE. 2011, pp. 348–351.

[45] Yao Zong et al. “A novel center-fed SIW inclined slot antenna for active phased array”. In: *Progress In Electromagnetics Research Letters* 88 (2020), pp. 97–104.

[46] Junfeng Xu et al. “CPW center-fed single-layer SIW slot antenna array for automotive radars”. In: *IEEE Transactions on Antennas and Propagation* 62.9 (2014), pp. 4528–4536.

[47] Teng Li et al. “Millimetre-wave slotted array antenna based on double-layer substrate integrated waveguide”. In: *IET Microwaves, Antennas & Propagation* 9.9 (2015), pp. 882–888.

[48] Irfan Ali Tunio et al. “Mutual coupling reduction in patch antenna array using combination of shorting pins and metallic walls”. In: *Progress In Electromagnetics Research C* 107 (2021), pp. 157–171.

[49] Henry Abu Diawuo et al. “Broadband proximity-coupled microstrip planar antenna array for 5G cellular applications”. In: *IEEE Antennas and Wireless Propagation Letters* 17.7 (2018), pp. 1286–1290.

[50] Mohammed Serhir et al. “Antenna modeling based on a multiple spherical wave expansion method: Application to an antenna array”. In: *IEEE transactions on antennas and propagation* 58.1 (2009), pp. 51–58.

A

Phased array design with fin structures

During the design of the phased array, the thermal performance can be improved by adding the fin-like structures as shown in Figure A.1. Before performing the thermal analysis process, it is important to evaluate the electromagnetic performance of the array to check the impact of those fin structures on the array. In order to have a minimum impact on the electromagnetic performance of the array while having a good thermal performance, the fins were placed only around the center elements which are closer to the power source. The material of the fins was pure copper. The dimensions of the fins were designed with 0.02 mm thickness, 3 mm width and 5 mm height.

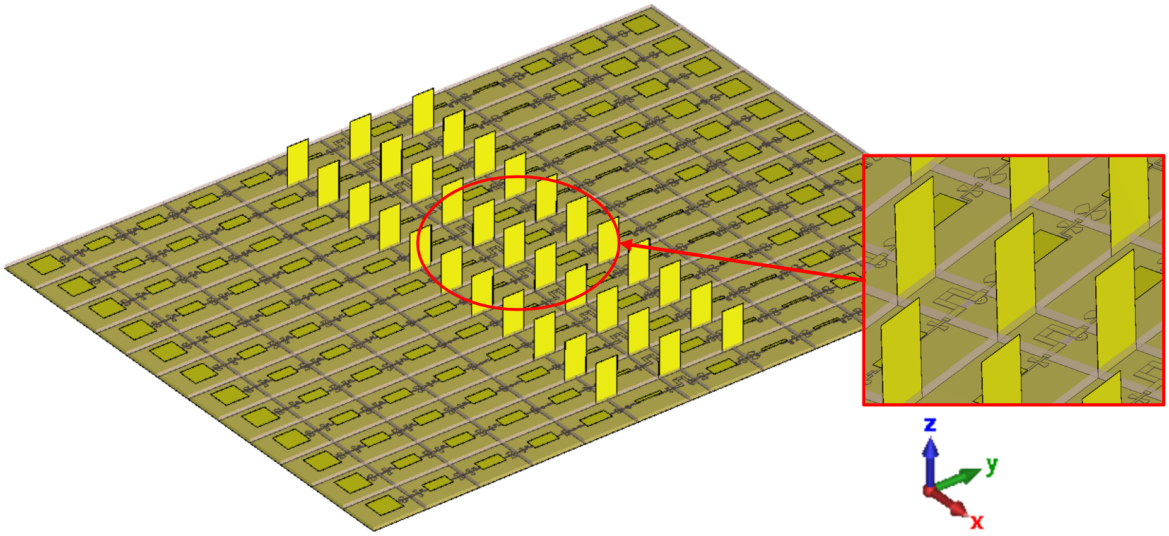

Figure A.1: Center-fed proximity-coupled array with fin structures

The simulation process was done in CST Microwave Studio based on the model shown in Figure A.1. The comparisons were then made with the performance of the center-fed proximity-coupled array with the lossy materials. Figure A.2 shows the comparison between the array with and without the fins in terms of the beam squint and pattern distortion. It can be seen that the difference in the beam squint is within 1° between the array with and without fins. On the other hand, the average RMS value over the frequency from 25.6 GHz to 26.2 GHz increased by 7% compared to the array without fins, and the average RMS value over the frequency from 26.2 GHz to 26.8 GHz decreased by 5%. As a result, the average RMS values over the evaluated frequency band of the array with and without the fins are both around 12.65%. Figure A.3 shows the reflection coefficients of the edge subarray (S11) and center subarray (S66). It is observed that by adding the fins to the array, the bandwidth does not change for both the center or the edge subarray. The port-to-port coupling between the edge subarrays (S21) and between the center

subarrays (S76) is shown in Figure A.4, where both S21 and S76 are below -20 dB after adding the fins to the array. Based on the above results, adding the fins to the array can be a potential solution to improve the thermal performance of the array, since the fins do not bring much influence to the electromagnetic performance of the original array.

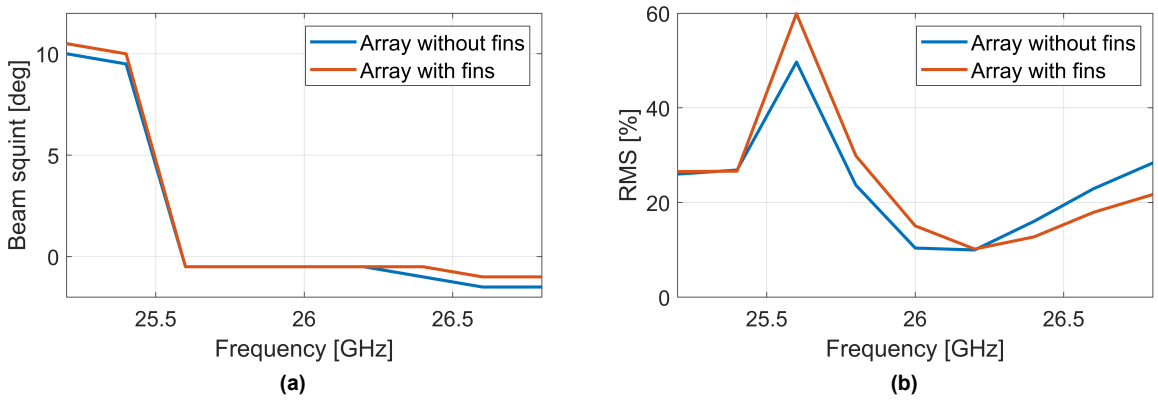

Figure A.2: Pattern analysis between the array with and without fins: (a) beam squint, (b) pattern distortion

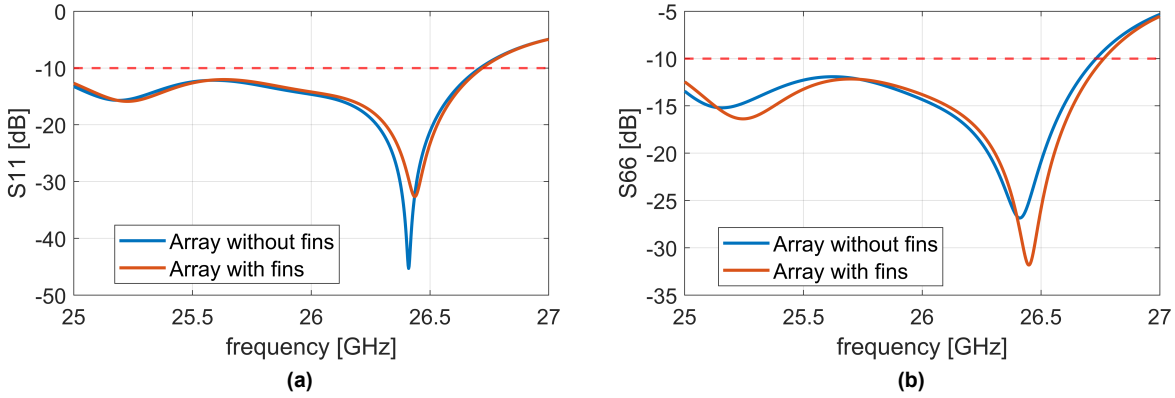

Figure A.3: Reflection coefficients of the arrays with and without fins: (a) S11, (b) S66

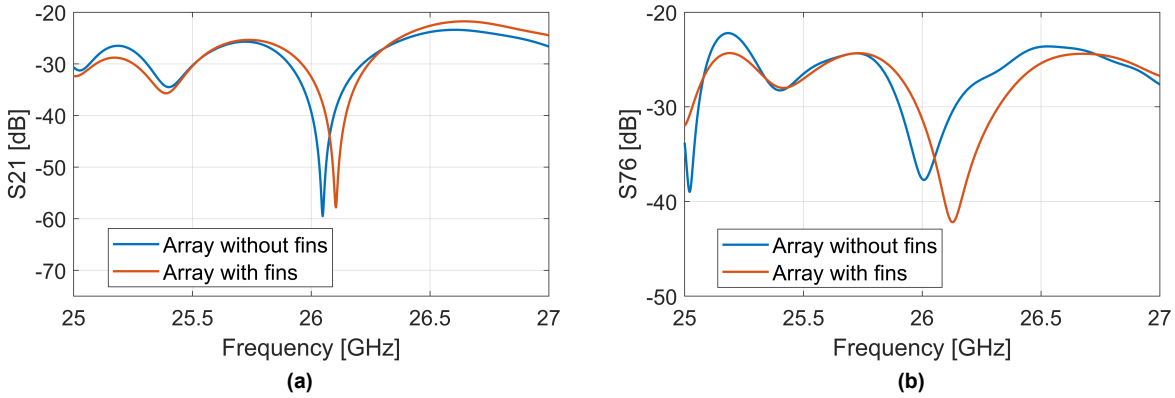

Figure A.4: Port-to-port coupling of the arrays with and without fins: (a) S21, (b) S76